




FACULTY OF SCIENCE AND TECHNOLOGY
MASTER THESIS

Study program/specialization:
Mathematics and Physics

Spring semester, 2022
open access

Writer:
Parisa Roshaninejad


.....
(Writer's signature)

Faculty supervisor:
Olena Zavorotynska
External supervisor(s):
Smagul Karazhanov

Thesis title:
Structure and morphology of CeO₂ thin films from Raman spectroscopy and microscopic studies.

Credits (ECTS): 60

KEY words:
Material physics
Energy related materials
Raman spectroscopy
Polarized Raman spectroscopy
X-ray diffraction (XRD)
Scanning electron Microscope (SEM)

pages: 93
+ enclosure: 3
Stavanger, 15/07/2022
Date/Year

University Of Stavanger

Department Of Mathematics and Physics

Structure and morphology of CeO₂ thin films from Raman spectroscopy and microscopic studies.

Supervisors:

Associate professor Olena Zavorotynska

Dr. Smagul Karazhanov

Author

Parisa Roshaninejad

July 15, 2022

Abstract

Cerium oxide has been subject of numerous studies because of its current and potential uses in supercapacitors, solar cells, self-cleaning glasses and in catalysis. Use of ceria in self-cleaning glass, especially on the solar cells, has been of interest because of its innate hydrophobicity, high transparency and low misfit factor with silicon.

This research work focuses on study and characterization of CeO₂ thin films deposited on Si and glass substrates prepared in IFE. For the thin films of CeO₂ with different thicknesses on Si, annealing was performed at four different temperatures at 400 °C, 600 °C, 800 °C and 1000°C for 30 minutes in air and 40 minutes in vacuum. After annealing, for some of the samples, Silicon oil was deposited on their surfaces by placing in oven at 100 °C overnight. To characterize the structure of the films, different techniques have been incorporated including Raman spectroscopy, polarized Raman spectroscopy (PRS), water contact angel (WCA) measurement, scanning electron microscopy (SEM), and X-ray diffraction (XRD).

The results showed that annealing of the coating increased crystallinity and decreased the size of ceria grains. PRS studies demonstrate the polycrystallinity of CeO₂ thin films is grown on single crystalline Si substrate. The model calculations were in good agreement with experimental data for single crystal. SEM images provided a good insight on morphology of the grains in the thin film and provided a measure of particle sizes. These results later confirmed by XRD studies and calculations based on acquired XRD patterns regarding the size of the ceria grains which indicated that by increasing the temperature the size of grains increased by increasing crystallinity. XRD tests carried out at UiS were combined with the data from IFE to provide a better picture of the changes in structure with annealing temperature.

Table of Contents

Introduction.....	8
1.1. Thesis purpose.....	8
1.2. Background	8
Theory.....	14
2.1. Cerium Oxide	14
2.2. Water contact angle.....	19
2.3. Polydimethylsiloxane (PDMS).....	21
2.4. Magnetron sputtering.....	22
2.5. Raman Spectroscopy.....	23
2.5.1. Factor group analysis	27
2.5.2. Polarized Raman Spectroscopy.....	28
2.6. SEM	33
2.7. XRD.....	35
Methods	38
3.1. Sample preparation	38
3.1.1. CeO ₂ on Glass substrate	38
3.1.2. CeO ₂ on Si substrate.....	39
3.2. Raman Spectroscopy.....	40
3.2.1. CeO ₂ on glass support	41
3.2.2. CeO ₂ on Si support.....	41
3.3. Calculation methods (Polarized Raman curves).....	41
3.4. XRD.....	45
3.5. WCA.....	45
3.6. SEM	46
Results and Discussions.....	48
4.1. Factor group analysis	48
4.2. Raman study of CeO ₂ films on glass substrate	49
4.2.1. Dependency of Raman peak shift and intensity on film thickness.....	50
4.2.2. Dependency of Raman peak shift on O ₂ /Ar ratio.....	53

4.3.	Raman study of CeO ₂ on Si substrate	54
4.4.	Polarized Raman Spectroscopy (PRS)	59
4.5.	WCA	63
4.6.	SEM	64
4.7.	XRD measurement.....	69
	Conclusion	77
	References.....	80
	List of Figures	87
	List of Tables	90
	Appendices.....	91
	Appendix A: High resolution SEM Images	91

Preface

This master thesis leads to a master's degree in mathematics and physics in University of Stavanger, and this research work is a part of COOL LONGBOAT Project (“Complex of online and onsite lectures on materials for hydrogen generation by solar water splitting”) funded by the Research Council of Norway. The samples for this work, CeO₂ thin films, have been prepared using magnetron sputtering by Damir Z. Mamedov under supervision of Dr. Smagul Karazhanov at Institute for Energy Technology (IFE).

Measurements and data analysis using Raman spectroscopy, polarized Raman spectroscopy, water contact angle measurements and SEM including experimental work and calculations have been done by me under supervision of assoc. prof. Olena Zavorotynska at the University of Stavanger. X-ray diffraction, particle size calculation and WCA measurements have been done both at IFE by Damir Mamedov and at the UiS by me.

Parisa Roshaninejad

July 2022

Stavanger, Norway

Acknowledgements

First of all, I would like to express my gratitude to my supervisor Olena Zavorotynska, at the University of Stavanger for all her guidance, support and for giving me the opportunity to work with various characterization techniques as much as possible regarding the limited time of Master program. Not only learning from her knowledge but also here great personality inspired me during whole this period. Being optimistic, not losing the hope and problem-solving skills were valuable skills that strength in me by working with her through the last year of my Master period

I would also like to thank my co-supervisor Dr. Smagul Karazhanov and Damir Zamirovich Mamedov at Institute for Energy (IFE) in Oslo, for preparing the samples and for all their guidance, particularly for helping me to get better understanding of research question, suggesting different ways to reach the answer of them.

I would also like to acknowledge Dr. Andreas Delimitis for all his guidance, specifically for his assistance with the scanning electron microscope. I want to thank Dr. Mona Minde for helping me to get high resolution SEM images.

I would like to thank my family for all their supports and encouragements in whole my lifespan.

Thanks,

Parisa Roshaninejad

Commonly used Abbreviations

COOL LONGBOAT	Complex of Online and Onsite Lectures on Materials for Hydrogen Generation by Solar Water Splitting
FCC	Face centered cubic
FWHM	Full width at half maxima
PRS	Polarized Raman spectroscopy
REO	Rare earth oxide
RS	Raman Spectroscopy
UiS	University of Stavanger
XRD	X-Ray diffraction
PDMS	polydimethylsiloxane
CCD	Charged Couple Device
IFE	Institutt For Energiteknikk
WD	Working Distance
SE	Secondary Electron
BSE	Back Scattered Electron

Chapter 1

Introduction

1.1. Thesis purpose

The goal of this thesis was to study and learn about CeO₂ thin films. In particular, the effect of synthesis conditions on microstructure of CeO₂ was studied. In addition, with an aim to increase hydrophobicity, CeO₂ films were coated by PDMS after annealing in different conditions. These thin films are designed to function as self-cleaning coatings on solar cells. In this research we used a few techniques to study the surfaces, including Raman and polarized Raman spectroscopy, SEM, XRD, and WCA analyses.

The second goal was to learn how to use the tools to best study and understand the surfaces and how to analyze the results obtained.

1.2. Background

Cerium-Oxide (Ceria) has attracted much attention due to its unique structure and physical properties and is of interest as a catalyst in multiple systems like vehicle emissions, as solid oxide fuel cell electrolyte material, gas sensors, optical coatings, high temperature superconductors, supercapacitors, and transparent materials in smart window technologies [1]. Because of similarity in lattice parameters, it is a potential material for silicon-on-insulator structures and a possible alternative for silicon in high temperature circuit boards [2]. CeO₂ is an interesting buffer layer material for the growth of some overlayers on Si in devices which is because of the perfect matching with Si that cause to prevent heat diffusion. Ceria is especially interesting because it exhibits several remarkable properties due to its ability to switch between two oxidation states (4+, 3+) corresponding to CeO₂ and Ce₂O₃ respectively, while keeping a fluorite structure [3]. Various synthesis methods have been reported to prepare CeO₂ nanoparticles including spin coating, sol-gel, magnetron sputtering, evaporation deposition, spray pyrolysis, laser deposition, ion beam sputtering and self-propagating method. The effect of different synthesis parameters on the resultant features of CeO₂ films, including the Raman spectra, has been investigated in several previous studies as summarized below.

Porqueras et. al. used **electron beam deposition** for preparation of CeO₂ films and investigated the influence of oxygen flow rate on the structural and optical properties of prepared samples on different substrates. Their study shows that all the structural characteristics such as orientation and crystal sizes are sensitive to changing the oxygen pressure and or flow rate [1]. In another work, which used the same method, CeO₂ films were prepared on glass substrates with different film thicknesses between 140 to 180 nm. These films showed excellent transparency in the visible region, while exhibiting low reflectance values in the UV region [2].

Elidrissi et.al., investigated the optical and structural properties of CeO₂ thin films prepared by the **spray pyrolysis**. In this research work CeO₂ was deposited on glass by using two solutions (CeCl₃·7H₂O and Ce(NO₃)₃). The thickness of samples determined to be 0.5-1 μm by using SEM. They found out that below 350°C, changing substrate temperature leads to having amorphous structure; however, by increasing the temperature to 500 °C crystals will be obtained. XRD results shows the obtained films were polycrystalline with cubic fluorite structure strongly oriented along (100). Surface morphology (grain size) was found to depend on initial solution and for Ce (NO₃)₃ shows small grain size. The peaks acquired in Raman study are (465(Ce-O), 556(Si-O), 1100(Si-O)). Films prepared from both precursors show about 80% transparency for visible and near infrared region [4]. In other work using the same method, cerium oxide nanoparticles were synthesized with cerium acetylacetonate, Ce (CH₃COCHCOCH₃)₃ (Ce(acac)₃). The resultant nanoparticles' size was in the range of 4.2–20 nm and film thicknesses were in the range of 340–790 nm, which were calculated from XRD patterns and SEM observation, respectively. The presence of two new peaks in 270 and 315 cm⁻¹ in Raman Spectra of nanocrystalline CeO₂ with smaller sizes indicates the nanosize effect and can be explained as surface phonon modes of nanometer CeO₂. At the same time linewidth of peak 463 cm⁻¹ decreases noticeably with increasing nanocrystals' size. A red shift in Raman peak position was reported by decreasing the crystallite size down to 4.2 nm [5].

In a separate work on preparing CeO₂ thin film on sapphire substrates, a polymeric precursor was used, and **spin coating** technique was employed. Preparation with this technique followed by drying and crystallizing the resulting film at temperatures in the range of 300 – 1200°C which leads to having a uniform distribution of grains with size ranges from 4 to 300 nm depending on the annealing temperature. The results showed that as the particle size decreases, the F_{2g} mode of Ce–O symmetric vibration shifts from 464 cm⁻¹ to 450 cm⁻¹. For analyzing the Raman spectra, a spatial correlation model was used, and the disorder induced by the microstructure was defined by the correlation length as a function of grain size instead of half width or line asymmetry [6].

The influence of annealing at different temperatures on the microstructural changes of CeO₂ have been also studied by Askrabic et.al. Studying structural and vibrational properties showed that by increasing annealing temperature, the oxygen vacancies change which has a significant effect on conductivity and oxygen storage of ceria. It was demonstrated that micro-strain effects dominate over size effects in annealed samples because of the significant change of oxygen vacancy

concentration with annealing. In this work a fine nanocrystalline powders of ceria was prepared by the **self-propagating method** at room temperature, using cerium nitrate as a precursor and then annealed in four temperatures from 200-500°C. The Raman peak located at 598 cm^{-1} represents vibrations induced due to the presence of oxygen vacancies (intrinsic vacancies), decreases in intensity by increasing annealing temperature which confirm the reduction of oxygen vacancies. In this work a new Raman peak was obtained at 480 cm^{-1} , which classified as a probable surface mode induced by large defective structure and disorder in the CeO_2 lattice [7].

The epitaxial growth of the CeO_x on Si has been carried out by **pulsed laser deposition** in an ultra-high vacuum (UHV) of 1.3×10^{-8} Pa. The XRD measurements exhibits a fine fluorite cubic structure with intense (100) and (200) peaks of cerium oxide. X-ray photoelectron spectroscopy showed the formation of Ce^{3+} in interface which decreases through thickness of the film and finally converts to higher capacity form of cerium, Ce^{4+} , in surface. They also observed formation of SiO_x in interfaces of non-passivated Si substrate (passivation was carried out with hydrogen to prevent formation of SiO). It also has been proven that O_2 pressure has a significant effect on full oxidation and epitaxial growth of CeO_2 . In lower pressure the XPS spectra is more likely to be Ce^{+3} and higher pressure to be Ce^{+4} and at least a pressure of 5×10^{-5} is needed for fully oxide cerium [8].

Another synthesis method for production of cerium oxide (CeO_{2-x}) nanoparticles is **pulsed plasma in liquid (PPL)**. The XRD result exhibits the formation of pure cubic ceria however the lattice constant is slightly larger than the commercial ceria can be attributed to the small particle size and the high concentration of Ce^{3+} ions. On the same account, XPS analysis showed that the cerium oxide nanoparticles synthesized by the pulsed plasma liquid method had a higher Ce^{3+} proportion (42.2%) than some commercial powders. The produced cerium oxide nanoparticles showed better polishing characteristics of quartz glass, compared to commercial samples. These results may be due to the high Ce^{3+} -ion or the small particle size [9].

In other research work, for the CeO_2 thin film prepared with **sol gel method**, the red shift of 464 cm^{-1} peak in Raman spectra and it's broadening were explained by the combined effects of strain and phonon confinement induced by reducing particles size. They also calculated the lattice constant which increased by decreasing particle size. The temperature-dependent Raman spectra showed a red shift in the peak position and increase in the linewidth at increasing temperature in all of the samples with particle size of 6nm, 25nm and $5\text{ }\mu\text{m}$ [10]. In a recent study also using **sol gel method** on the behavior of cerium oxide nanoparticles of different sizes at different temperatures the absence of the Ce (III) oxidation state on the surface of CeO_2 nanoparticles, even for particles as small as 2nm has been confirmed. It was also shown that the formation of hydroxyl groups at the surface affects the chemical performance of these nanomaterials. In this research work the CeO_2 nano materials synthesized by using $\text{Ce}(\text{NO}_3)_3 \cdot 6\text{H}_2\text{O}$. It was shown that the drying process did not have any influence on the phase crystallinity, morphology, and particle size distribution [11].

Reactive ion beam sputter is another useful technique for deposition of CeO_2 thin films. The studying of effect of oxygen partial pressures and substrate temperatures shows a preferential

orientation of (220) up to a 200 °C which is changed to (200) at 400 °C and above. Substrate temperature maintained in the range of 50-500°C and it was shown that for the temperatures above 300°C Raman FWHM decreases beside peak shift and XRD broadening which confirms the formation of nanocrystalline phase with better crystallinity [12].

In another it was showed that the best crystallinity with a good morphology and a high resistivity has been obtained for a CeO₂ layer deposited by **magnetron sputtering** and post-annealed at 1000°C for 30s. The chamber pressure was 10⁻⁴Pa with a magnetron power of 60 W, anode-cathode distance was 3 cm and deposition pressure 10 Pa with the resultant film thickness of 530 nm. In this work RTA was done with a JIPELEC. It showed that by RTA the FWHM of Raman spectra decreases and the peak position shifts from 465.2 to 464.7 cm⁻¹. Morphology study showed that the crystallite size remains constant for different RTA used [13].

In two connected articles, Schilling et al. used DFT model to calculate the Raman peaks for ceria, both in oxidized (Ce⁴⁺) and reduced (Ce³⁺) configurations. The calculated peak positions comply with the observed peaks for ceria powders acquired. A peak calculated at 250 cm⁻¹ was attributed to surface mode of clean CeO₂ (111) which was observed in experimental work. Vibrational bands in experimental test between 480 to 600 cm⁻¹ were because of oxygen defects and Ce³⁺ ions. Characteristic peroxide (O₂²⁻) stretching vibrations peaks were calculated and observed at 800 to 900 Cm⁻¹ range. They also observed that with reducing crystallite size, there is red shift and broadening of characteristic *F*_{2g} Raman peak around 464 cm⁻¹. The defect features manifested at 550 and 590 cm⁻¹, were increased by decreasing crystallite size. Based on these two observations, Schilling et al. claimed that phonon confinement is the reason for this behavior. They used UV-V is spectroscopy to get the band gap of the transformations and used the data to check for quantum size effects. They pose that reduced ceria is deposited at the grain boundaries of oxidized ceria and as this prevails, increase of a band gap with decreasing particle size (quantum size effect) is not observed in their work. Interestingly, the depicted intensity of 595 cm⁻¹ Raman peak (attributed to defects) had a inverse relationship with band gap (calculated from UV-Vis studies). Hence, the intensity of this peak can be used as a measure of quantum size effect [14] [15].

During numerous works done on CeO₂ coatings and powders, it became apparent depending to deposition technique, different parameters have effects on the coating properties. In electron beam deposited coatings, all the characteristics were dependent on oxygen pressure and flow rate. The films prepared by this method showed great transparency (low reflectance). In spray pyrolyzed films, substrate temperature affected the crystallinity of structure. Also, surface morphology depended on the composition of precursor. In spin coated samples on sapphire, with decreasing particle size, a Raman shift in *F*_{2g} mode of vibration is evident. In a self-propagated prepared coating, which underwent some heat treatment afterwards, increasing annealing temperature changes oxygen vacancy concentration which in turn causes changes in conductivity. Also, because of highly defective structure, a new Raman peak was obtained. In laser deposited samples in ultra-high vacuum, Ce³⁺ was reported to be formed at the interface (low oxygen) and the ratio

of $\text{Ce}^{3+}/\text{Ce}^{4+}$ was decreased gradually till the open surface. In this case, oxygen pressure was the main reason behind this trend in the layer and higher pressure leads to higher Ce^{4+} content and epitaxial growth. The sol-gel deposited coatings of ceria, showed a red shift in Raman peak which was attributed to the effect of strain and phonon confinement because of reduced particle sizes. In this case, lattice constant was increasing by decreasing particle size. With increasing temperature, the red shift and the peak width increased. In another sol-gel prepared coating, Ce^{3+} was absent for particles prepared at different temperatures. It was also concluded that drying process has no effect on crystallinity, morphology and particle size distribution. Coatings prepared by ion beam sputtering show preferential growth in (220) and then (200) directions. A decrease in FWHM of characteristic Raman peak of ceria was reported in higher temperatures along with similar decrease in FWHM of XRD peak of ceria. This is attributed to increased crystallinity. A magnetron sputtered coating prepared elsewhere showed very good crystallinity and desirable morphology. The desirable properties were obtained through a specific fast heat treatment (RTA). After heat treatment, FWHM of Raman peak of ceria was decreased and peak shifted to lower wave numbers.

Magnetron sputtering is one of the preferred techniques to synthesize the thin film materials because the optimal plasma distribution can lead to a perfect adhesion of thin films to substrates. On the other hand, it makes it possible to prepare the films in bigger size which in commercially preferable method. Changing the deposition parameters on CeO_2 thin films features have been studied in recent works. Shi et. Al., evaluated the influence of bias voltage (negative voltage on substrate) on the morphology, wetting behavior, microstructure, mechanical and tribological properties of cerium dioxide (CeO_2) on Si (100) substrates deposited by reactive unbalanced magnetron sputtering in an Ar- O_2 gas mixture in the chamber pressure of 4×10^{-4} Pa. Applying a varying negative voltage on substrate from -20 to -160V, it was shown that the peak intensity of CeO_2 (111) increased with increasing bias voltage and after reaching its maximum at -80 V, decreases significantly which is accompanied with the increasing of hexagonal Ce_2O_3 (101) peak around 30.4° . Studying surface morphology by SEM and AFM indicates that the smoothest surface was obtained at a bias voltage of -60 V. All deposited coatings exhibited a hydrophobic feature with the water contact angle around 100° , which was close to the value obtained from Teflon surface [14].

The effect of Radio Frequency (RF) power on the properties of magnetron sputtered CeO_2 thin films on glass substrate at a pressure of 3×10^{-4} mbar of Ar atmosphere was studied by Murgan et.al. The power was changed between 150, 200 and 250 W and the measured film thicknesses corresponding to the RF power were 380, 470 and 590 nm respectively. The deposited CeO_2 films showed a polycrystalline structure with two strong peaks for (111) and (220) in XRD measurements. With increasing RF power, a significant intensity increase was visible for (220) peak which point to the growth of CeO_2 films in a particular order. Studying the optical properties of resultant films in the wavelength range 325–900 nm indicated that they are highly transparent in visible region and exhibit low reflectance in the ultraviolet region. With increasing thickness, optical band gap of the films decreased from 3.53 to 3.45 eV. Increase of RF power, beside

increasing of defects, increased the crystallite size from 6 to 9 nm and increased lattice parameter as well. However, it also led to increasing surface roughness from 2.9 to 7.7 nm as ascertained from AFM images and width and intensity of CeO₂ peak at 466 cm⁻¹. Whilst the peak for Raman active mode (F_{2g}) was obtained at 465.4 and 466.0 cm⁻¹ for the films prepared at RF powers 200 and 250 W respectively, there was no significant peak for the films prepared at 150 W power. Existence of this peak confirms the cubic fluorite structure of resultant CeO₂ which appeared in XRD experiments. RF power induced formations of flower like morphology were observed in SEM images [15].

The effect of deposition temperature (200-800°C), magnetron power (2-125 W), anode-cathode distance (2-6cm) and post deposition RTA on epitaxial growth and structural characterization of CeO₂ thin films deposited by on-axis RF magnetron sputtering on Si (111) substrate has been studied in a different work. The films were prepared using Argon-ion as sputtering gas at 10⁻⁴ Pa. rapid thermal annealing (RTA) was performed in the range of 400-950°C. The XRD results reveal a non-textured target by exhibiting same results of powder and target. By increasing both the growth temperature and RTA, the FWHM of Raman peak decreases which is attributed to better crystallinity. While short anode-cathode distance, high RF power and higher growth temperature caused higher growth rate, the Raman peak position in 464 cm⁻¹ did not change [16].

The influence of the reaction gas composition during the DC magnetron sputtering process on the structural, chemical, and optical properties of CeO₂ thin films was studied using X-ray photoelectron spectroscopy (XPS) analyses revealed that cerium is present in two oxidation states, namely as CeO₂ and Ce₂O₃, at the surface of the films prepared at argon-oxygen flow ratios between 0-7%, whereas the films are completely oxidized into CeO₂ as the aforementioned ratio increases beyond 14%. X-ray diffraction (XRD) studies confirmed that all thin films exhibited a polycrystalline character with cubic fluorite structure for cerium dioxide [17]. Annealing increases crystallinity, using RTA, crystallinity has increased. Other than that, synthesis methods have been effective in crystallinity. But annealing at longer temperatures have not been carried out before. SO, it was a question that using longer times, how crystallinity is affected.

In this work we studied CeO₂ thin films prepared using magnetron sputtering at different conditions on two different substrates of Si and glass in IFE. Annealing was performed on samples at four different temperatures for 30 minutes in air and 40 minutes in vacuum. The resulting morphology of all the films and hydrophobic properties of the CeO₂/Si films was studied by Raman spectroscopy, SEM, and XRD. The effect of structural properties on Raman spectra, and in particular, on polarized Raman spectra were studied. Polarized Raman spectroscopy is a technique which gains information about orientation of crystals. In addition, the hydrophobic properties of the films were modified by coating the surface with PDMS. Water contact angle studies were performed, and the results were correlated with the morphological properties of the samples.

Chapter 2

Theory

In this section, theoretical bases behind the studied compound and the experimental tools and techniques employed in this study will be discussed. After a brief introduction about cerium oxide and magnetron sputtering as the thin film preparation technique, Raman spectroscopy which has been used for studying the structural properties of cerium oxide thin films before and after annealing (on two different substrates of silicon and glass), and PRS, the technique incorporated to gain information about orientation of the deposited ceria layer will be discussed. Lastly, a brief intro in SEM and XRD will be given. These techniques were used for better understanding of the thin film morphology, crystallite sizes as well as changes in lattice parameter after imaging.

2.1. Cerium Oxide

cerium (IV) oxide as a rare earth oxide is a yellow-white powder which also known as ceric oxide or ceria with the chemical formula CeO_2 . The most important feature of cerium oxide is its reversible conversion to a non-stoichiometric oxide. cerium (Ce) is the second element and the most common in the lanthanide series, and with atomic number of 58 is an important material with variety of applications in different fields, such as auto-exhaust catalyst [18], oxygen sensors [19], fuel cells [20] [21], glass-polishing materials [22], electrochromic thin-film application [23], solar cells and biotechnology. Cerium is 5 times more abundant than lead and is 25th most abundant element in earth crust.

CeO_2 has fluorite structure (fcc) with the space group of $Fm\bar{3}m$ (No. 225), consists of a simple cubic oxygen sub-lattice with the cerium ions occupying alternate cube centers as shown in Figure 2.1, 8-coordinate Ce^{4+} (represented by yellow balls) and 4-coordinate O^{2-} (represented by red balls). At elevated temperatures by releasing oxygen, it produces oxygen vacancies in the structure which can be measured by different techniques such as XPS (X-Ray photoelectron spectroscopy) to compare the ratio of Ce^{3+} to Ce^{4+} .

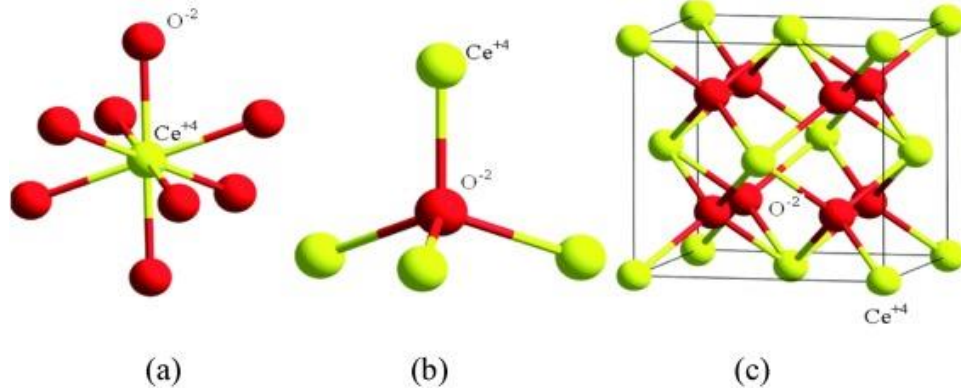


Figure 2-1: (a) and (b): eight-folds of cerium atoms and four-folds of oxygen atoms in CeO₂ structure; (c) fcc structure for CeO₂ [24].

Cerium normally has two types of oxides known as cerium dioxide (CeO₂) with fluorite structure and cerium sesquioxide (Ce₂O₃) with hexagonal crystal structure as it is shown in Figure 2-2, however because of higher stability of CeO₂ over Ce₂O₃, it is usually called cerium oxide. The Ce⁴⁺ oxidation state with [Xe]4f⁰ is usually considered more stable than [Xe]4f¹ for Ce³⁺.

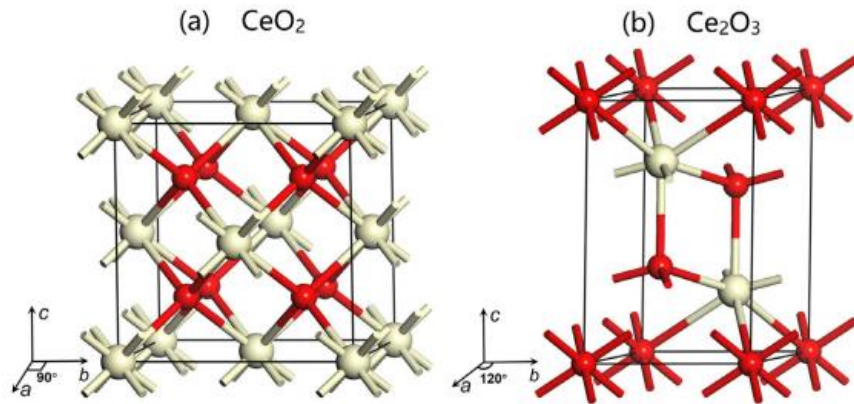


Figure 2-2: (a) Fluorite structure of CeO₂. (b) Hexagonal structure of Ce₂O₃. Grey color represents Ce atoms and red color represents O atoms [25].

Cerium oxide thin films are used extensively in electronic and energy related applications. Depend on the deposition technique and deposition parameters, type of substrate and composition, the microstructure of cerium oxide thin films can vary. By control of these parameters, epitaxial growth can be achieved or polycrystalline films with varying grain size from a few nanometers to micrometers can be prepared [26].

An ideal crystalline material consists of unit cells repeated in three dimensions indefinitely. Atoms are arranged in a crystal in symmetrical way. However, displacement of atoms from their position in the lattice leads to breaking symmetry of a perfect crystal. This can happen because of both

intrinsic and extrinsic defects. While extrinsic defects arise due to impurities or dopants, intrinsic defects may be produced because of the redox reactions between solid and surrounding atmosphere. The most important and stable defects of CeO₂ is related to oxygen vacancies which are produced during reversible transition of Ce³⁺ to Ce⁴⁺ according to the formula below:

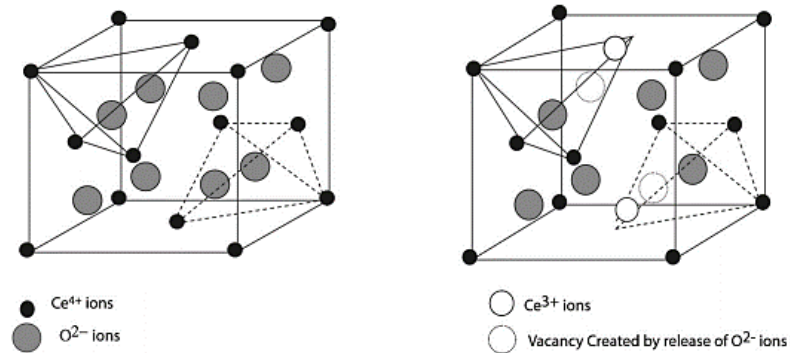
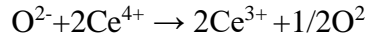


Figure 2-3: Comparison of Ce³⁺ and Ce⁴⁺ structure and oxygen vacancies produced in Ce³⁺ structure [27].

When O²⁻ ion leaves the structure as oxygen, two electrons are left in the crystal. These electrons can move through the structure and transfer electricity and heat. The motion of electrons in CeO₂ lattice can be considered a thermally mediated hopping mechanism [28]. This redox transition, between Ce³⁺ and Ce⁴⁺ can happen easily and this important property of CeO₂ makes it a suitable candidate to be used as a solid electrolyte in solid oxide fuel cells as it shows high oxygen ion conductivities [29].

Increasing the rate of Ce³⁺/Ce⁴⁺ leads to increasing lattice distortion because of changing in Ce-O bond length. This is because of the change in the radius of Ce⁴⁺, 0.92 Å to 1.034 Å of Ce³⁺ which in turn causes a disturbance in local symmetry and overall lattice parameter.

Oxygen vacancies have important effects on ceria crystals property mainly because of the catalytic activities arising from easier movement of oxygen in higher concentrations of oxygen vacancies. There are three low index lattice planes on cerium oxide surface namely as (111), (110), (100) which are shown in Figure 2-4. The order of stability, activity formation energy of oxygen vacancies, number of oxygen vacancies through these planes are summarized in below table [28] [29] [30]. Moreover, other factors like temperature and doping elements can influence on concentration of oxygen vacancies [31]. Zhou and Huebner have proposed a simple formula which correlates concentration of oxygen vacancies to the change in lattice parameter [32]. The idea is that as radius of Ce³⁺ is bigger than Ce⁴⁺, a higher portion of Ce³⁺ will make the Ceria lattice bigger, hence bigger lattice parameter.

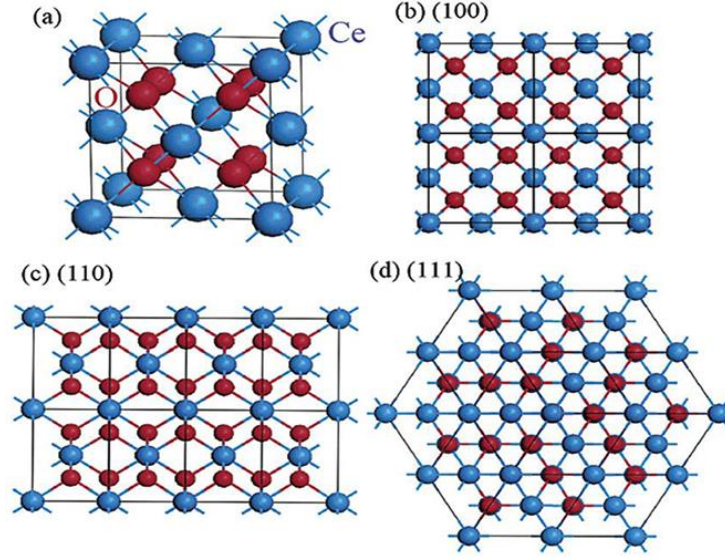


Figure 2-4: a) fcc crystal cell of CeO₂ structure. (b-d) the (100) or (200), (110), (111) planes of the CeO₂ structure [33].

The formula is presented below

$$\frac{\sqrt{3}}{4}(a' - a_0) = c \left[r_{Ce^{3+}} - r_{Ce^{4+}} + \frac{1}{4}(r_{V_{O^{\circ\circ}}} - r_{O^{2-}}) \right] \quad (2.1)$$

In this formula, $r_{Ce^{3+}}$ is the radius of Ce³⁺, $r_{Ce^{4+}}$ is the radius of Ce⁴⁺, $r_{V_{O^{\circ\circ}}}$ is the radius of oxygen vacancy, $r_{O^{2-}}$ is the radius of O²⁻ ion and a' is the lattice parameter of the sample. a_0 is the lattice parameter of bulk CeO₂ and corresponds to a supposedly 100 percent CeO₂. All the parameters other than lattice parameter are constants. C is the ratio of Ce³⁺/Ce⁴⁺ and is related to vacancy concentration through this formula

$$V_{O^{\circ\circ}} = O^{2-} * C/4 \quad (2.2)$$

O²⁻ is number of oxygen ions accompanying each cerium ion and in the fluorite structure of Ceria is equal to eight. Hence,

$$V_{O^{\circ\circ}} = 2C \quad (2.3)$$

And this gives us a measure of vacancies in our samples.

Table 2-1: comparison of stability, activity, the number and formation energy of oxygen vacancies for low index planes of ceria

Stability	(111)> (110)> (100)
Activity	(100)> (110)> (111)
Formation energy of oxygen vacancies	(111)> (110), (100)
Number of oxygen vacancies	(110), (100)> (111)

In ceria nanoparticles, it has been shown that by decreasing particle size, more oxygen vacancies were formed [20] [34]. So, it is possible to achieve desired reactivity by controlling the size. Recently a detailed study on ceria nanoparticles proved a systematic lattice expansion with reduction in particle sizes down to nanometer ranges in comparison to the bulk CeO_2 [35]. In the mentioned research work it was observed that in 1.1 nm CeO_2 nanoparticles, the cerium atoms occupy reduced state, without changing the cubic shape to hexagonal lattice [35].

Quantum size effect have significant influence on optical properties of nanomaterials but not on physical properties (their optical absorption and emission can be controlled with the quantum size effect) which arises by the confinement of electrons within small size particles [36]. The quantum confinement effect becomes considerable only when the size of the particles decreases to the wavelength of the electron range. Breaking this word to quantum and confinement helps to have a better understanding of this effect confinement means to make discreteness by limiting the motion of electron to specific energy levels and quantum talking about the atomic area of particles. While the size of quantum dots is smaller than the Bohr radius, confinement occurs which causes to have discreet energy level instead of continuity. By decreasing particle size to nanometer range, confinement, and discreteness of energy level of the band gaps increases (widens up). To study the quantum size effect a model calculation based of Raman peak shift and Raman peak width, and it was shown that the decreasing the size leads to a red shift. In addition, the width of Raman peak enlarges as shown ion Figure 2-5 [37].

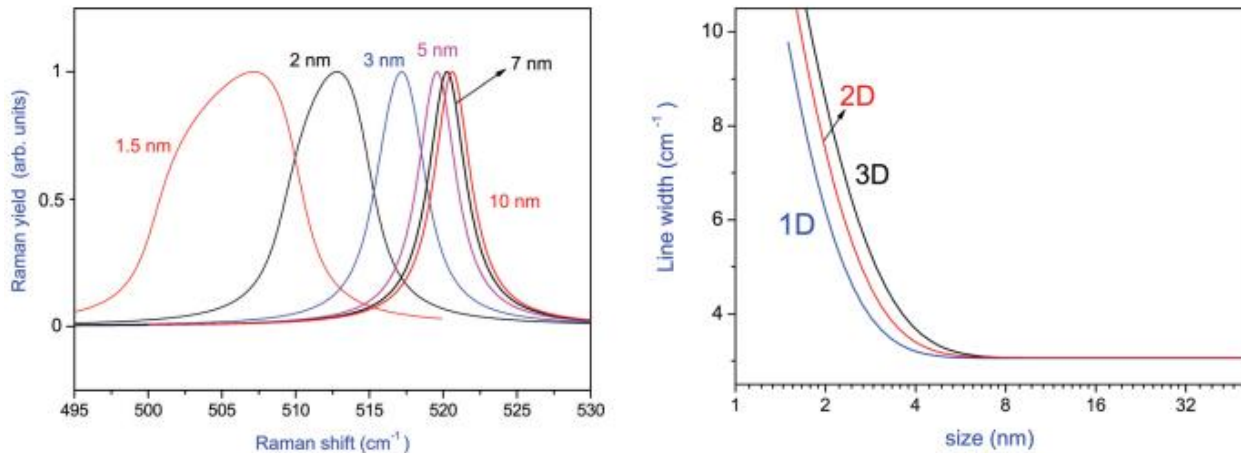


Figure 2-5: a) calculated Raman peak position for a layer of Si as a function of its thickness. The bulk Si frequency value is 521 cm^{-1} . b) Calculated Raman peak width calculated as a function of the size. The lines show how the confinement enlarges the Raman peak for a single (1D) size-limited direction, for a two-dimensional (2D) size-limited square wire, for a three-dimensional (3D) cube [37].

2.2. Water contact angle

Finding out and tuning surface wettability of ceramics has a vital effect in their usage in various applications. Hydrophobicity is often used for tuning the reactivity and mechanical properties of the surfaces, it also is useful for microfluids and thermal coatings [38] [39].

Water plays a key role in self-cleaning properties of surface. The wettability of oxide surface in general, is a function of surface properties such as defects, energetic and lattice termination which deal with the water contact angle at the surface of material (θ), where (θ) is shown in Figure 2-6. The material is considered as super hydrophobic when (θ) $\sim 0^\circ$ and super hydrophilic when (θ) $> 150^\circ$ [40]. Determining WCA exhibits the ability of surface to self-clean. This angle is affected by roughness of surface and different models is introduced for describing the wettability of surface as young's model, Wenzel's model, Cassie-Baxter's model [41].

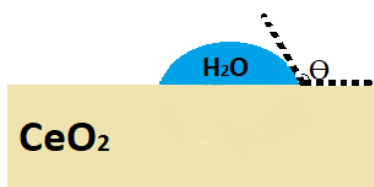


Figure 2-6: Schematic representation of water adsorption on a CeO₂ surface.

Both hydrophobic and hydrophilic properties are used for self-cleaning surfaces. For hydrophilic surfaces, these contaminations are removed by sliding of water which spread out on the surface. For hydrophobic surfaces while the contaminations like oil are resistant, the water droplets are easily removed. Having low sliding angle allows the collected water on the surface to be removed commonly by gravity and it is useful for removing any water-based debris.

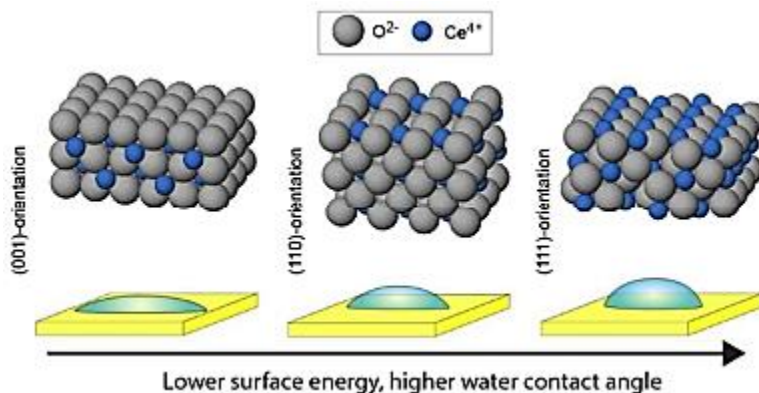


Figure 2-7: Understanding the wettability of rare earth oxide ceramics from crystallographic orientation – surface energy relationships [41].

CeO₂ by having hydrophilic properties widely used in in catalysis and biomedicine in which the adsorption and wettability's role become more significant [42]. Studies have shown that adsorption

behavior of various molecular and ionic species diverges significantly between the different crystallographic planes of CeO_2 [38] [39] [40]. The most hydrophobicity is reported for CeO_2 (111) surface [43]. According to density function calculations it has been shown that CeO_2 (111) surface was the most hydrophobic then followed by CeO_2 (100), and CeO_2 (110) surface [40] as shown on the Figure 2-7.

This is in line with other works that suggest WCA of rare earth oxide epitaxial film surface depends on orientations in crystal with different surface energy as $\text{WCA (111)} > \text{WCA (110)} > \text{WCA (001)}$ when $\text{SE (111)} < \text{SE (110)} < \text{SE (001)}$ [41]. It means that there is a close relation between the crystallographic orientation, wetting property, and the surface energy as it is shown in Figure 2-8.

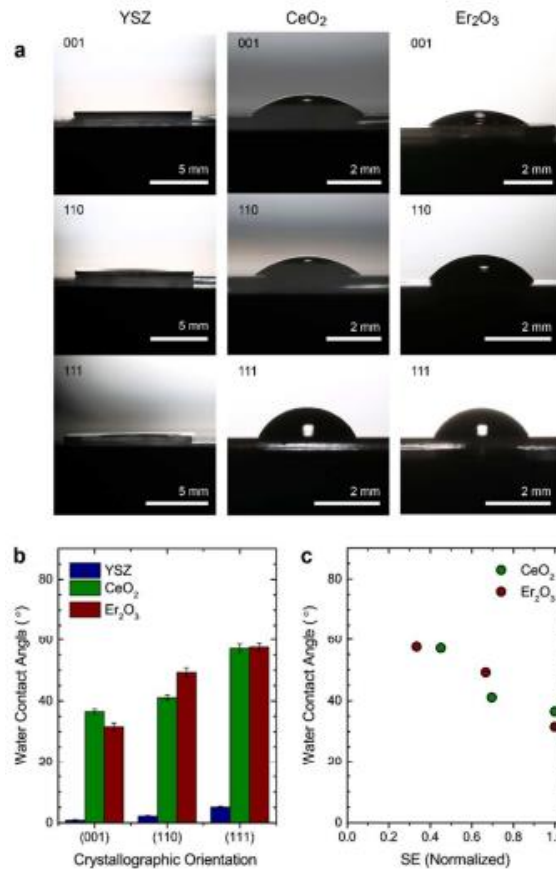


Figure 2-8: Wetting properties of three rare earth oxide's surface with different orientation. a) Water droplets on low index planes of YSZ, CeO_2 and Er_2O_3 epitaxial films. (b) the relationship between Water contact angle and crystallographic orientation relationships. (c) the relationship between water contact angle with surface energy (normalized). It is shown that the surface energy is inversely proportional to the water contact angle. [41].

For increasing hydrophobicity of the CeO_2 thin films, they are coated with polydimethylsiloxane (PDMS) which will be discussed in next part.

2.3. Polydimethylsiloxane (PDMS)

Polydimethylsiloxane (PDMS), also known as dimethylpolysiloxane or dimethicone, is the simplest member of a group of polymeric organosilicon compounds that called silicones or silicone oils. It is formed by hydrolyzing $(\text{CH}_3)_2\text{SiCl}_2$, which is a product of Muller–Rochow reaction between high-purity SiO_2 and CH_2Cl_2 [44].

PDMS has unusual rheological (or flow) properties. It is optically clear and, in general, inert, non-toxic, and non-flammable [45]. PDMS with a low molecular weight is used as a lubricant, antifoaming agent, and hydraulic fluid. The structure of PDMS is presented in following figures. In the formula, Me means methyl group (CH_3). The polymer is constructed by long chains of Si-O-Si bonds as shown on the Figure 2-8. Because of strongly non-polar methyl groups connected to the Si, throughout the chain, PDMS is non-polar and strongly hydrophobic [46]. PDMS has a water contact angle $>100^\circ\text{C}$ [47].

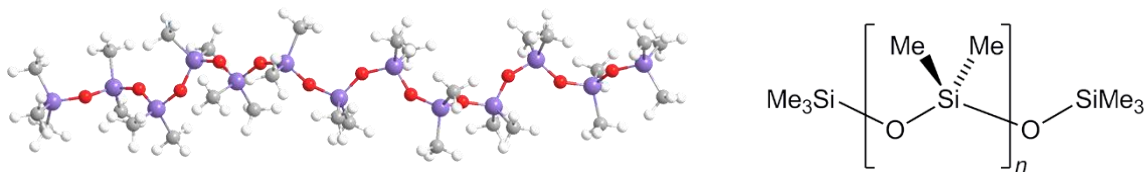


Figure 2-9: Molecular structure and bonds in PDMS [45]

Polydimethylsiloxane (PDMS) is a low-cost hydrophobic polymer that can be used to coat solid surfaces in thin films to make them water-resistant. PDMS coatings can produce superhydrophobic surfaces when paired with dual surface roughness [47]. The Raman spectrum of the sample of PDMS is shown in Figure 2-10.

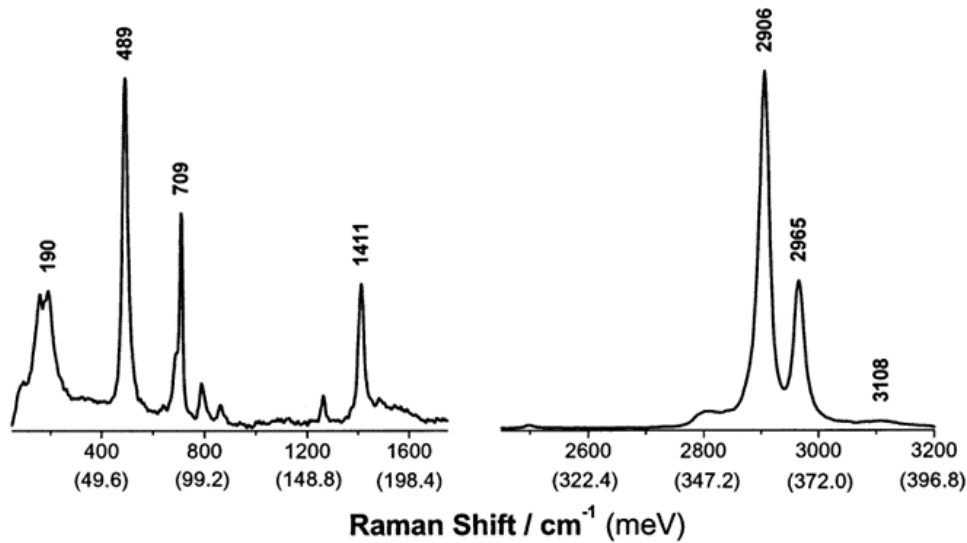


Figure 2-10: Raman spectrum of PDMS [47]

The Raman active vibrational modes of PDMS Raman spectrum have been summarized in Table 2-2.

Table 2-2: Observed FT-Raman and INS wavenumbers for 58100 molecular weight PDMS [48]

Raman (cm ⁻¹)	INS (cm ⁻¹)	assignment	symmetry				
2966		C-H sym str	A ₁	742	CH ₃ rock	B ₁	
2906		C-H sym str	A ₁	185	CH ₃ torsion	B ₁	
1411	1410	C-H asym bend	A ₁	190	183	C-Si-C rock	B ₁
1263	1264	C-H sym bend	A ₁	2966		C-H asym str	B ₂
861	870	CH ₃ rock	A ₁	2906		C-H sym str	B ₂
	709	C-Si-C sym str	A ₁	1411	1410	C-H asym bend	B ₂
489		Si-O sym str	A ₁	1263	1266	C-H sym bend	B ₂
190	190	C-Si-C scissors	A ₁	788	802	C-Si-C asym str	B ₂
	54	O-Si-O scissors	A ₁	680	687	CH ₃ rock	B ₂
2966		C-H asym str	A ₂	190	190	C-Si-C wag	B ₂
1411	1410	C-H asym bend	A ₂				

2.4. Magnetron sputtering

For this research work the CeO₂ thin films have been prepared in IFE using magnetron sputtering technique with different deposition parameters on two different substrates: single crystalline silicone and glass. The sputtering method is a useful technique for preparing semiconductors, metals, insulators, etc. The advantage of this technique having simple equipment, easy control, large coating area and strong adhesion. Magnetron sputtering process consists of ejection of target

material usually by an incident particle beam and sticking those onto a substrate as it is shown in Figure 2.11.

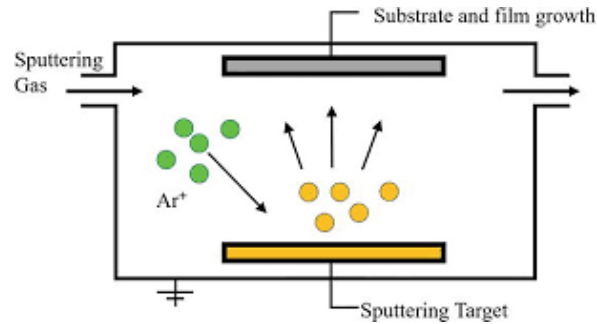


Figure 2-11: Schematic diagram of magnetron sputtering.

By producing magnetic field on the target, magnetic field and the electric field's interaction increases the probability of producing ions when electrons collide with the argon atoms. The generated ions collide with the target surface under the action of an electric field to sputter the target. This process is common between two types of magnetron sputtering, direct current (DC) magnetron sputtering and radio frequency (RF) magnetron sputtering. During this collision between incident particles and targets material, part of the momentum transfers to the target atom, which leads to cascade process and following collisions of these detached atoms with other target atoms leading to sputtering of the target atoms close to the surface. In DC magnetron, a potential difference is maintained between the substrate and target, promoting the deposition. RF sputtering is the preferred method and an important advantage of that it is suitable for coating any material and there is no need for the target to be electrically conductive.

2.5. Raman Spectroscopy

For studying the origin of molecule spectra, the molecular transitions including electronic, vibrational and rotational transitions can be considered. These transitions occur in different time scales, and this leads to a separation in the energy of molecule as follows:

$$E = E_{el} + E_{vib} + E_{rot} \quad (2.4)$$

These energies originate from the motion of electrons in the molecule, the vibrations of constituent atoms and the rotation of molecule. When the molecule is placed in the electromagnetic field, there would be a transfer of energy from field if the incident energy equals the energy difference of two quantized states according to the Bohr's Equation.

$$\Delta E = h\nu \quad (2.5)$$

Where ΔE is the difference between the ground state and the excited state. By absorbing this energy, the molecule will be excited from E_1 (initial vibrational level of electron) to a higher virtual energy state and when returning, emits energy. Depending on whether the emitted energy $h\nu$ equals to the absorbed energy or not, Rayleigh or Raman Scattering are expected.

Vibrations transitions occur in $10^2 \sim 10^4 \text{ cm}^{-1}$ range which are in infrared region, but not all the transitions between vibrational levels are allowed so the Raman active modes should be determined.

Nowadays for producing strong, coherent, and monochromatic light in wide range of wavelengths, lasers are used as the as the light source of Raman spectroscopy. Laser light causes electronic polarization of the molecule, leading to a scattered light with the frequency of $\nu \pm \nu_i$, where the ν_i is the vibrational frequency of the molecule. Then there would be a shift from incident light frequency ν that is what represented as Raman shift through this spectroscopic technique. For studying the origin of Raman spectra, assume the incident light with the electric field E and frequency of ν

$$E = E_0 \cos(2\pi\nu t) \quad (2.6)$$

Then the induced dipole moment of molecule radiated by this light will be

$$P = \alpha E = \alpha E_0 \cos(2\pi\nu t) \quad (2.7)$$

where α is called the polarizability tensor, which is a linear function of nuclear displacement q , where the molecule vibrating with the frequency ν .

$$q = q_0 \cos 2\pi\nu_i t \quad (2.8)$$

$$\alpha = \alpha_0 + \left(\frac{\partial\alpha}{\partial q}\right)q \quad (2.9)$$

Then from above equations we have

$$P = \alpha_0 E_0 \cos 2\pi\nu t + \frac{1}{2} \left(\frac{\partial\alpha}{\partial q}\right) q_0 E_0 \{ \cos[2\pi(\nu + \nu_i)t] + \cos[2\pi(\nu - \nu_i)t] \} \quad (2.10)$$

where these terms represent Rayleigh scattering, anti-stokes and stokes scatterings, respectively. The obtained lines related to Stokes scattering regarding Maxwell-Boltzmann distribution law (MB) are stronger because as it is shown in Figure 2-11, in the anti-stokes lines the molecule's initial state is $\nu = 1$ and after scattering it reaches to the $\nu = 0$ state. But for the stokes lines the initial state is $\nu = 0$ which has larger proportion according to the MB law at room temperature and normal pressure and that is why these lines are stronger. The Eq. 2.10 indicates that the Raman shifts can only be observed for the vibrations that change the polarizability of the molecule. This is called a Raman active vibration. The the complicated vibrations can be shown as a superposition of normal vibrations. The kinetic energy of an N-atom molecules can be expressed as

$$T = \frac{1}{2} \sum m_N \left[\left(\frac{d\Delta x_N}{dt}\right)^2 + \left(\frac{d\Delta y_N}{dt}\right)^2 + \left(\frac{d\Delta z_N}{dt}\right)^2 \right] \quad (2.11)$$

By generalizing the coordinates such that $q_i = \sqrt{m_i}\Delta x_i$, the kinetic energy will be

$$T = \frac{1}{2} \sum_1^{3N} \dot{q}_i^2 \quad (2.12)$$

For small values of displacements, located initially in equilibrium position, the potential energy by Taylor expansion be

$$V = \frac{1}{2} \sum_{ij}^{3N} b_{ij} q_i q_j \quad (2.13)$$

By solving Lagrange's equation, the solution is given as

$$q_i = q_i^0 \sin(\sqrt{b_{ij}}t + \delta_i) \quad (2.14)$$

where q_i^0 and δ_i are the amplitude and the phase constant respectively. As there is not any possibility for more simplifications, so it is needed to transform into a new coordinate as Q_i using the below equation

$$q_k = \sum_i B_{ki} Q_i \quad (2.15)$$

The Q_i are called the normal coordinates for the system. By doing all replacements in potential and kinetic energy formulas combined with Lagrange's equation the final solution will be

$$Q_i = Q_i^0 \sin(\sqrt{\lambda_i}t + \delta_i) \quad (2.16)$$

such a vibration is called a normal vibration and the frequency of this vibration is

$$\nu_i = \frac{1}{2\pi} \sqrt{\lambda_i} \quad (2.17)$$

Even though there are $3N-6$ total normal vibrations possible, not all of them will be active in Raman scattering. The Raman scattering effect which has been derived classically is not able to completely explain the phenomenon. However, it can be well understood by using quantum mechanics with the energy transfer model.

In a quantum mechanics theory, a photon is described as a quantum of light with the energy of

$$E = h\nu \quad (2.18)$$

where h is Planck's constant and ν is the frequency of the light. With the same way of introducing a photon, a phonon is a quantum of atomic vibration of the normal modes a lattice of a crystal with the energy of a phonon can be defined as having energy

$$E = h\nu_{vib} \quad (2.19)$$

where ν_{vib} is the frequency of the normal mode in the lattice. When the incoming light interacts with the atoms of the sample, it temporarily excites an electron to an unstable virtual state which is known as virtual absorption. The produced electron-hole pair recombine, returning the system to ground state and emitting a photon.

Incident light on the molecules interacts with their electronic cloud and can cause different modes of scattering.

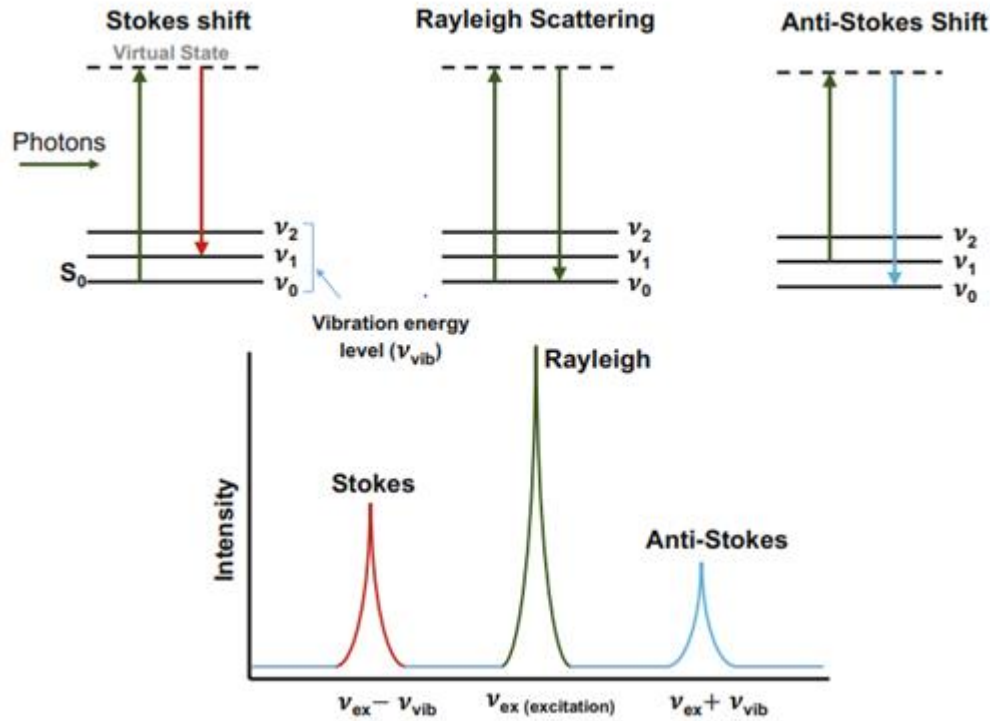


Figure 2-12: Rayleigh Scattering versus stokes Raman and anti-stokes Raman scattering [49]

Intensity of Raman spectra is proportional to square of the incident light and the polarizability of the dipole:

$$I_{Stokes} \propto \left(\frac{\partial \alpha}{\partial q} \right)_0 (\omega - \omega_i)^4 E_0^2, \quad \omega = \frac{2\pi}{\lambda} c, \quad E = E_0 \cos 2\pi \nu t \quad (2.20)$$

Which is solved to:

$$I_n = KI_0 \frac{(v_0 - \nu)^4}{\mu \nu (1 - e^{-h\nu/kT})} (45\bar{\alpha}^2 + 13\gamma^2) \quad (2.21)$$

Where K is the summarizing constant and a product of all other constant factors, I_0 is the intensity of incident light and proportional to E^2 , ν_0 is the frequency of incident light, ν is the frequency of scattered light which in Raman spectroscopy is stokes (or anti-stokes), μ is the reduced mass, h is Planck constant, k is Boltzmann constant, T is absolute temperature (in Kelvin), $\bar{\alpha}$ is the mean value of polarizability tensor which comes from the averaging tensor over random orientations or isotropic part of the Polarized Raman scattering, γ^2 is the anisotropic part of the polarizability averaged over all orientations.

Mean polarizability tensor, $\bar{\alpha}$, and anisotropic polarizability are functions of temperature. It is only natural to consider that, as temperature in fact is a measure of vibration of atoms or molecules. The relationships are:

$$\bar{\alpha} = \frac{T_r(\alpha)}{3} \quad (2.22)$$

$$\gamma^2 = 0.5[(\alpha_{xx} - \alpha_{yy})^2 + (\alpha_{yy} - \alpha_{zz})^2 + (\alpha_{zz} - \alpha_{xx})^2 + 6(\alpha_{xy}^2 + \alpha_{yz}^2 + \alpha_{zx}^2)] \quad (2.23)$$

To find out about the nature of the outcome of Raman spectroscopy the first step is to understand the selection rules which give us the ability to distinguish between Raman active and inactive modes. As the only peaks that appears in Raman spectra belongs to the compounds with Raman active mode

2.5.1. Factor group analysis

In each normal vibration, each nuclei have a harmonic motion with same vibration frequency of other nuclei. But occasionally the direction of vibration can differ, which is called a degenerate vibration. If the molecule has an axis higher than two-fold, doubly degenerate and if it has more than C_3 axis, triply degenerate vibrations occur.

Changing the aspects of polarizability ellipsoid (size, shape, or orientation) contributes to whether a Raman mode is going to be active or not. This is because according to Eq. 2.7 induced dipole moment and electric field are in the vector form however the polarizability is a second rank tensor governing $x y z$ axis.

Selection rules basically depend on molecule's symmetry which is defined by the spatial arrangement of nuclei. Based on spatial symmetry of molecule it has a set of defined symmetry elements and belongs to a point group (combinations of two or more symmetry elements when there are more than one symmetry element). The spatial symmetry of a compound is denoted by the space group which in total there are 230 different space group. Schonflies notation is commonly used when talking about point groups and site symmetries. To find out about the Raman active modes, understanding of Mulliken symbols as "A", "B", "E", "T" in addition to "1", "2", "g", "u" subscripts is necessary. A one-dimensional (singly degenerate mode) representations are indicated with A/B while E and T(F) denotes the two-dimensional (doubly degenerate) and three dimensional (triply degenerate) representations.

The "1", "2" subscript indicates the symmetric or anti-symmetric modes with respect to a rotation around a two-fold axis (C_2) normal to C_n and "g" or "u" depending on the mode is symmetric or anti-symmetric with respect to the inversion through center.

To summarize the capital letters indicates the degeneracy and symmetry with respect to principal axes while the subscripts indicate the symmetry with respect to mirror plane or inversion centers. In factor group analysis, first step is to find the positions of atoms in unit cell and site symmetries. The compound discussed in this thesis work, cerium oxide, consists of cerium and oxygen atoms which belongs to the following point groups (in Schonflies notation) respectively:

(1) T_d : Three perpendicular C_2 axes, four C_3 axes, a σ_d through each pair of C_3 axes (σ_d introduces a plane of symmetry).

(2) O_h : Three perpendicular C_4 axes, four C_3 axes, and a center of symmetry, regular cubic molecules where they consist of p-fold axis of symmetry (C_p).

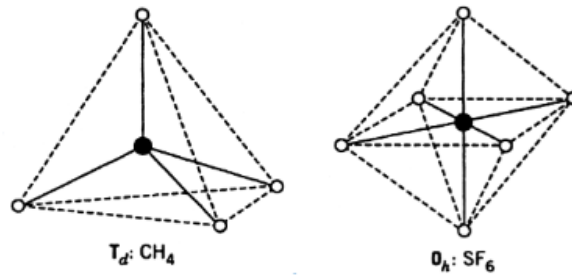


Figure 2-13: Example of molecules belongs to T_d , O_h point groups [50].

The next step is to find the linear function related to the point group in character. Using correlation between point group and site symmetry to find out how the irreducible representations transforms, will ended up with finding Raman active mode.

2.5.2. Polarized Raman Spectroscopy

Many optical applications require an understanding of polarization and the ability to manipulate light polarization. However, polarization is an important feature of light that impacts even optical systems that do not measure it directly.

The electric field of light oscillates perpendicularly to the direction of propagation. However, if its direction fluctuates randomly in time, it is considered as unpolarized light like sunlight but if it is well defined it is called polarized light which can be classified into three types. The classical plane wave solution of the electromagnetic wave equation for the electric fields is

$$E(r, t) = |E| \text{Re}\{|\varphi\rangle \exp[i(kz - \omega t)]\} \quad (2.24)$$

Where E is the amplitude of field, ω is the angular frequency and $|\varphi\rangle$ is polarization state in x-y plane

$$|\varphi\rangle = \begin{pmatrix} \psi_x \\ \psi_y \end{pmatrix} = \begin{pmatrix} \cos\theta \exp(i\alpha_x) \\ \sin\theta \exp(i\alpha_y) \end{pmatrix} \quad (2.25)$$

1. If $\alpha_x = \alpha_y$, the polarization will be linear, and the electric field of light has one component which is oscillated in a single plane along the direction of propagation (Figure 2-14 c)
2. If α_x , is rotated by $\pi/2$ with respect to α_x without changing the amplitude, the polarization will be circular. The electric field of the light rotates in a circle around the direction of propagation and includes two linear components that are perpendicular to each other (Figure 2-14 b)
3. If the α_x be different from α_y and the amplitude be different also that would be elliptical polarization which is the combination of two linear components with different amplitudes and/or a phase difference that is not $\pi/2$ [50] (Figure 2-14 a).

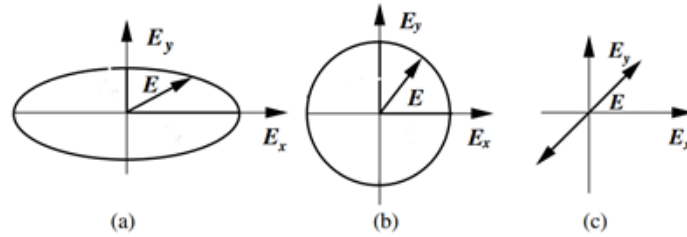


Figure 2-14: States of polarization in (a) elliptical polarization, (b) circular polarization, (c) linear polarization [51].

PRS gives a spectrum with a polarization either parallel (I_{\parallel}) or perpendicular (I_{\perp}) to the polarization of the incident light is achievable which provides useful data for acquiring information about the orientation of molecules in crystals, polymers, and liquid. PR provides the option to investigate the changes in molecular structure of liquids in interfaces with solids, compared to the same liquid as an isotropic sample. Liquids are considered isotropic samples in PR. Isotropic samples are randomly oriented samples, like liquids and microcrystalline powders. Raman scattered light is made up of light with polarizations that are both parallel to and perpendicular to that of the excitation light. Both components are recorded in the same spectrum during typical Raman measurements. In contrast, polarizing filters are employed to measure the Raman spectra of each component independently during polarized Raman measurements [52].

PRS of single crystals are different than liquids. Single crystals are considered anisotropic samples. This means that unlike in a liquid, where molecules are positioned arbitrarily in space, chemical bonds in a crystal are all orientated in specific directions, and not all Raman bands can be identified from a single crystal face. As a result, when viewing a single crystal face, one should not expect to find all Raman modes, especially if the crystal face is a crystallographic X, Y, or Z axis face. This means that not every vibration mode is visible in single crystals placed in the instrument. Sample may need to be placed in another direction and investigated again.

When comparing parallel and perpendicular polarized Raman spectra obtained from single crystals to parallel and perpendicular spectra obtained from a liquid sample, there is a significant

difference. In a liquid, you sample all orientations of the molecule in space, whereas in a single crystal, all chemical bonds are oriented in space according to the crystal class to which the compound or element belongs [53].

In this research work PRS was used for studying the orientation of CeO₂ crystal and Si single crystal which is used as the substrate layer. The polarized Raman spectra are formed by inserting a polarizer within the beam path between the sample and spectrometer, allowing the Raman polarization to be chosen by the user. The polarization of the beam can be changed by inserting polarizing optics between the laser and the sample. There is also the option of polarizing scattered light which depends on the possibility with the instrument.

Depolarization ratio is defined as Eq. 2.26

$$p = I_{\perp}/I_{\parallel} \quad (2.26)$$

Where I_{\perp} is the intensity of Raman band perpendicular to light beam and I_{\parallel} is the intensity with parallel polarization to the laser light. Depolarization ratio allows for determination of the symmetry of the vibrational mode. If $p = 3/4$ then it depolarized and is considered as non-symmetric vibration, however if $p < 3/4$ then the vibration is polarized and is symmetric in nature.

Regarding the familiar rule for Raman active vibrations according to Eq 2.24, changing the polarizability is the main requirement for monitoring the Raman Peak.

$$p = \alpha E \quad (2.27)$$

Where α is the Raman polarizability tensor which is fixed relative to position of atoms and directions of the bonds. The symmetry and orientation of the sample and the polarization of light as two effective factors of Eq 2.24 are also significant factors in the Raman peak intensity as

$$I \propto |e_i R e_s|^2 \quad (2.28)$$

Where e_i is the incident wave polarization and e_s is scattered light polarization and R (or α) is the Raman tensor(s). For the face centered cubic crystal structure there are three degenerate tensors as

$$R_x = \begin{bmatrix} 0 & 0 & 0 \\ 0 & 0 & d \\ 0 & d & 0 \end{bmatrix}, R_y = \begin{bmatrix} 0 & 0 & d \\ 0 & 0 & 0 \\ d & 0 & 0 \end{bmatrix}, R_z = \begin{bmatrix} 0 & d & 0 \\ d & 0 & 0 \\ 0 & 0 & 0 \end{bmatrix}$$

The parallel and cross polarization produced by changing scattered light polarization as below:

$$e_i = (1 \ 0 \ 0)$$

$$e_s^{\parallel} = (1 \ 0 \ 0)$$

$$e_s^{\perp} = (0 \ 1 \ 0)$$

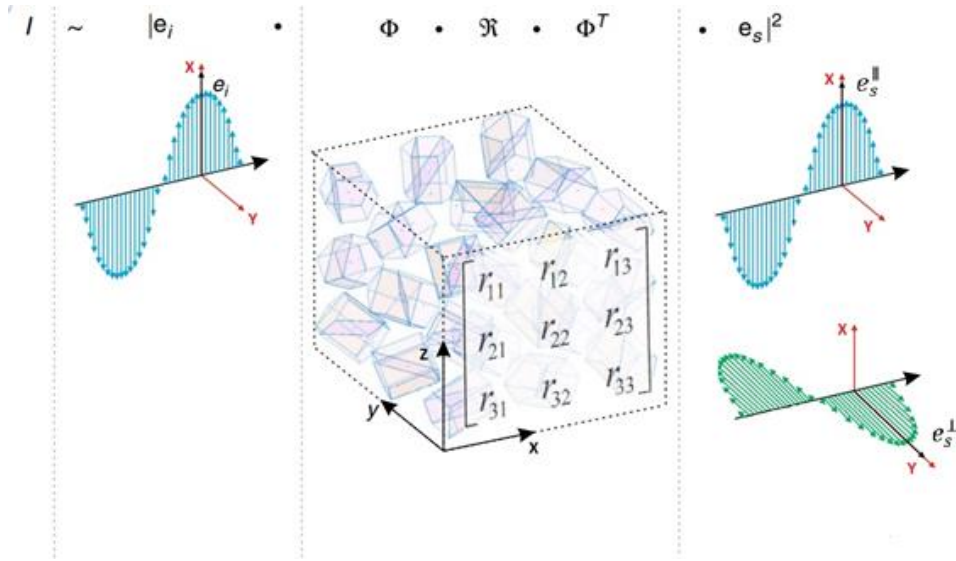


Figure 2-15: Illustration of the incident/scattering polarization on a polycrystalline sample.

To describe the orientation of a rigid body vs. fixed coordinate system, Euler angles (θ , φ , χ) can be used where their exact position is showed in Figure 2-15. Considering Euler angles (φ_{xyz}), the Raman tensor in Cartesian system of coordinates associated to the crystal frame transforms into that of the laboratory via

$$R_{xyz} = \Phi_{xyz} R \bar{\Phi}_{xyz} \quad (2.29)$$

Several Cartesian coordinates to be described as follows:

1. XYZ which is the observer's axis system which is fixed in space and its origin translating with the crystal center of mass
2. xyz which is the crystal axis system

Assuming the molecular center of mass is fixed, the Euler angles describing the orientation of x , y , z axis in the XYZ coordinate system has been shown in Table 2-2.

θ and φ are ordinary polar coordinates and χ is the angle in xy plane measuring the rotation clockwise about z axis.

Table 2-3: Rotating to nonrotating axes as function of Eulerian angles

	X	Y	Z
x	$\cos\theta\cos\varphi\cos\chi - \sin\varphi\sin\chi$	$\cos\theta\sin\varphi\cos\chi - \cos\varphi\sin\chi$	$-\sin\theta\cos\chi$
y	$-\cos\theta\cos\varphi\sin\chi - \sin\varphi\cos\chi$	$-\cos\theta\sin\varphi\sin\chi + \cos\varphi\cos\chi$	$\sin\theta\sin\chi$
z	$\sin\theta\cos\varphi$	$\sin\theta\sin\varphi$	$\cos\theta$

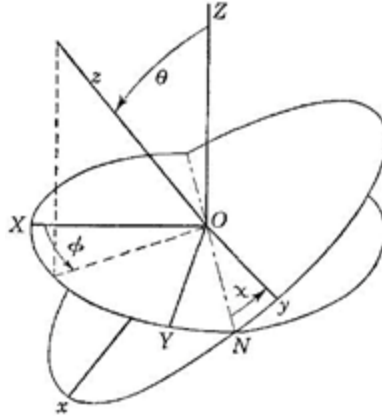


Figure 2-16: Euler angles position related to laboratory coordinate system (XYZ) and crystal coordinate system (xyz)

These results come from the basic definition for rotation around three principal axes. A rotation of θ radians about the Z-axis is defined as

$$\Phi_z(\theta) = \begin{bmatrix} \cos\theta & -\sin\theta & 0 \\ \sin\theta & \cos\theta & 0 \\ 0 & 0 & 1 \end{bmatrix}$$

A rotation of ϕ radians about the X-axis is defined as

$$\Phi_x(\phi) = \begin{bmatrix} 1 & 0 & 0 \\ 0 & \cos\phi & -\sin\phi \\ 0 & \sin\phi & \cos\phi \end{bmatrix}$$

A rotation of χ radians about the Y-axis is defined as

$$\Phi_y(\chi) = \begin{bmatrix} \cos\chi & 0 & \sin\chi \\ 0 & 1 & 0 \\ -\sin\chi & 0 & \cos\chi \end{bmatrix}$$

Sequence of rotations can be represented as the matrix product which is known as rotation matrix

$$\Phi = \Phi_z(\theta)\Phi_x(\phi)\Phi_y(\chi) \quad (2.30)$$

However, as matrix multiplication does not commute, the order of the axes which one rotates about can change the result. So first we rotate about the z-axis, then the x-axis, and at the end about the y-axis.

2.6. SEM

Scanning electron microscope (SEM) uses high energy focused electron beam for producing images from different type of samples and gaining the information about topography and morphology, texture, chemical composition, crystallography, and orientation of materials. The main components of SEM are Electron gun, Electromagnetic Lenses, Scanning coil, Vacuum chamber and detector [54]. During the exposure of light on sample a few interactions occur which is shown in Figure 2-16. Secondary electron (SE) with the energy range less than 50 eV are the main means of viewing image in SEM. These electrons are produced by inelastic scattering interactions with primary electrons ejected from conduction or valence bands of the specimen atoms. Due to their low energy, these electrons originate from within a few nanometers below the sample surface and interact with the top surface of the specimen so mainly affected by the topographic features of the sample.

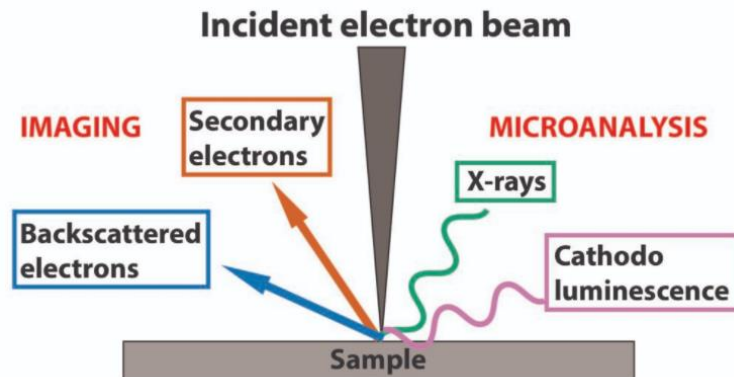


Figure 2-17: Types of interactions of incident electron beam in SEM. [55]

The elements with higher atomic number because of producing stronger electromagnetic field attracts more electron atomic number, the element creates a stronger field which through an elastic interaction reflects lots of electrons and leads to brighter image. On the other hand, light elements reflect less electron that causes them to look darker in SEM images. As it is shown in Figure 2-18 in a distance of $D/2$ above and below the best focus point the diameter of the beam becomes bigger than the pixel diameter and the overlapping of signals from the pixels leads to overlap of image. According to Eq. 2.31 Depth of field, D is proportional to the working distance and final aperture size:

$$D \propto \frac{2p}{\alpha} \quad (2.31)$$

$$\alpha \approx \tan \alpha = \frac{r}{w} \quad , \quad r = A/2 \quad (2.32)$$

Where α is the divergence angle and r , the radius of aperture. It is expected that by decreasing aperture size or increasing the working distance, the divergence angle decreases which leads to

increasing the depth of field. However, by increasing the work distance the number of electrons interacting with sample decreases which can be solved by increasing the accelerating voltage. However, by increasing accelerating voltage which is proportional to interacting volume it will penetrate more inside the sample.

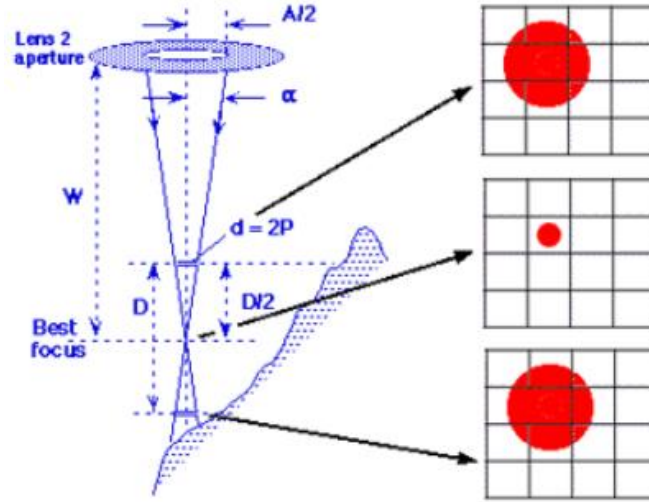


Figure 2-18: Region of image in effective focus [56]

SEM spatial resolution refers to the smallest observable object in the image. When working with high magnifications, the resolution should be high enough to distinguish the objects in small ranges. For increasing the resolution, the beam diameter should be as small as possible to reduce the probability of overlaps of signals coming from adjacent areas.

Beam diameter drives from Eq. 2.32 where k is a constant, i is the current beam, E_0 is the accelerating voltage, and α is divergence angle

$$d = k \sqrt{\frac{i}{E_0} \cdot \frac{1}{\alpha}} \quad \text{or} \quad d = k \sqrt{\frac{i}{E_0} \cdot \frac{W}{r}} \quad (2.33)$$

It is expected that by increasing accelerating voltage or divergence angle the beam diameter increases too which leads to increasing the resolution and since the divergence angle is dependent on work distance and aperture size, these factors may also have an effect on resolution.

SEM has the power to provide details about the morphology of matter. The high resolution available in modern SEMs provides the option to gain considerable information about what is the structure, how small are the grains or crystallites and how the crystals are oriented. Specifically, “Channeling Contrast” which is also called “Orientation Contrast” can be used to get resolutions based on the orientation of crystals in the sample [54].

Another connected matter to the orientation is Water Contact Angle (WCA). This is important when hydrophobicity is desirable. As the orientation of the crystals means how the atoms (or ions) are arranged on one specific surface, including density of atoms in that specific plane, this basically

affects WCA and hydrophobicity which is reported for cerium oxide [57]. So, to observe orientation and grain size as well we were motivated to do some SEM tests.

2.7. XRD

X-ray diffraction method which allows to have a better visualization through matters specially in large thickness and size and widely used for studying the real structure of crystals developed based on Bragg's law. According to this law the path difference between x-ray beams scattering from adjacent planes can be deduced from Eq. 2.34 [58]. For having a constructive interference between these scattered beams, the path difference should be an integer multiple of wavelengths, which gives the Bragg equation.

$$n\lambda = 2d \sin \theta \quad (2.34)$$

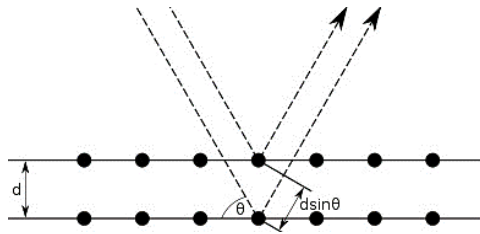


Figure 2-19: Bragg diffraction. Two rays with known wavelength and phase reach a crystal and scattered off from different layers. θ is the incident beam angle and d is the inner plane distance [58].

d is the inter planer distance and θ is the incident beam angle. To predict the possible diffraction direction, for a specific incident wavelength and a cubic crystal with a unit cell size and inter-planar distance d , all the possible Bragg angles to have diffraction from the planes (hkl) achieve from Eq. 2.3.

$$\frac{1}{d^2} = \frac{h^2+k^2+l^2}{a^2} \quad (2.35)$$

$$\sin^2 \theta = \frac{\lambda^2}{4a^2} (h^2 + k^2 + l^2) \quad (2.36)$$

CeO_2 lattice constant is 5.407 \AA with the lattice parameters of $(a=b=c)$. It has a symmetry of $Fm\bar{3}m$ (full space-group symbols $F4/m\bar{3}2/m$. Periodic arrangement of atoms and electrons present are responsible for scattering and over- all scattering from crystal is the sum of scattered beam from all electrons [59] [60].

Any atom with specific atomic number Z has a definite power of scattering which is called scattering factor f which is the sum of scattering amplitude from all presented electrons in the atom (or ion). In CeO_2 with a fluorite fcc crystal structure there are four cerium atoms

and eight oxygen in each unit cell which need to be considered in finding form factor as a combination.

Table 2-4: The atomic factor coefficients for Ce⁴⁺ and O¹⁻ ions [61]

Element	A1	b1	a2	b2	a3	b3	a4	b4	c
O ¹⁻	4.19	12.86	1.64	4.17	1.53	47.02	-20.3	-0.01	21.9
Ce ⁴⁺	20.32	2.65	19.81	0.22	12.12	15.79	0.14	62.23	1.59

In calculation of form factor according to the formula below, some scatterings will be destructive and cancel out each other which is known as extinction rules [62].

$$F_{hkl} = f_n \exp(2\pi i(hx_n + ky_n + lz_n)) \quad (2.37)$$

In an FCC crystal, considering the position of atoms, if all (h, k, l) be odd or all even there will be non-zero solution for Eq. 2.37, otherwise it will be zero because of destructive scattering and at the end there will be no diffraction. Diffraction condition is achievable by replacing (x, y, z) with the position of ions in FCC structure and then expanding the above formula of structure factor will lead to these conditions:

$$h + k = 2n, \quad h + l = 2n, \quad k + l = 2n$$

This means that the plane indices shall not be mixed (only all odd or all even indices are allowed diffractions). This is applicable for both Ce and O ions separately at the same time and therefore there is no diffraction if these conditions are not met. More specifically for CeO₂ crystal, by substituting the position of Ce and O ions as the values of (x_n, y_n, z_n), the general formula will be simplified more. The result of calculations summarized in Table 2-5.

Table 2-5: structure factor for allowed planes in diffraction

$h^2 + k^2 + l^2$	(h,k,l)	2θ	multiplicity	$\sin \theta/\lambda$	$f(\text{Ce}^{4+})$	$f(\text{O}^{1-})$	F^2 (hkl)	Normalized F^2 (hkl)
1	100	16,38	6	0,09	51,97	7,99	0	0,00
2	110	23,25	12	0,13	50,06	7,20	0	0,00
3	111	28,57	8	0,16	48,39	6,57	299791	0,45
4	200	33,11	6	0,18	46,9	6,05	225210	0,34
5	120	37,15	24	0,21	45,54	5,68	0	0,00
6	121	40,85	24	0,23	44,37	5,25	0	0,00
8	202	47,52	12	0,26	42,17	4,65	358098	0,54
9	221	50,60	24	0,28	41,27	4,40	0	0,00
9	300	50,60	12	0,28	41,24	4,40	0	0,00
10	130	53,55	24	0,29	40,37	4,18	0	0,00
11	113	56,39	24	0,31	39,57	3,98	601426	0,91
12	222	59,14	8	0,32	38,84	3,81	200477	0,31
13	230	61,81	24	0,33	38,15	3,65	0	0,00
14	123	64,42	48	0,35	37,51	3,50	0	0,00
16	400	69,48	6	0,37	36,35	3,24	130867	0,20
17	232	71,94	24	0,38	35,82	3,13	0	0,00
17	410	71,94	24	0,38	35,82	3,13	0	0,00
18	330	74,37	12	0,39	35,31	3,03	0	0,00

Chapter 3

Methods

3.1. Sample preparation

3.1.1. CeO₂ on Glass substrate

The samples were provided as thin films on glass substrate with different parameters including thickness, O₂/Ar ratio, total pressure, and deposition rate using magnetron sputtering technique in IFE Oslo.

Table 3-1: Description of the CeO₂ on glass substrate samples (IFE)

Sample No	Thickness (nm)	O ₂ /Ar	Total pressure (Pa)	Deposition rate (nm/min)
58	100	50/160	0.5	5
59	200	50/160	0.5	5
55	400	50/160	0.5	10
56	600	50/160	0.5	10
60	50	50/160	0.5	5
61	50	24/160	0.5	5
62	50	11/160	0.5	5
63	25	50/160	0.5	5
64	25	24/160	0.5	5
65	25	11/160	0.5	5
70	100	11/160	0.25	5
71	50	11/160	0.25	5
72	50	8/160	0.25	5
73	50	6.5/160	0.25	5

3.1.2. CeO₂ on Si substrate

For this research work CeO₂ thin films on Si substrate which were prepared in IFE in Oslo were used. The CeO₂ samples were provided as thin films of different thickness on Si support (N-doped silicon monocrystalline wafers (100 plane index). These flat samples with the regular size of 1×1 cm² as shown in Figure 3-1 annealed in four different temperatures (400°C, 600°C, 800°C, 1000°C) for 30 minutes. Then for increasing hydrophobicity of samples they have been covered by Polydimethylsiloxane (PDMS) by placing in oven simultaneously with samples for 17 hours.

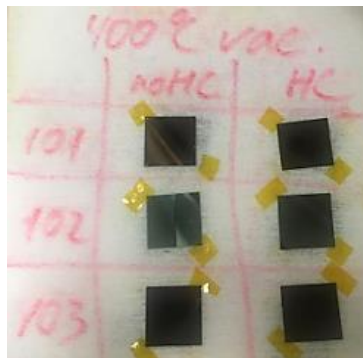


Figure 3-1: CeO₂ thin films on Silicon substrate (IFE)

Table 3-2: Description of the CeO₂ on Si substrate samples (from IFE)

Characteristics	Batch 101	Batch 102	Batch 103
Deposition pressure, Pa	0.5	0.25	0.5
O ₂ /Ar ratio	50/160	7/160	50/160
Thickness (profilometer), nm	200	400	50
Heat treatment in air, °C	400, 600, 800, 1000	400, 600, 800, 1000	400, 600, 800, 1000
Heat treatment in vacuum, °C	400, 600, 800 (Delamination at 1000)	400, 600, 800, 1000	400, 600, 800, 1000
Number of various samples in a group	2 (with and without HC)	2 (with and without HC)	2 (with and without HC)
Reference	+	+	+

3.2. Raman Spectroscopy

RENISHAW inVia Raman microscope system was used for the Raman studies of this research work.



Figure 3-2: RENISHAW inVia Raman microscope system

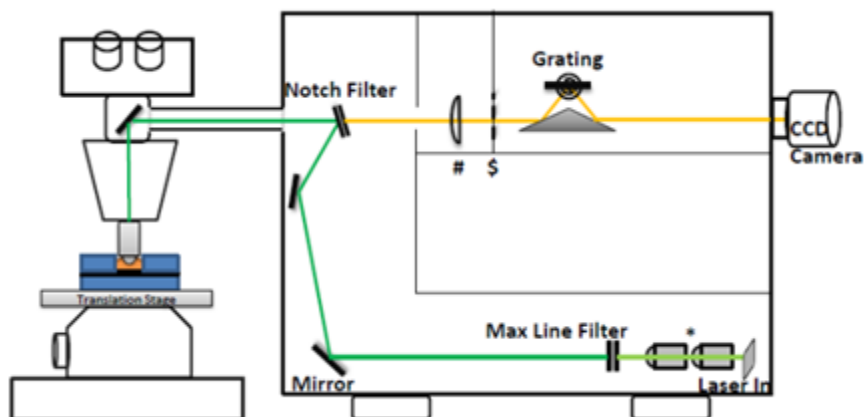


Figure 3-3: Schematic image of Renishaw Raman microscope set up

It is equipped with three laser sources with 532nm 447nm and 630nm wavelengths. It also includes a set of mirrors, shutter, pinhole filter for turning the red laser from a line to spot, mirrors to direct the laser up and into the microscope, microscope with an objective it focuses the light with an objective in the sample and hopefully inelastic scattering occurs which is collected with the same objective, filter rejects the incident light and Rayleigh scattering and to transfer inelastic scattering light, lens focuses onto slit, diffraction grating and a CCD for recording images.

3.2.1. CeO₂ on glass support

The samples consist of CeO₂ thin films on glass support were studied with 532 nm laser, x100 magnification, 100 % laser power, 100s acquisition time. Several spectra per sample were obtained to ensure reproducibility. Measuring in the different parts of the sample, ensure sample homogeneity. The spectra were very similar, also in intensity if the focus did not change. The achieved spectra in WiRE (5.5 version) analysed with Origin software.

3.2.2. CeO₂ on Si support

Renishaw inVia Raman microscope was used for Raman studies to find PDMS on surface of the CeO₂ thin films. The samples were measured with 532 nm laser, x50 (or x100) magnification, 10-100 % laser power, 10 s acquisition time. Several spectra were obtained to ensure reproducibility and homogeneity.

3.3. Calculation methods (Polarized Raman curves)

At first step, we used MATLAB and simulated the intensity of scattered beams using Euler angles. The simulated curves were compared to the experimental ones. The PRS for Si supports were also obtained for method validation. Considering the three low index planes of CeO₂ and the Si (100), the calculations was mainly focused on (100),(111) and (110)planes. first assuming crystal axes (xyz) were exactly aligned with lab frame coordinates (XYZ). This of course can be verified later as the results of the experiments are obtained. For this plane, z and Z are parallel and angle θ is equal to zero. Similarly, χ is also zero. And the angle φ changes as we rotate the sample. Next, as the strongest peak in XRD patterns was (111) so the second assumption was this plane. Euler angles for this plane were calculated using the cosine rule. The following rule is used to calculate the angle between two planes in crystals (cubic structures):

$$\cos\alpha = \frac{h_1h_2+k_1k_2+l_1l_2}{\sqrt{(h_1^2+k_1^2+l_1^2).(h_2^2+k_2^2+l_2^2)}} \quad (3.1)$$

This leads to choose (54.74, φ , 54.74) as Euler angles of (111) plane. and (45°, φ , 0) for (110) plane. The model calculations have been shown in Figure 3-4 to 3-6.

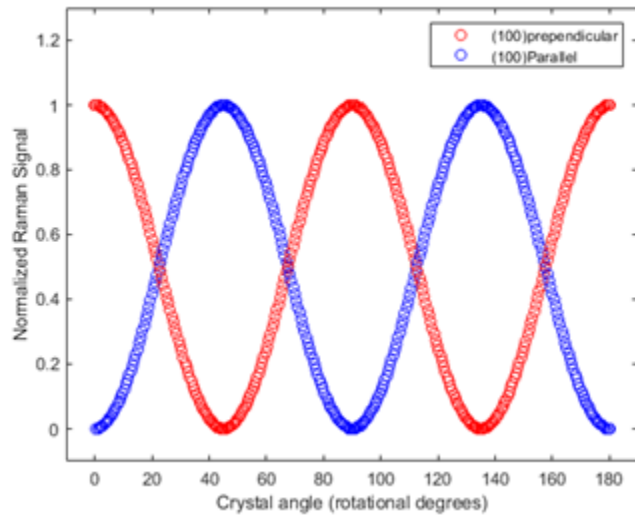


Figure 3-4: Calculated results for polarized Raman experiment for (100) plane of cubic structure crystal

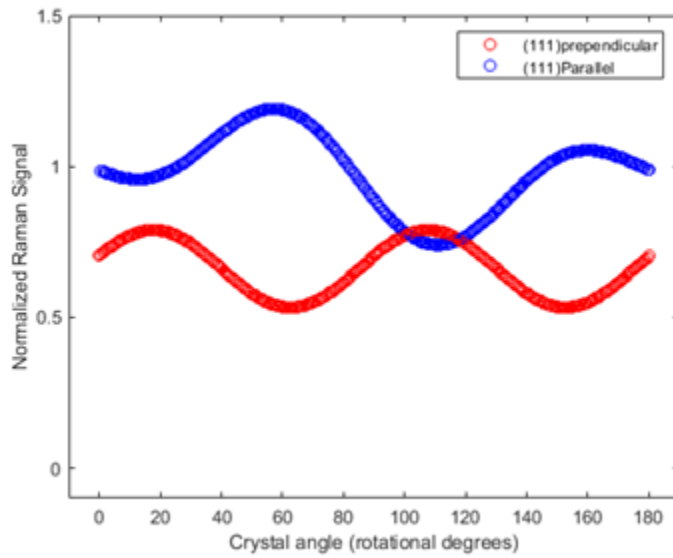


Figure 3-5: Calculated results for polarized Raman experiment for (111) plane of cubic structure crystal

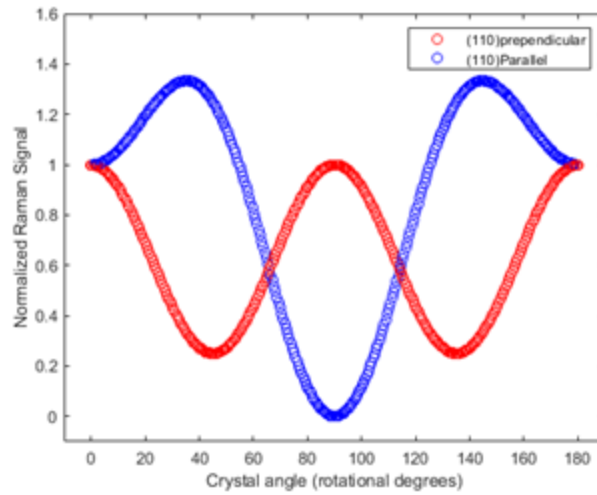


Figure 3-6: Calculated results for polarized Raman experiment for (110) plane of cubic structure crystal

PRS (backscattering geometry) is used to determine orientation of the crystal. The incident light reaches the sample aligned with Z-direction and scattered back in the same direction \vec{Z} and it has a default polarization in X direction (in our set up), however the polarization of scattered light is tunable by using polarizer. So, to have a perpendicular ($Z(XY)\vec{Z}$) and parallel ($Z(XX)\vec{Z}$) polarization where the $(AA)^*$ indicate the polarization of incident light and scattered light respectively, a polarizer or a polarizer plus a one-half wave plane have been selected from analyzer kit of the instrument to change the polarization axis.

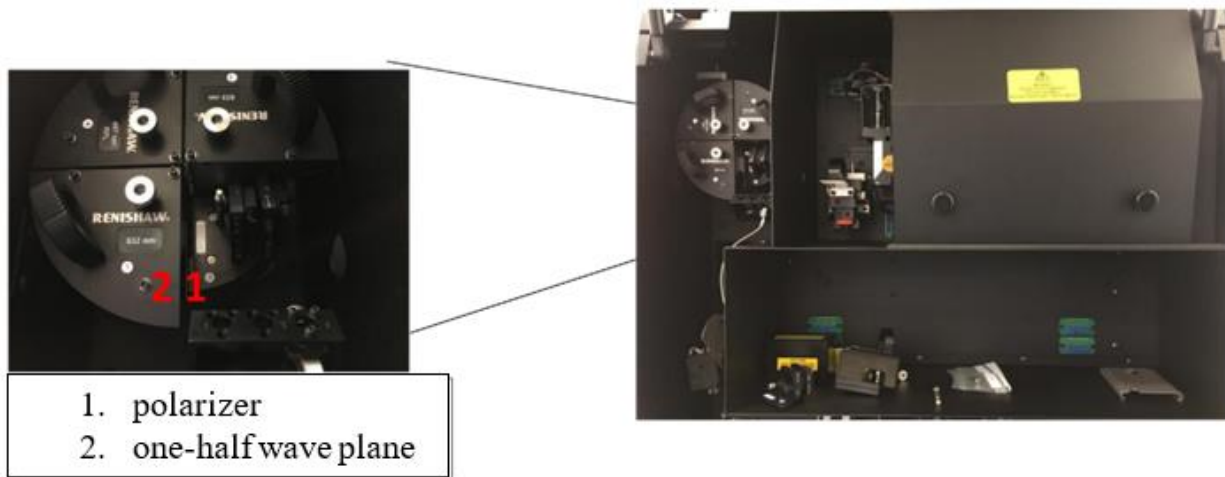


Figure 3-7: Raman spectroscopy set up after inserting polarizer and $\frac{1}{2}$ wave plane

CeO_2 on silicon (100) substrate have been studied with this method for finding about the orientation of CeO_2 crystal(s). The test samples have been taken from a group which have been annealed in different temperatures (400°C, 600°C, 800°C, 1000°C) in two different environments (air, vacuum). At the same time, we took SEM images of the same samples for having better

understanding and comparison. Raman scattering was taken by inVia Raman microscope by Renishaw Inc. It has a polarization option which enables the control of both laser and spectrometer polarization (polarizer/analyzer). 532 nm (green) DPSS (Diode pumped solid state) laser which is polarized in x -direction by default with 5-10% power was used for polarized Raman studies. A low power laser used because of the strong peak of Si and otherwise it became over scale, as we wanted to keep both Si and Ceria peaks in the spectra as modelling of experimental Si spectra was used for comparison. A 50X objective was used for focusing laser spot onto the c -plane (001) faced surface.

The rotation of the sample was performed as follows: a circle was drawn on a blank sheet of paper and equally divided. The marked Ceria/Si sample was mounted on the fixed still slide and then was placed on the two marked paper sheets. Each time the sample was rotated by 10 (or 45) degrees in sequence and totally rotated by 180 degrees around the c -axis of the crystal. This makeshift setup is illustrated in Figure 3-8 (a).

Five rotational degrees used ($0^\circ, 45^\circ, 90^\circ, 135^\circ, 180^\circ$). To reduce errors, Raman measurements have been done in four different positions for each rotational degree. Variation in Raman intensity of F_{2g} mode both in Si support and CeO_2 films with the variation in Raman light polarization (parallel, perpendicular) / sample position depends on the mutual orientation of crystal axes and Raman light.

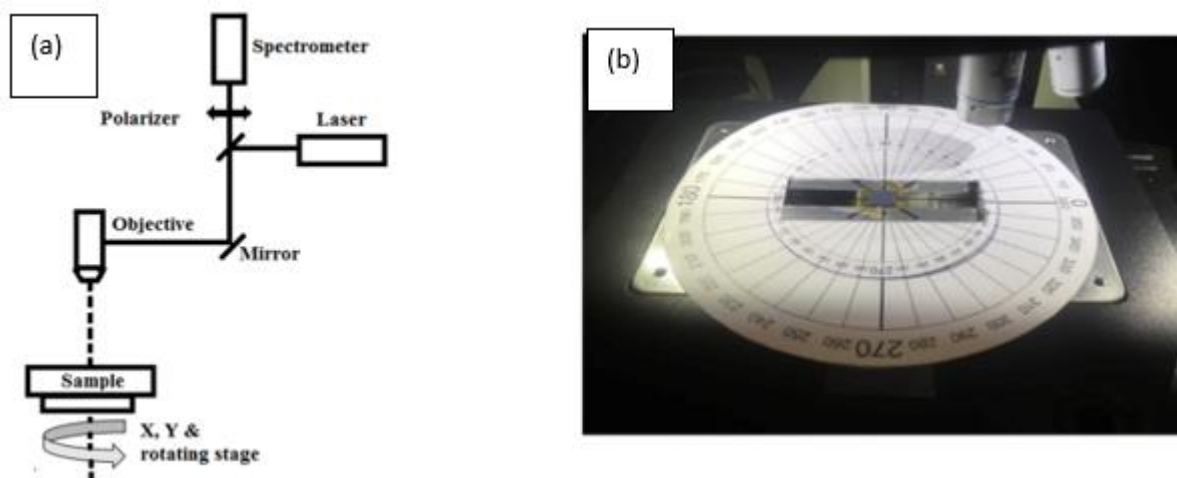


Figure 3-8: a) Schematic procedure of Polarized Raman experiment's set up. b) Sample mounted on angle marked blank plate inside Raman chamber

3.4. XRD

X-ray diffraction patterns were obtained using D8 Advance Eco Bruker instrument in flat plate Bragg-Brentano geometry. The instrument was equipped with Cu-source with the wavelength 1.54\AA and 0.6 mm divergence slit. cerium oxide thin films were fixed with Vaseline on the holders and mounted on the rotating sample stage (Figure 3-9). By selecting desired diffraction angle in software, the diffraction patterns were achieved.

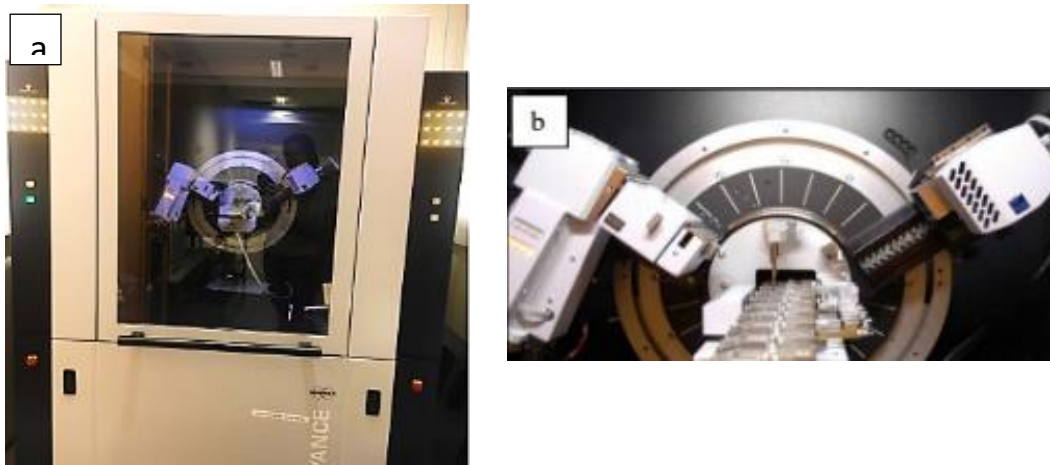


Figure 3-9: XRD for crystal characterization. a) D-8 Bruker b) CeO_2 thin films placed on holders located under x-ray light.

3.5. WCA

To measure the water contact angle with the surface of CeO_2 -PDMS thin films, the samples were fixed on a flat plate and labeled. A drop of Distilled water was placed on the samples using a micropipette to have a fixed volume of water ($100\mu\text{m}$). A high-resolution camera is used for taking the images. This experiment was repeated two times to eliminate the errors. Two important point which must be considered are to take the images instantaneously after inserting water drop to avoid change of drop shape because of evaporation in room temperature and second to use micropipette instead of simple pipette for taking the same amount of water.

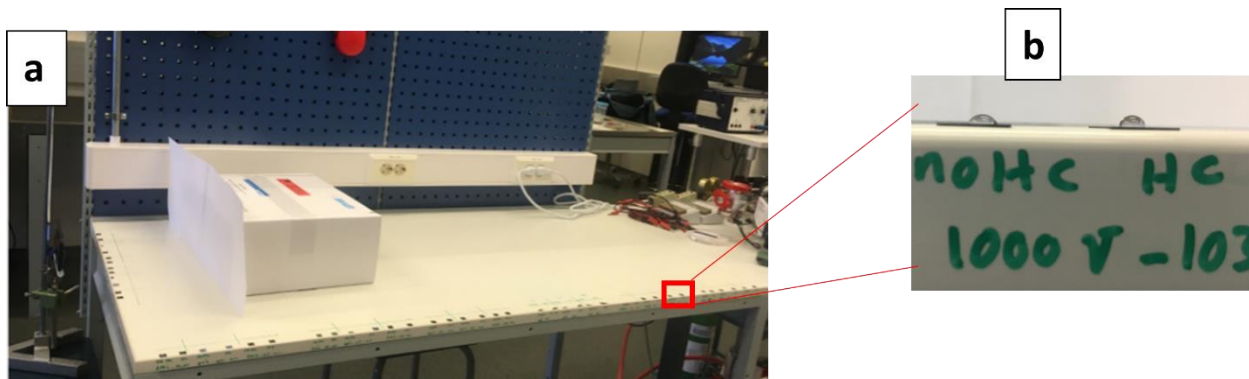


Figure 3-10: a) WCA experiment's set up. b) Sterile water drops on the CeO₂-PDMS thin films

IC measure software is used for accurate angle measurements on images. As the effect of cleaning materials as ethanol on PDMS, were not clear for us we were not able to clean the contaminations. So, the effect of probable contaminations and environmental hydrocarbons on the results should be considered.

3.6. SEM

In this research work, Zeiss Supra 35VP Field Emission Gun Scanning Electron Microscope (FEG-SEM) (Figure 3-11 c) has been used to analyze the samples and the CeO₂ samples were coated with Pd first, for making the samples conductive.

The thin films which mainly consists of cerium oxide nanoparticles were deposited using magnetron sputtering on silicon in 1x1 cm². The sample pieces were cut from original samples to fit on holders of SEM chamber. As Ceria is non-conductive a 15 nm thick Palladium coating was applied on the samples to make them suitable for electron beam. Leica EM ACE600 coater (Figure 3-11 b) has been used for sputtering coating. This essential technique increases the signal to noise ratio by increasing the number of secondary electrons that can be detected from the surface of the specimen to be detected with the SEM detectors.

Coated samples were placed in the high vacuum SEM chamber and Secondary Electron (SE) imaging was used to study the morphology and size of the Ceria particles. The different magnifications have been used to gain better insight observation.

The working distance of 10mm was chosen for imaging when using secondary electron detector however a working distance of 5mm used while using "in lens" detector which leads to better resolution. It was useful for films with smaller particle size to be clearer. For having better comparisons, the images were taken with 1000x, 5000x, 50000x and 80000x magnifications. The particle sizes of a few samples were measured using imagej tool to compare with results from XRD pattern.

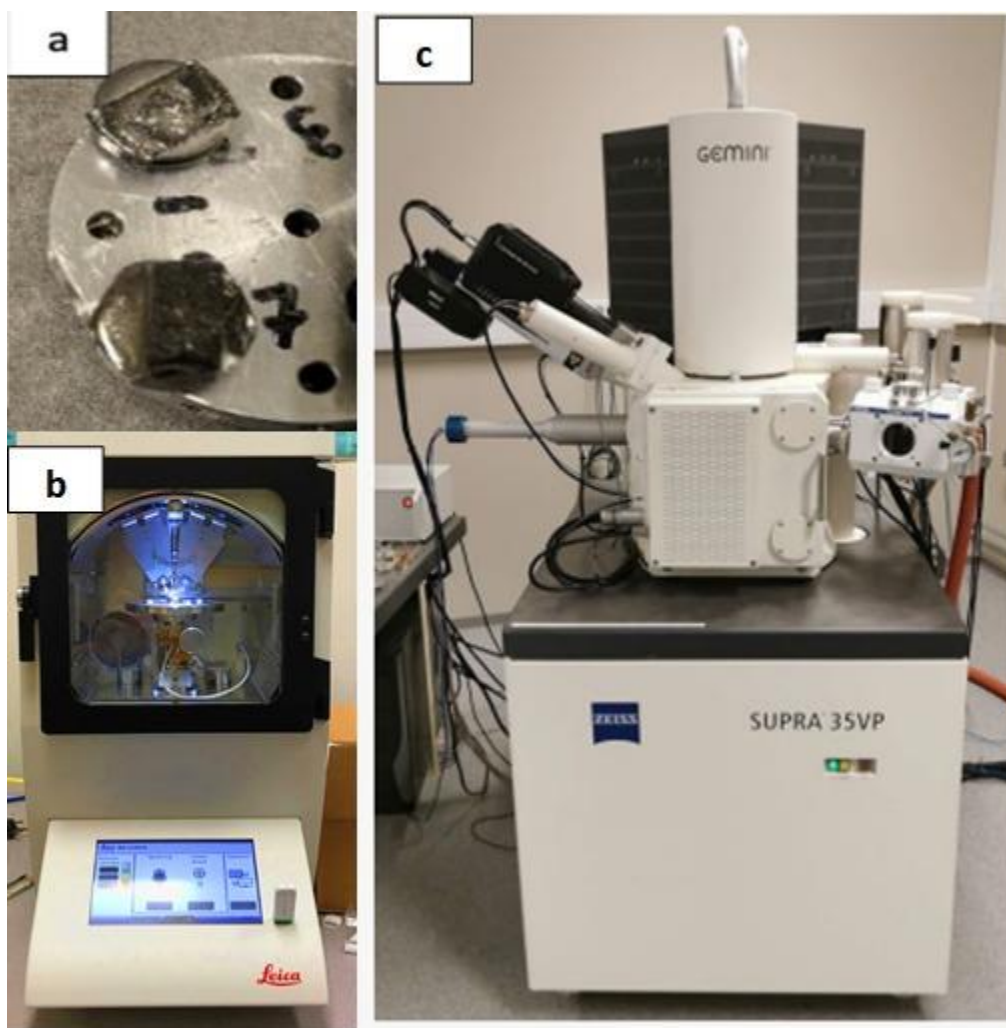


Figure 3-11: a) Two samples in SEM holder fixed with conductive carbon tape. b) Leica EM ACE600 coater c) Zeiss Supra 35VP Field Emission Gun Scanning Electron Microscope at UiS, 15 kV acceleration voltage, 30- μ m aperture is used for Getting images with SEM.

Chapter 4

Results and Discussions

4.1. Factor group analysis

CeO₂ crystal with a cubic fluorite structure corresponding to the space group O_h⁵ (Fm $\bar{3}$ m) which belongs to 225 group number. It consists of Ce and oxygen atoms which are positioned at (0,0,0) and (1/4,1/4,3/4) respectively with site symmetries of O_h (m $\bar{3}$ m) and T_d (43m) [63]. Then refer to character table related to O_h and T_d, the translation modes are F_{1u} and F_2 which using correlation table transforms as F_{1u} and F_{2g} mode.

Table 4-1: Positions of Ce and O atoms in ceria crystal [63]

Element	Wyckoff	x y z	Point group	Site symmetry
Ce	4a	0 0 0	m $\bar{3}$ m	O _h
O	8c	1/4 1/4 3/4	$\bar{4}$ 3 m	T _d

Using the character table of O_h⁵, Group theory predicts a triply degenerate Raman active optical phonon (F_{2g} symmetry) and one infrared-active optical phonon (F_{1u} symmetry), which presents either LO or TO character (with different wavenumbers) depending on the relative propagation/polarization directions of the mode [64]. The F_{2g} band located at 464 cm⁻¹ belongs to symmetrical stretching vibration of the Ce–O₈ unit [65] a weak band around 1180 cm⁻¹ corresponds to the LO mode (Raman inactive and 595 cm⁻¹ labelled as 2LO. The TO mode is located at 272 cm⁻¹. Other second-order features at 264, 366, 550, 600, 676, 935 cm⁻¹ were assigned to phonon overtones from the X and L points on the Brillouin-zone boundary [66]. Annealing in vacuum at high temperatures can possibly produce Ce³⁺ species (with hexagonal D_{3d} Ce₂O₃ structure as the extreme case). Ce₂O₃ has peaks as 409, 189, 103 cm⁻¹ as it is shown in Figure 4-1 [67].

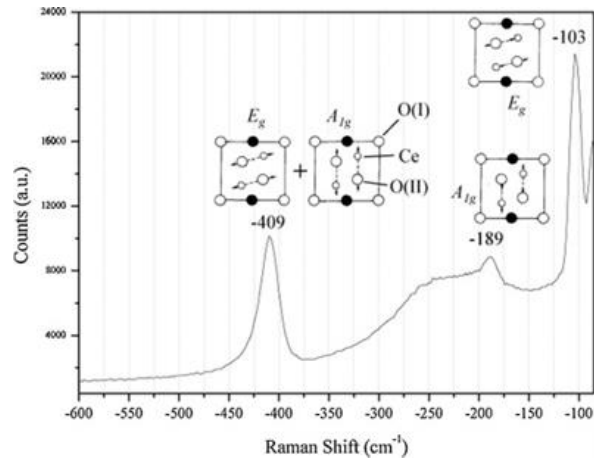


Figure 4-1: Raman spectrum of Ce₂O₃ [67]

4.2. Raman study of CeO₂ films on glass substrate

The purpose of this study was to investigate the effect of various synthesis parameters on the Raman spectra of CeO₂ and thus on their microstructure. Furthermore, quantum effects for the thinnest films could have been expected. To have a better comparison of peak intensity, the experimental data were normalized to the main reported peak of glass (around 1100 cm⁻¹) as it is shown in Figure 4-2.

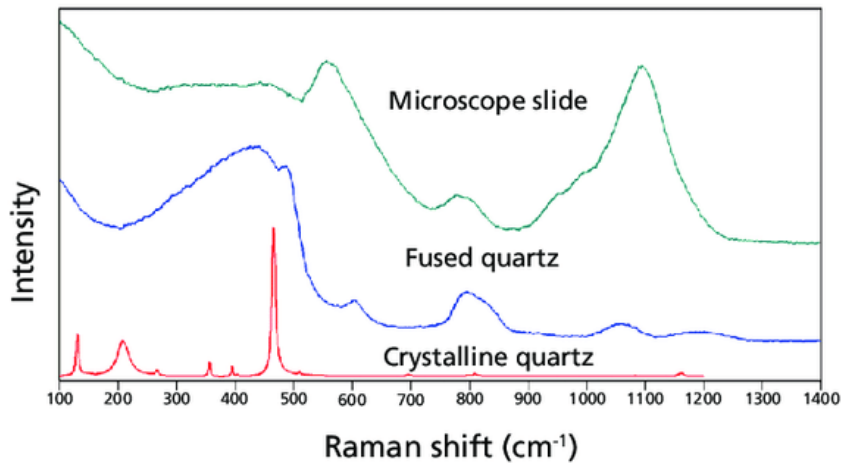


Figure 4-2: Raman spectra of crystalline and fused quartz and a glass microscope slide [68].

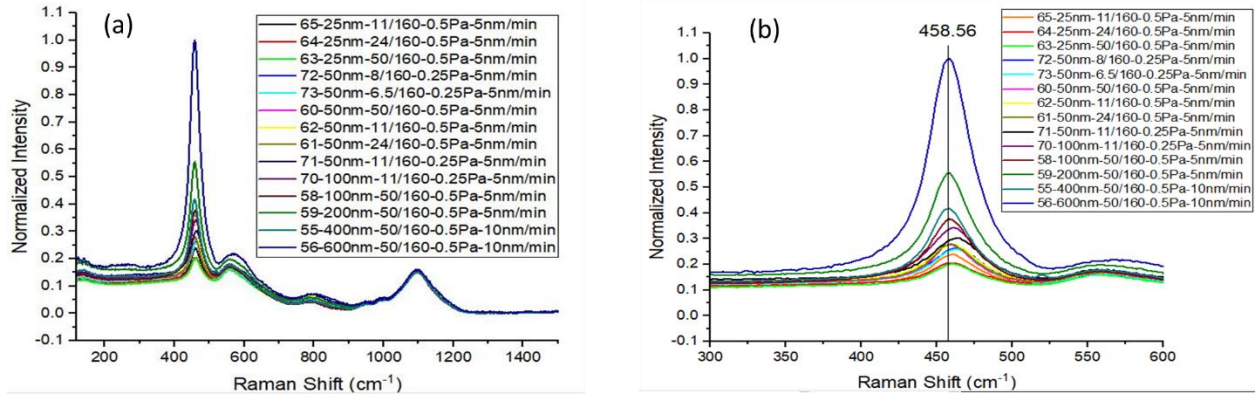


Figure 4-3: Normalized Raman spectra for samples with different parameters for (a): full range of energy (b): expanded view of CeO₂ peak. Name of graphs includes parameters respectively (sample number, thickness, O₂/Ar ratio, pressure, deposition rate).

In Figure 4-3, the Raman spectra of all the samples with different properties as thickness and deposition parameters is illustrated, however for better review of achieved Raman spectra, comparisons are divided into three main groups based on change of only one parameter of thickness, O₂/Ar ratio and total pressure. Some small peak shifts of ceria have been observed in samples prepared with different parameters.

4.2.1. Dependency of Raman peak shift and intensity on film thickness

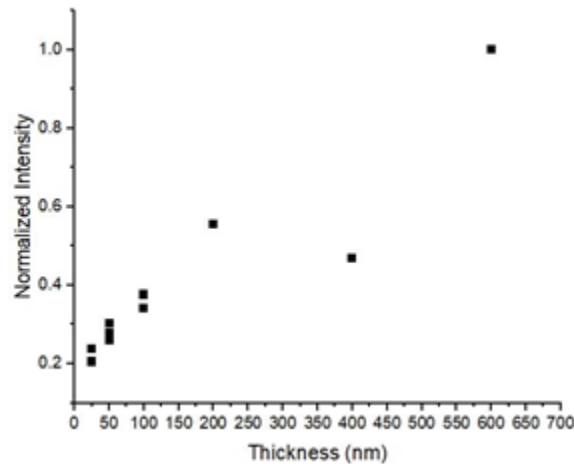


Figure 4-4: Thickness vs. normalized intensity for all samples. Samples with same thickness shows similar intensities irrespective of their different deposition parameters

In Figure 4-4 CeO₂ Raman peak intensity vs. film thickness has been represented. Almost all samples with the same thickness have similar intensities and by increasing film thickness the intensity increases as well. This behavior is expected as a direct consequence of the increased

sample volume and thus the number of scattered photons. The only exception is sample 55 with 400 nm thickness. It is suggested that this behavior can be because of experimental errors or defects on the sample. For this set of experiments laser light with 100% power have been used. For eliminating probable saturations that seems to be around 600 nm films, one suggestion could be decreasing the power. The saturation can be related to the used objective lens and beam spot size as well. Introducing the light with smaller spot size means covering less volume of the sample in focal point and that leads to less saturation.

Raman spectra was performed for all samples and then graphs with one variable were compared to better understand the results. However, in few cases there are more than one variable that is due to the problems in the construction step. Figures 4-5a) and e) show the dependance of the peak position on the sample thickness for the samples prepared at 50/160 O₂/Ar ratio and 0.5 Pa pressure. We can see that all the samples demonstrate a red shift from the 464 cm⁻¹ equilibrium position of CeO₂ powder [69]. The shift is the smallest (-4.5 cm⁻¹ for the thinnest sample and is larger -5.5 cm⁻¹ for the thicknesses > 50nm) although the difference is very small. This shift indicates the increase in the Ce-O distances, i.e., increase in the lattice parameter for these films where the latter can be caused by introducing larger Ce³⁺ cations or by defects [10]. Red shift is also characteristic for smaller particle sizes for powdered samples as discussed in literature [70]. Thus, it can be suggested that at these synthesis parameters thicker samples possess somehow smaller particles with perhaps larger lattice spacing. The shift does not depend on the deposition rate (5 nm/min on Figure 4-5 a) vs. 10 nm/min on Figure 4-5 e)). For the same pressure (0.5 Pa)

At lower O₂ concentration (24/160 O₂/Ar ratio, Figure 4-5 c) we observed similar shifts indicating that such O₂ concentration difference (50-24 O₂ relative concentration) does not make a considerable effect on the microstructure of the resulting films, but the shift is already smaller for the 11/160 O₂/Ar ratio and the thinnest sample, -2.3 cm⁻¹ (Figure 4-5 d).

Figure 4-5 b shows that for the samples prepared with the lowest O₂ concentration (11/160) and at the same time at lower pressure of 0.25 Pa, the shift is smaller being -3.3 and +1.3 cm⁻¹ that could evidence negligible lattice parameter modification and larger particle size of the films. The effect of these parameters is further investigated separately.

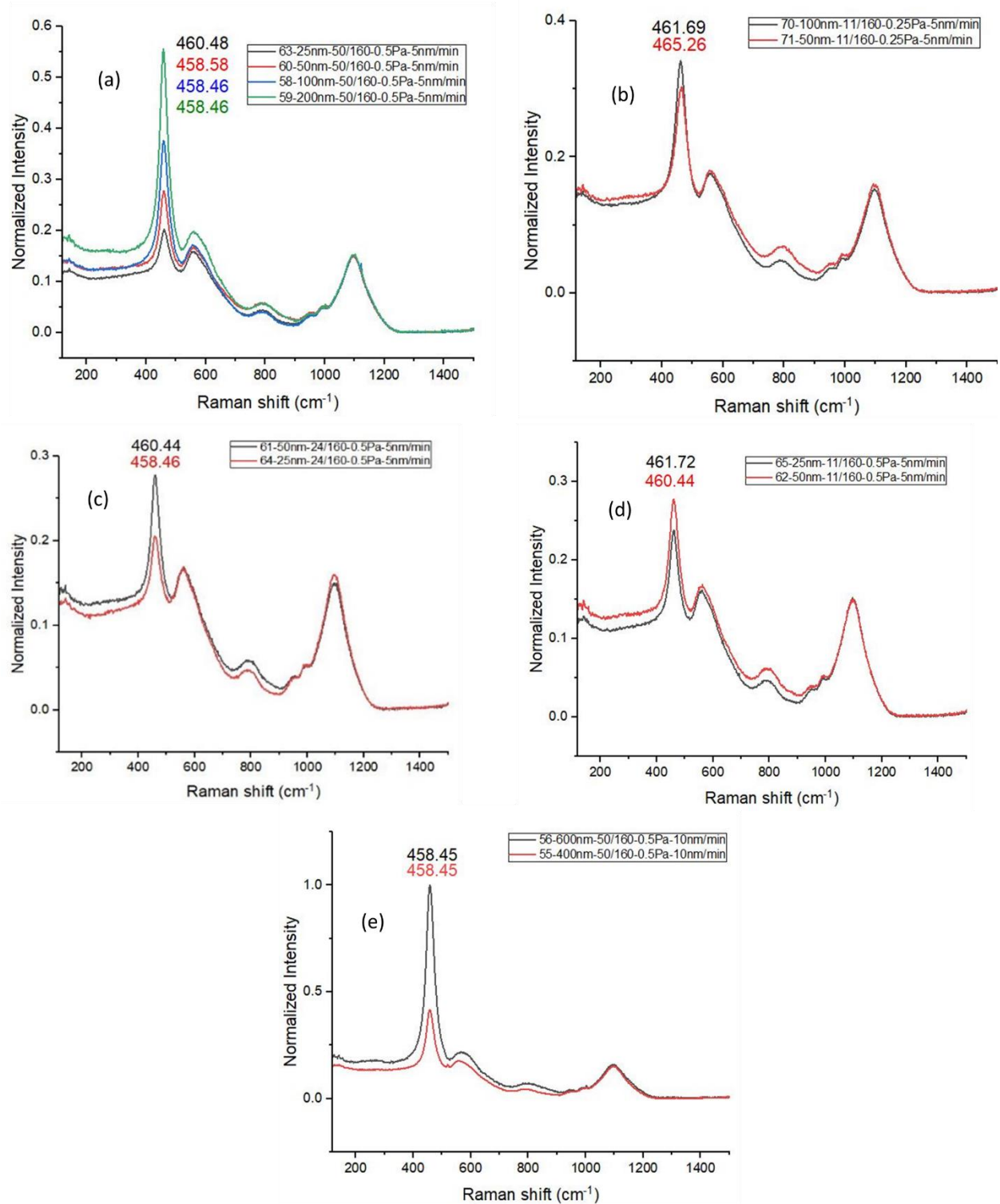


Figure 4-5: comparison of CeO₂ peak intensity for samples with different thicknesses. Other parameters are same for each group. There are some shifts and intensity changes in ceria peak.

4.2.2. Dependency of Raman peak shift on O₂/Ar ratio

To single out the effect of O₂/Ar ratio on the ceria peak shift, we compared the samples which had changes in O₂/Ar ratio while the other deposition parameters kept same. The evaluation of further data showed that changing the O₂/Ar ratio in lower total pressure (0.25 Pa, Figure 4-6 (a)) has less significant effect on peak shift from the 464 cm⁻¹ ceria peak demonstrating +1.3 to - 2.6 shifts without a clear dependence on the concentration. It can be seen from Figure 4-6 (a,c) that there are shifts about 3 cm⁻¹ between samples prepared in 0.25 Pa and 0.5 Pa with the larger shifts from 464 cm⁻¹ for the latter group. Thus, it seems that the largest shifts are induced on the samples prepared at larger total oxygen concentrations. By comparing Figures 4-6 (b) and (c) it can be deduced that variation in O₂/Ar ratio has more effect on samples with less thickness.

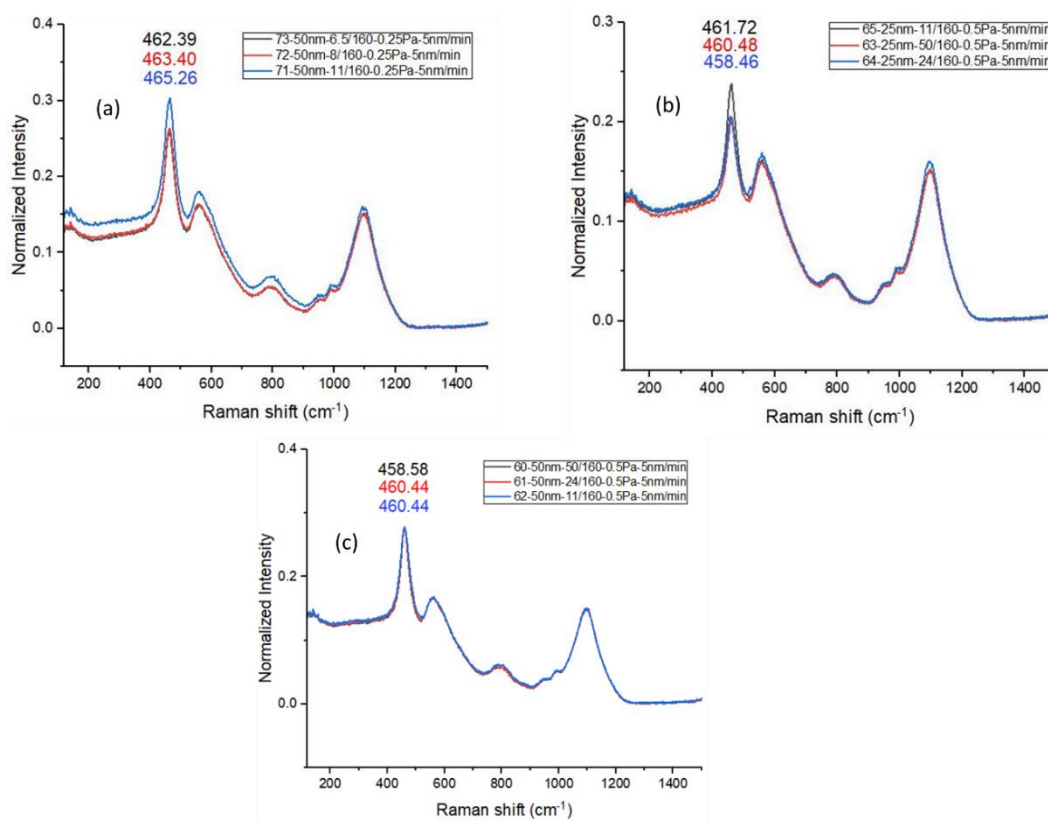


Figure 4-6: comparison of CeO₂ peak intensity for samples with different O₂/Ar ratio. Other parameters are same for each group. There are some shifts and intensity changes in ceria peak.

Sample 64 demonstrates also the features at 550 and 595 cm⁻¹ that originate from O²⁻ vacancies and replacement of cerium (IV) atoms by cerium (III) atoms or impurity atoms in the bulk, respectively [70]. Note also that this sample has the largest shift from the 464 cm⁻¹ position. The new peak can also be related to quantum size effect in smaller size nanoparticles [10]. It is suggested that the thinner films might demonstrate quantum size effects similarly to nanoparticles. As it can be seen in Figure 4-7, in CeO₂ nanoparticles, decreasing crystallite size increases FWHM.

FWHM vs. crystallite size follows an inverse relationship. It is proposed that these changes arise from the smaller phonon mean path and hence life-time in smaller particles (confinement). It is also suggested that failures in structure play a role in broadening the peak. Observed red shift is attributed to the effect of strains arising from curvature of nano crystals. In addition, a weak peak near 560 cm^{-1} is stronger for smaller particle size [10]. So the new peak in the Raman spectra of 64 sample could be related to quantum size effect

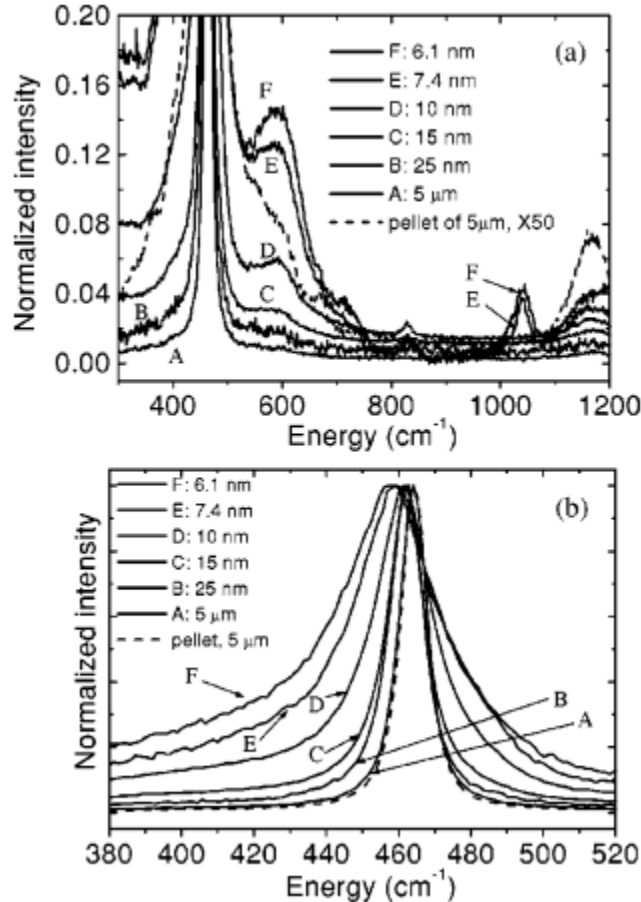


Figure 4-7: Normalized Raman spectra of ceria nanoparticles and the bulk material. a) the full range of energy studied, b) expanded view. It is showing that the peak position, linewidth, and line shape is changing with respect to particle size [10].

4.3. Raman study of CeO_2 on Si substrate

The aim of studying this group of samples was to understand wheatear PDMS peaks (shown on Figure 2-10) could be detected by RS in addition to learning about redox transition of cerium oxide. To subtract the effect of the strong peak of Si (substrate) at 521 cm^{-1} on our observations, the measurements divided in two separate regions, below 480 cm^{-1} and above 800 cm^{-1} .

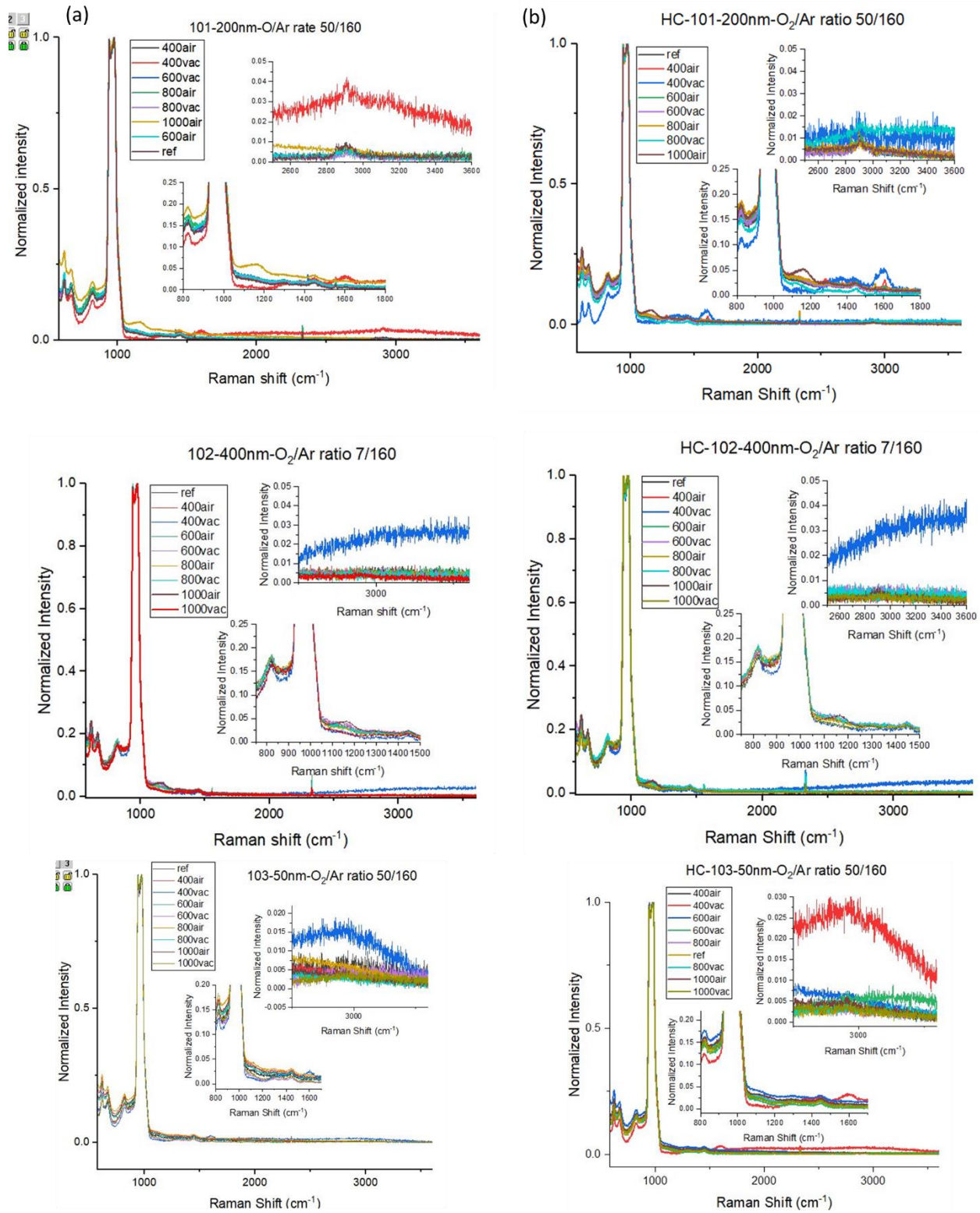


Figure 4-8: Comparison of Raman spectra of samples annealed in different temperatures (a) left hand side without PDMS (b) right hand side with PDMS. Reference samples are plotted inside.

Figure 4-8 illustrates the higher range of Raman spectra for CeO₂ samples on Si Substrate. They are divided in two main groups of the samples including PDMS on the surface which are placed on the left side of the Figure, and the samples without PDMS which are placed on the right side of the Figure. Each column consists of three separate figures which are ordered up to down by the batch number of 101 (200nm), 102 (400nm), 103 (50nm).

A few strong and weak peaks were observed in the Raman Spectra which appears in Figure 4-8. Silicon has only one first order Raman active phonon located at the Brillouin-zone. The first order Raman (Stokes) spectrum consists of one strong peak at 520 cm⁻¹ arising from the creation of the triply degenerate, long wavelength transverse optical phonon (TO). The second order spectrum is much weaker with features ranging from 0 – 1050 cm⁻¹ (around 301 and 976 cm⁻¹). Higher order features, assigned as 3TO and 4TO scattering, are evident in the 1400 – 1600 cm⁻¹ and 1800–2000 cm⁻¹ region of the spectrum and combination bands can be found around 1000 -1250 cm⁻¹. While this provides a rich spectral photonic landscape for silicon, the intensity of these bands makes it more difficult to observe the weaker spectral features considered in this work [71]. The sharp transition at ~2330 cm⁻¹ comes from ambient nitrogen (molecular) gas. The band at ~1450 cm⁻¹ is assigned as the third order silicon TO phonon, the ~1550 cm⁻¹ band arises from molecular oxygen. Analyzing the data from Raman spectra indicates the absence of peaks related to the Ce₂O₃ (shown on Figure 4-1) and PDMS (shown on Figure 2-10). However, there are some shifts in Raman peak for the samples which are annealed in vacuum and air. In the lower range of spectrum which is shown in Figure 4-9 there are two main peaks belonging to Si (302 cm⁻¹) and CeO₂ (464 cm⁻¹)

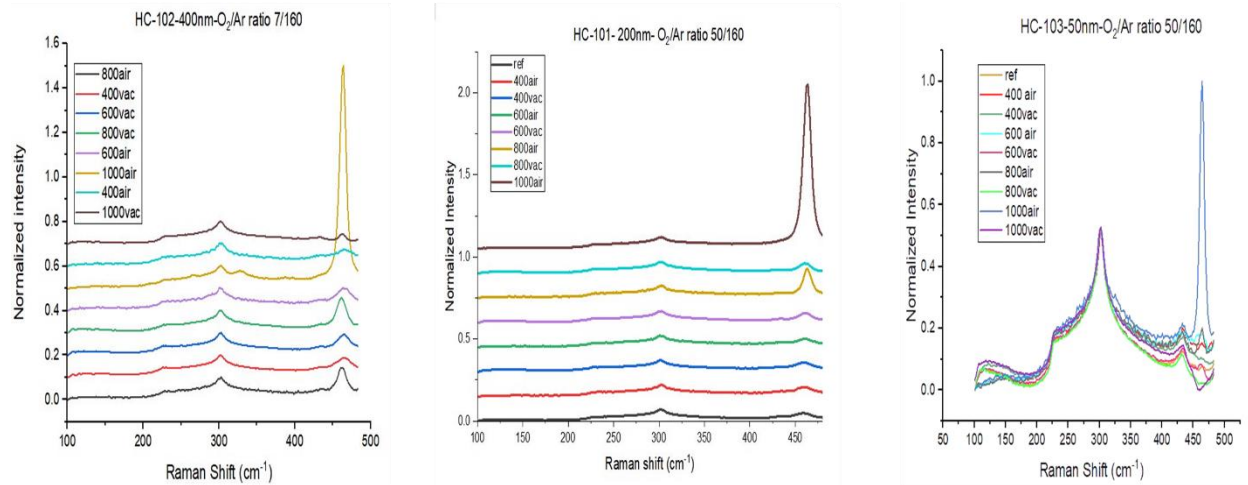


Figure 4-9: Comparison for spectra obtained for different batches coated with PDMS, with reference samples and the samples annealed in different temperatures (in lower range below 480 cm⁻¹). From left to right the Raman spectra of batch 102, 101 and 103 with 400, 200 and 50 nm thicknesses.

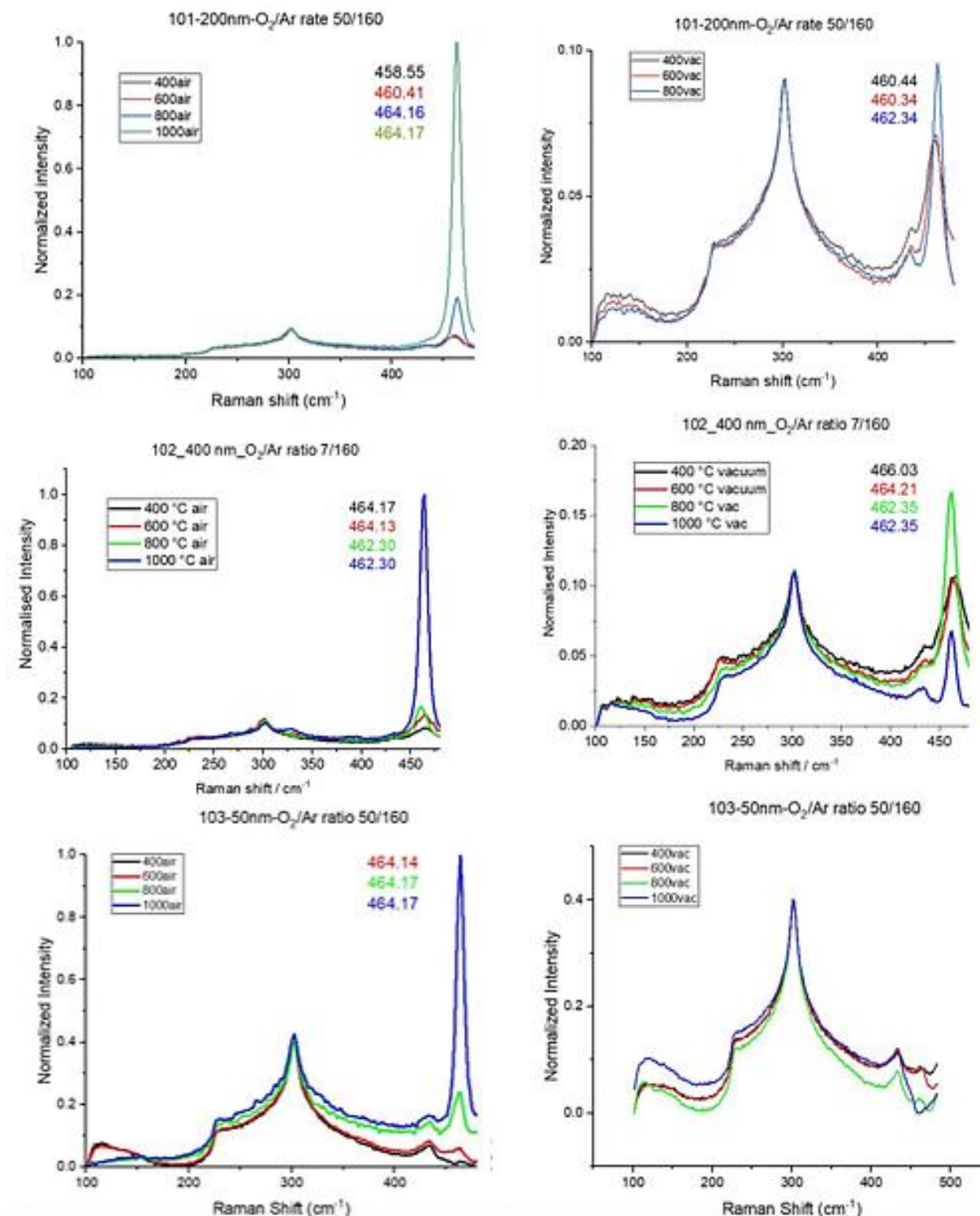


Figure 4-10: Raman spectra for 101, 102 and 103 batches (without PDMS) annealed in air (left hand side) and vacuum (right hand side). The peak shifts identified on each graph.

The peaks in the lower range of Raman spectra are normalized to the Si Peak in 302 cm⁻¹ to eliminate the experimental errors. The plot in Figure 4-10, indicates a shift in the ceria peak located

in 464 cm^{-1} both for the samples which annealed in air and vacuum. The reason for these peak shifts can be related both to the production of Ce_2O_3 and oxygen vacancies and also applied strains in the crystal structure because of CeO_2 crystal growth.

When annealing the samples in vacuum because of leaving oxygen from the vacuum chamber ($p < 3.5\text{ Pa}$), more oxygen vacancies will be produced and the amount of Ce_2O_3 in the structure of the nano film will be increased, which because of the larger lattice parameter and weaker bond in Ce_2O_3 it leads to decreasing the vibration frequency and making a red shift in Raman peak [72].

During annealing in air because of presence of a great amount of oxygen, increased reactions with CeO_2 particles in high temperature causes to growth of CeO_2 crystals which leads to produce some strains in the system, however by annealing in air the oxygen vacancies decrease which cause a blue shift in the Raman spectra [72].

Composition of Ceria is best described as CeO_{2-x} . This means that the oxide layer is a combination of CeO_2 and Ce_2O_3 . There are oxygen vacancies in the structure as well to compensate for the electrical neutrality of the film. That are expected to have Raman features at 550 cm^{-1} and 590 cm^{-1} [73] [70]. Oxygen can diffuse into and out of the layer by hopping through these vacancies. When CeO_2 is heated either in air or vacuum, diffusion of oxygen ions through microstructure is accelerated as diffusion is a temperature-controlled process. However, the direction of diffusion will be different when annealing in air or vacuum. In air, the atmosphere has a higher concentration of oxygen than the CeO_2 layer and there will be a net flux of oxygen absorbed in the layer. These oxygen ions will combine with oxygen vacancies in the structure and change the Ce^{3+} to Ce^{4+} to compensate for their extra charge. This process is reducing concentration of vacancies. Ce^{3+} has a larger radius than Ce^{4+} (because it has lost one electron less) and having more Ce^{3+} in the structure produces a strain. Also, the bound between Ce^{4+} and oxygen is shorter compared to the bound between Ce^{3+} and oxygen and the vibration frequency will be different. When ceria is heated in air, oxygen gets in and there will be less Ce^{3+} and less strain. When it is heated in vacuum, oxygen gets out, concentration of vacancies increases, and there will be more strain in structure [63]. The full width half maximum of the Raman peak of ceria at 464 cm^{-1} have been measured. As it is shown in Figure 4-11, FWHM of Raman F_{2g} signal dependent on the inverse crystal size for ceria samples (101 and 102 batches with 200 and 400 nm respectively) annealed in air and vacuum. Increasing the annealing temperature, the particle sizes increased as it is calculated based on XRD patterns and is summarized in Table 4-6, then the FWHM of ceria Raman peak decreases as the consequence of increasing particle sizes [70].

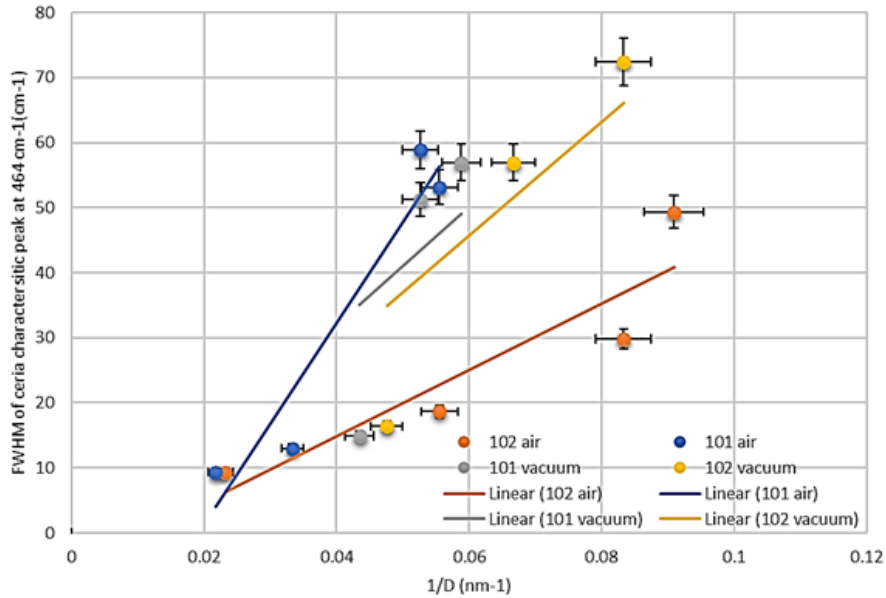


Figure 4-11: FWHM of Raman peak vs. inverse crystalline size which have been calculated by XRD data (have been done in IFE) for batches 101 and 102 (200 and 400 nm thickness respectively) annealed in air and vacuum. FWHM decreases by increasing particle sizes which is the consequence of increasing annealing temperature. Depicted trendlines are least square fits.

4.4. Polarized Raman Spectroscopy (PRS)

The experimental results which came from the Raman spectra after each definite rotation (10° or 45°) compared with simulations of three low index plane of CeO_2 crystal ((100), (110), (111)) are shown in the Figures below. These measurements were done with the purpose of figuring out the orientation of CeO_2 crystal. PRS is a useful analytical tool which can be used to identify crystal structure, differentiate between single crystals and polycrystalline materials, and determine orientation of the crystal and degree of disorder. This is especially true for single crystals.

The results of measurements which obtained both for the samples annealed in air and in vacuum shows that the silicon peak (F_{2g}) at 521cm^{-1} (filled dots) fits with the simulation results of orientation in (100) plane and as we are aware of the Si single crystal orientation (100) which is used as a substrate for growth of CeO_2 crystals, this serves to confirm that our method is reliable to identify the orientation of the single crystals. . The samples after annealing follow the pattern better than the sample before annealing (reference sample) which can shows the efficiency of the annealing in ordering the single

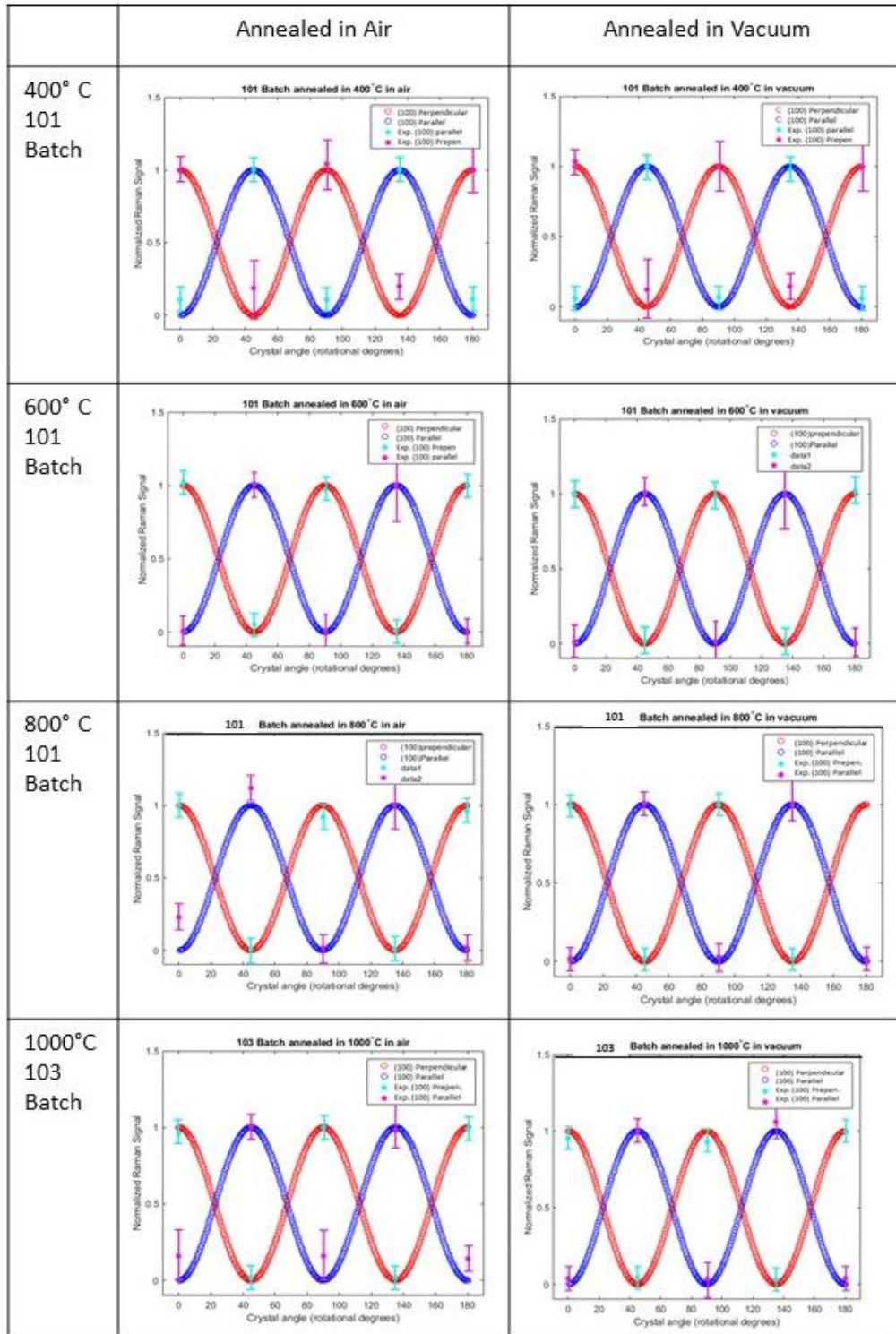


Figure 4-12: Calculated curves (empty circles) and experimental results (filled circles) of intensity variation for the Si peak (F_{2g}) (521cm^{-1}) vs. crystal rotation at parallel (blue) and perpendicular (red) polarizations. They all are in good agreement with the simulated pattern for orientation in (100) plane. Left hand side Figures are the samples annealed in air and the right side are the samples annealed in vacuum respectively. The test samples are arranged according to the annealing temperature from top to down. The experimental results fit well with the simulations.

crystals orientation. This was repeated for all the samples which were annealed in different temperatures and for the reference sample as well. Figure 4-12 illustrates the simulation performed using MATLAB. The experimental results from Si Peak at 520 cm^{-1} in different rotational angles fitted well on the calculation results of the Si (100) plane which confirms the capacity of this method in finding the orientation of single crystals. In Figure 4-13 the experimental results have been drawn over the calculation result for (111) plane which seems to be a better match compared to (100) and (110) planes. It can be said that misfits with the calculation patterns in most of the test samples is because of the polycrystallinity of CeO_2 film on Si substrate. This deduction is in agreement with the observations of SEM images. The right and left drawings belong to samples annealed in vacuum and air in respectively. Contrary to the Si crystals, patterns acquired for ceria don't follow the definite patterns that is simulated for (100) but are closer to (111) plane. The calculation patterns including the experimental data for Reference sample have been shown in Figure 4-14.

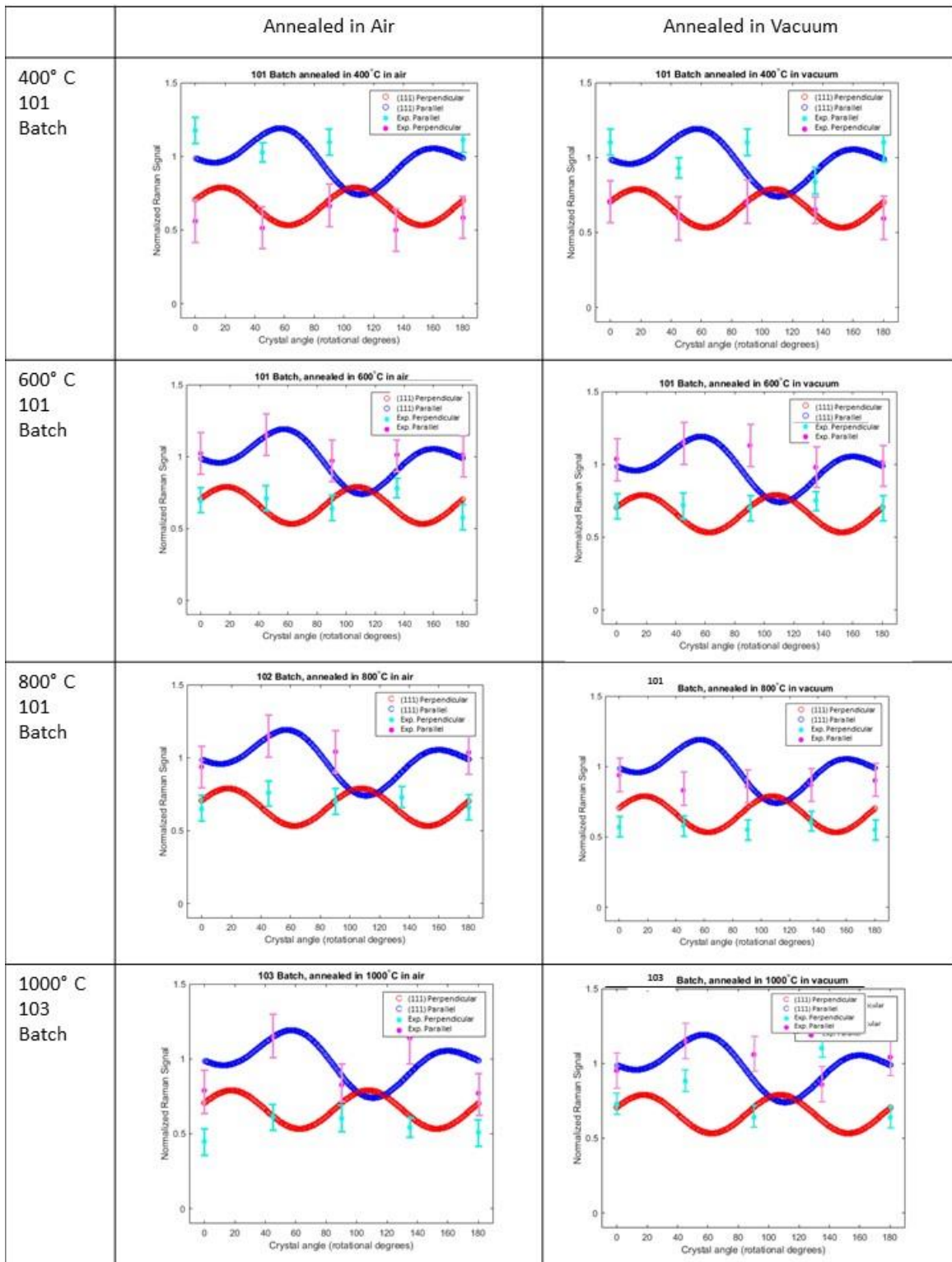


Figure 4-13: Calculated curves (empty circles) and experimental results (filled circles) of intensity variation for the CeO_2 peak (F_{2g}) intensity (464cm^{-1}) vs. crystal rotation for parallel (blue) and perpendicular (red) polarization. Left hand side Figures are the samples annealed in air and the right side are the samples annealed in vacuum respectively.

The misfit of experimental results with calculations shows polycrystallinity of CeO_2 layer.

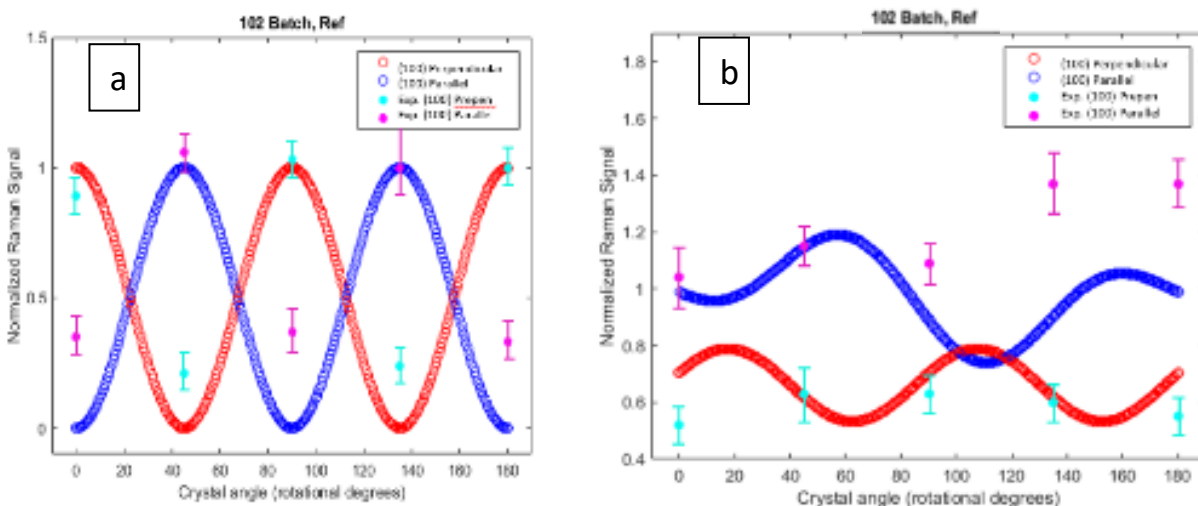


Figure 4-14: Calculated curves (empty circles) and experimental results (filled circles) for reference sample. a) calculation results for (100) plane and Raman peak of Si (F_{2g}) intensity at 521cm^{-1} by the perpendicular and parallel polarization of light in Raman set up. b) the experimental results of CeO_2 peak (F_{2g}) (464 cm^{-1}) of reference sample vs. crystal rotational angle. Experimental data (filled circles) fit better with the calculations (empty circles) for silicon on (100) plane but for CeO_2 the best fit is on (111) plane (The rest of unfitted results has not provided in the figures).

4.5. WCA

The water contact angle measurements have been examined to test the difference between the samples coated with PDMS and uncoated ones. For these measurements distilled water have been used to avoid producing contamination. The surface was not cleaned before water deposition. The samples were placed on a flat table and a high-resolution camera was in front of the samples. One drop of distilled water has been placed on all the samples and the picture was taken. WCA was measured by using IC measure software package which provides powerful tools for the manual measurement of circles, lines, and angles.

Table 4-2: WCA measurements for the CeO_2 -PDMS samples annealed in air

		400 °C	600 °C	800 °C	1000 °C
101	PDMS	115	54.14	126.57	93.18
	NO PDMS	94	87.80	130.54	118.30
102	PDMS	113	117.10	125.23	106.41
	NO PDMS	101	126.71	130.91	123.17
103	PDMS	91	104.53	129.70	120.70
	NO PDMS	89	116.6	130.24	100.63

Table 4-3: WCA measurements for the CeO₂-PDMS samples annealed in vacuum

101		400 °C	600 °C	800 °C	1000 °C
	PDMS	63.43	113.84	104.90	
	NO PDMS	88.85	132.88	136.67	
102	PDMS	94.45	115.82	118.39	125.31
	NO PDMS	108.65	128.42	135	108.43
103	PDMS		111.50	116.36	93.65
	NO PDMS		130.63	132.54	112.62

Table 4-4: WCA measurements for the CeO₂-PDMS reference samples without annealing

REF 101	PDMS	89.61
	NO PDMS	94.97
REF 102	PDMS	107.24
	NO PDMS	99.78
REF 103	PDMS	134.08
	NO PDMS	142.14

4.6. SEM

Based on the results of WCA measurements we decided to acquire SEM images of the samples which exhibited biggest differences in water contact angles (WCA) with PDMS and without that. The results obtained from SEM showed a polycrystalline structure of ceria deposited on Silicon which approves the obtained results with polarized Raman spectroscopy studies.

To summarize the results, it was decided to compare only images with same magnification. So, first, structure of reference sample with no annealing, with and without PDMS was compared.

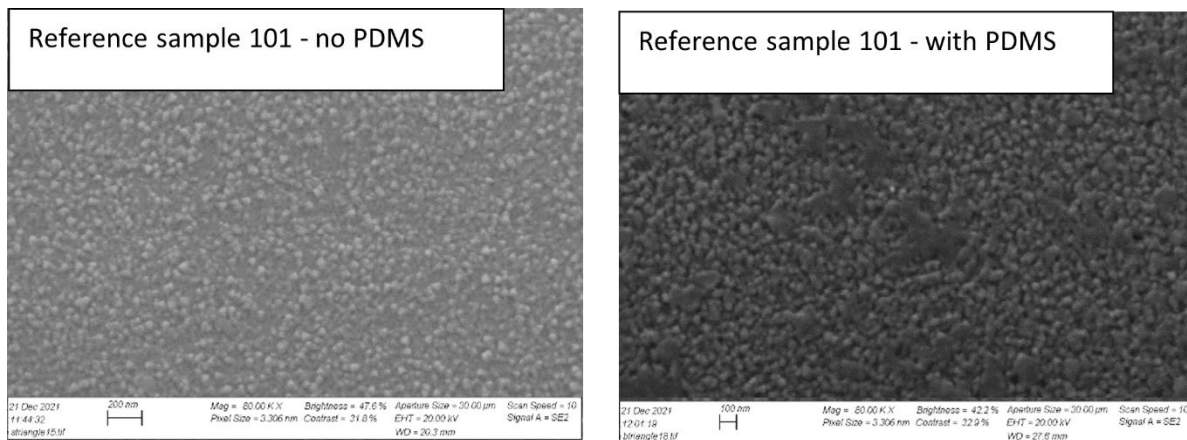


Figure 4-15: SEM images of reference samples (no annealing) with and without PDMS for the Batch 101.

Figure 4-15 displays micrographs of reference sample 101 with and without PDMS. There is no specific difference between these two samples, however, it can be said that there is some overlap of a materials similar to liquid over the ceria particles in the sample with PDMS which can be considered as dirt particles. In both pictures, ceria nanoparticles are segregated and not forming an intact continuous layer. The particles are mostly in triangular shapes however because of the small sizes the exact shapes are not distinguishable. The approximate size of particles has been measured using imageJ software for the images with better resolution and bigger particle sizes

After heat treatment (annealing), there was a change apparent in the oxide layer. In Figure 4-17, air annealed samples with and without PDMS have been compared. All the micrographs are with a magnification of 80KX. As it can be seen, the segregated ceria particles have started to cover the surface. Also, there is a relationship between annealing temperature and particle size, as the images can be compared (all at same magnification). At 400 °C the particles are small which grow bigger as temperature increases. Another interesting thing is the change in the shape of nanoparticles. Up to 600 °C, there are triangular shapes governing the surface; at 800 °C, this has been changed to spherical particles.

At 1000 °C there are a bigger size of particles which we attribute this to agglomeration of ceria particles. Agglomeration leads to potential delamination and destroying layer as continuous layer of sample annealed at 800 °C is replaced by segregated agglomerates of particles at 1000 °C. As it is shown on Figure 4-16, the measured distribution of particle sizes in Sample 103 annealed in 1000 °C, is in the range of few hundred nanometers which is different from the results from XRD patterns. In Table 4-5 the particle size for the mentioned sample is in the range of 42nm. This big difference supports the agglomeration hypothesis. Similar result is observed for the 101sample annealed at 800 °C in air. The particle size is bigger than the sizes calculated from XRD patterns, and the shape of particles is spherical which is common in agglomeration.

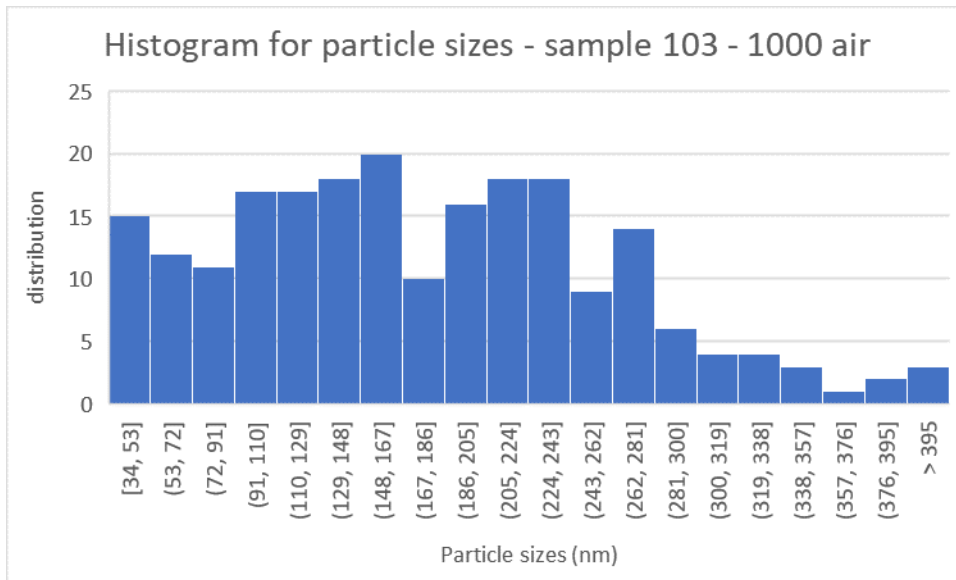


Figure 4-16: Particle size histogram measured by image j based on SEM image of sample batch 103 prepared at 1000 °C in air

The calculated particle sizes based on the SEM images have been summarized in Table 4-5 which are in good agreement with the results from Deby Sherer formula, with two exceptions mentioned where agglomeration happened.

Table 4-5: Particle size measured using image j tool based on SEM images

Samples annealed at:	800 air	800 vac	600 air	600 vac	400 air	400 vac	ref
Particle size	60nm	45nm	17nm	25nm	-	-	-

Because of small size of particles in ref sample and the sample annealed in 800 °C, the particle size measurements using this method was not achievable.

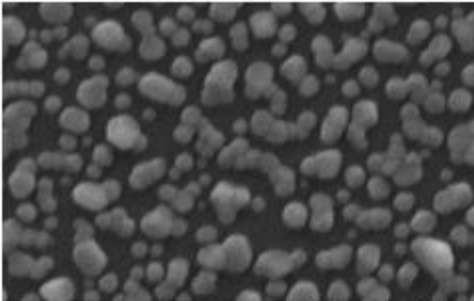
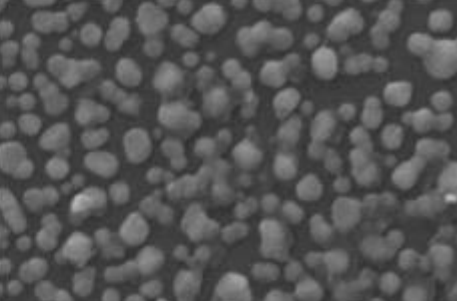
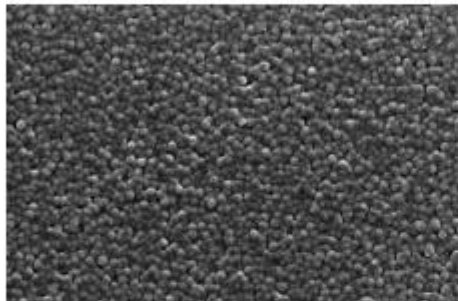
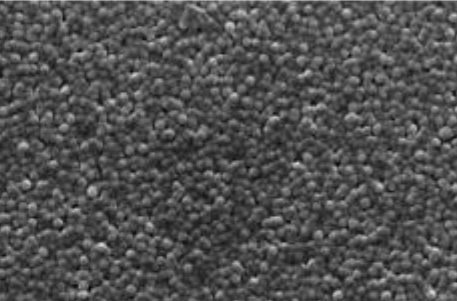
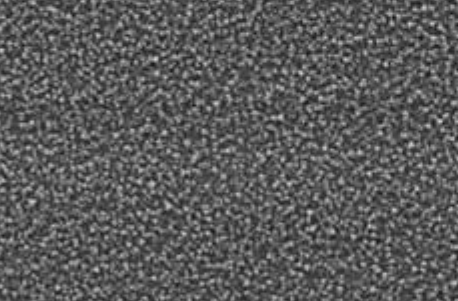
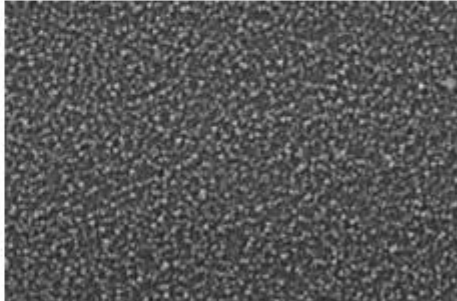
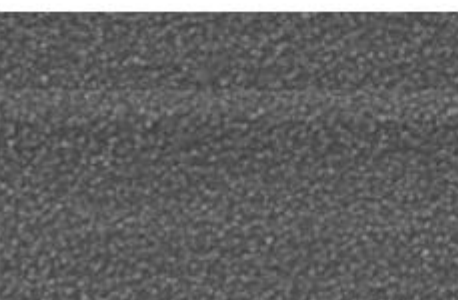
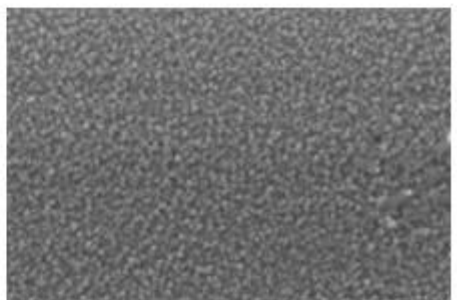
Air	No PDMS	PDMS
1000 Batch 103	 <p>10 Dec 2021 12:21:50 HV=20.00kV X500.0k 200um Mag = 50000.0x Depth = 48.2% Area/Scan = 1.20E-06 Pixel Size = 1.20E-06 Scan Area = 1.20E-06 Scan Time = 0.100s Signal = 4882</p>	 <p>10 Dec 2021 12:21:50 HV=20.00kV X500.0k 200um Mag = 50000.0x Depth = 48.2% Area/Scan = 1.20E-06 Pixel Size = 1.20E-06 Scan Area = 1.20E-06 Scan Time = 0.100s Signal = 4882</p>
800 batch 101	 <p>10 Dec 2021 12:21:50 HV=20.00kV X800.0k 200um Mag = 80000.0x Depth = 44.7% Area/Scan = 1.50E-06 Pixel Size = 1.50E-06 Scan Area = 1.50E-06 Scan Time = 0.100s Signal = 4882</p>	 <p>10 Dec 2021 12:21:50 HV=20.00kV X800.0k 200um Mag = 80000.0x Depth = 44.7% Area/Scan = 1.50E-06 Pixel Size = 1.50E-06 Scan Area = 1.50E-06 Scan Time = 0.100s Signal = 4882</p>
600 Batch 101	 <p>10 Dec 2021 12:21:50 HV=20.00kV X600.0k 200um Mag = 60000.0x Depth = 42.7% Area/Scan = 1.67E-06 Pixel Size = 1.67E-06 Scan Area = 1.67E-06 Scan Time = 0.100s Signal = 4882</p>	 <p>10 Dec 2021 12:21:50 HV=20.00kV X600.0k 200um Mag = 60000.0x Depth = 42.7% Area/Scan = 1.67E-06 Pixel Size = 1.67E-06 Scan Area = 1.67E-06 Scan Time = 0.100s Signal = 4882</p>
400 Batch 101	 <p>10 Dec 2021 12:21:50 HV=20.00kV X400.0k 200um Mag = 40000.0x Depth = 40.7% Area/Scan = 1.67E-06 Pixel Size = 1.67E-06 Scan Area = 1.67E-06 Scan Time = 0.100s Signal = 4882</p>	 <p>10 Dec 2021 12:21:50 HV=20.00kV X400.0k 200um Mag = 40000.0x Depth = 40.7% Area/Scan = 1.67E-06 Pixel Size = 1.67E-06 Scan Area = 1.67E-06 Scan Time = 0.100s Signal = 4882</p>

Figure 4-17: SEM images of air annealed samples with and without PDMS at magnification of 80KX

it appears there is a change in that temperature range responsible for this which worth further studying.

Using special high-resolution detector, we were able to acquire very good images which tell a lot about microstructure of the samples. These images are presented in Figure 4-19.

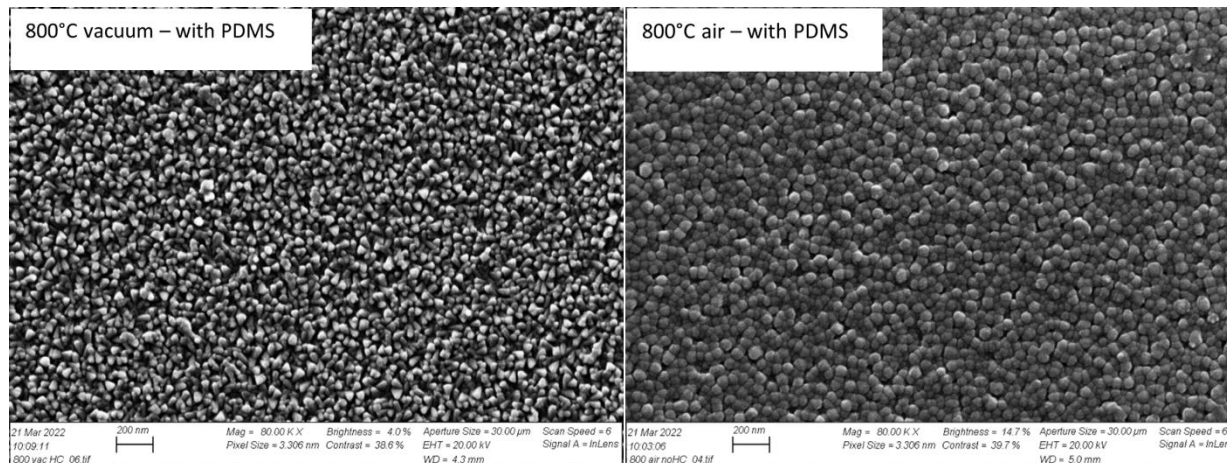


Figure 4-19: High resolution SEM images of samples annealed in air (without PDMS) and vacuum (with PDMS) at 800 °C (101 batch, the films with 200nm thickness) higher size images are presented in appendix A.

Comparing two micrographs, it can be concluded that vacuum annealed sample has a smaller particle size, and the shape of particles are trigonal. In air annealed sample, agglomeration has started, and the shapes of the particles are changing to spheres. The increase in particle sizes leads to broadening of Raman peak as it is shown in Figure 4-11. The intensity of ceria peak decreased when annealing in vacuum which can be related to decreasing Ce^{4+} to Ce^{3+} ratio.

4.7. XRD measurement

Three sets of samples have been prepared as mentioned in the methods section. These sample coded as 101 (200nm), 102 (400nm), and 103 (50nm) have been prepared using different sputtering parameters and conditions. The samples have been studied using X-ray diffraction to investigate the effect of deposition parameters on the ceria layer deposited. Figure 4-20 represents the diffraction patterns of these three reference samples.

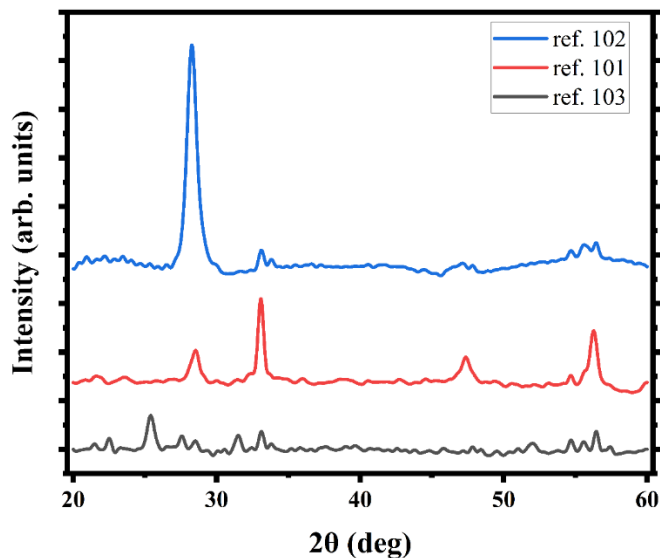


Figure 4-20: XRD patterns for reference samples, 101, 102 and 103 (no annealing is performed).

As can be seen, sample 102 has the highest intensity for the ceria representative peak at approximately 28° . This can be attributed to the deposition parameters used for this series of samples.

The next step was to study the effect of heat treatment (annealing) on the properties of deposited layers. This was carried out for three sets of reference samples in different temperatures and media as described in the methods section. The results of X-ray diffraction studies on samples 101, 102 and 103, annealed in different temperatures and in different (vacuum and air) atmospheres are presented in Figures 4-21 to 4-23.

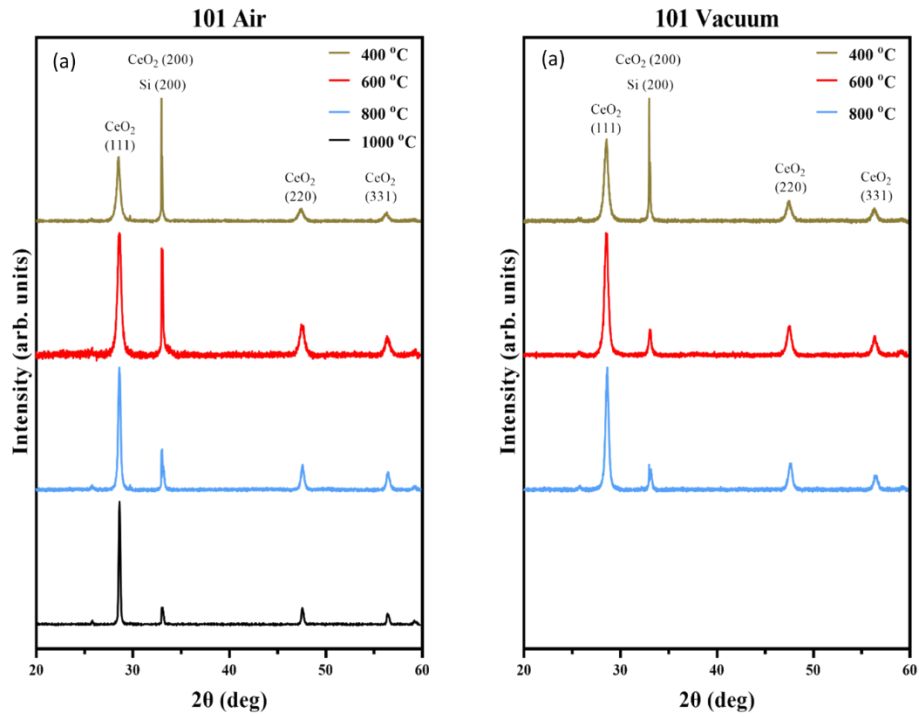


Figure 4-21: XRD patterns for batches 101 samples annealed in vacuum and air. Results for the vacuum-1000°C sample is missed because of the sample delamination (received from IFE).

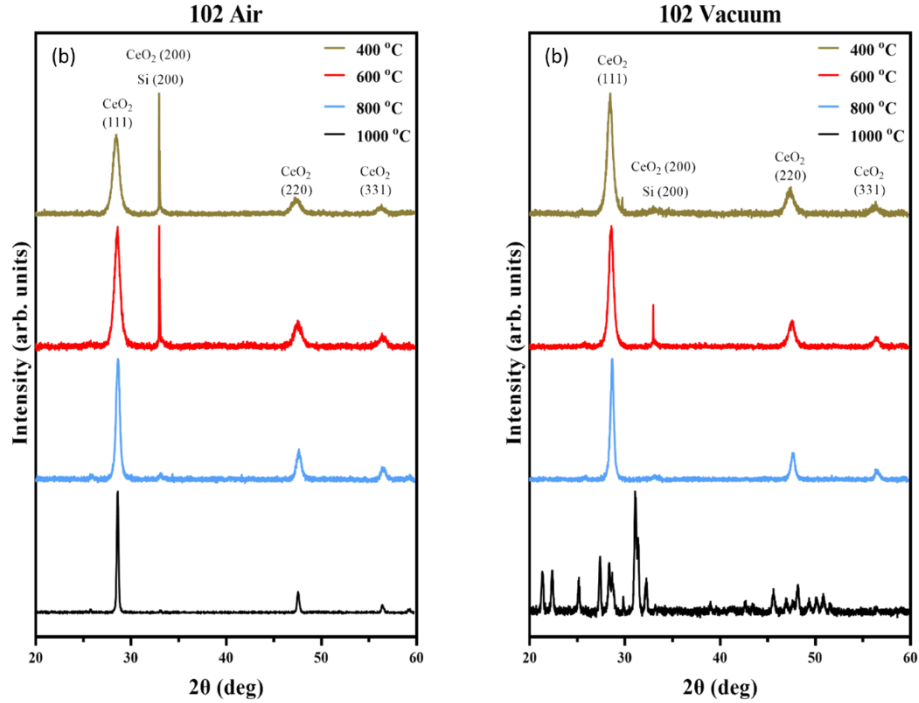


Figure 4-22: XRD patterns for batches 102 annealed in air and vacuum conditions (received from IFE).

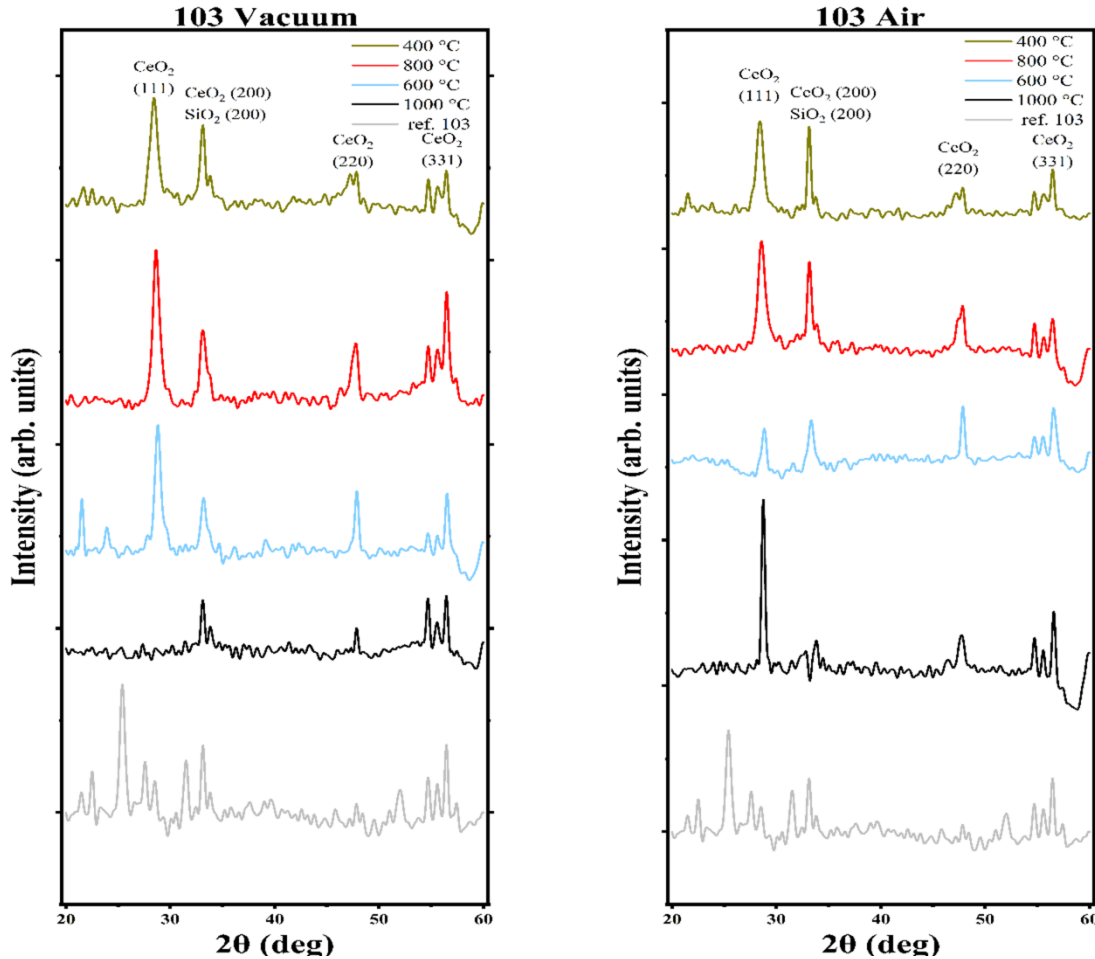


Figure 4-23: XRD patterns for batches 103 annealed in air and vacuum. (The patterns obtained at UiS)

Numbers in parentheses above the upper graph in each subplot represent crystallographic planes after indexation. Figure 4-23 represents the XRD patterns of the 103 samples which is obtained in UiS. All three sets of samples have fcc – fluorite type structure which is the crystal structure of ceria (CeO_2). XRD patterns of samples 101 and 102 were acquired at IFE.

As it can be deduced from the patterns acquired for 101 samples, for samples annealed in air, width of ceria (111) peak is decreased with increasing temperature. This is inversely proportional to the crystallite size, and it is expected to have a smaller crystal size where there is a wider peak. This can be attributed to the higher diffusion in elevated temperatures which will result in crystal growth and bigger crystallite sizes.

Same claim can be made regarding 101 samples annealed in vacuum, however annealing at 1000 °C has resulted in the surface layer of ceria to be peeled off. This can be attributed to different causes, like conversion of CeO_2 to Ce_2O_3 which will cause the oxide layer being disconnected from Silicon substrate because of crystal lattice mismatch and strains.

Samples of batch 102 annealed in air, show similar trend as 101 air annealed samples and the crystallite size is decreased by increasing temperature. The justification is same, and this is attributed to higher diffusion rates and crystal (grain) growth.

Samples annealed in vacuum show same trend although interestingly the intensity of the peaks is not reduced much with decreasing temperature. This can be a promising sample and annealing condition, if smaller size crystallites are preferred. Sample annealed at 1000 °C also kept its integrity in batch 102 which can be justified by the better adhesion of the surface layer to the substrate and possibly a mixed oxide layer with a CeO₂ layer at the interface with Silicon substrate and Ce₂O₃ layer near the outer surface at the interface with vacuum.

103 batch samples prepared in air, show similar increase of peak width with decreasing temperature as 101 and 102 air samples. Sample annealed at 800 °C show less intensity of Ceria characteristic peak and there is no apparent reason for that. Samples annealed at 600 °C and 400 °C show similar trends and it can be deduced that similar mechanisms are in operation in both temperatures. Whereas, in 800 °C there is a not yet explained change. Sample annealed at 1000 °C shows the narrow sharp peak accompanied with higher crystallinity which in this case means higher grain sizes possibly because of grain growth at higher temperatures.

Vacuum annealed 103 samples provide some insightful data. First, the highest intensity is at 600 °C and the smallest size will probably be the sample annealed at lowest temperature like other batches. However, the characteristic peak of ceria at approx. 28° is vanished in the sample annealed at 1000 °C. This is an interesting find and can be attributed to the possible conversion of CeO₂ to Ce₂O₃. This needs to be investigated further in future works as this potentially provides a route to prepare controlled CeO₂ / Ce₂O₃ concentrations in samples, useful for sensor applications among other things.

The peak at $2\theta \approx 33^\circ$ appears as combination of signals from CeO₂ (200) and Si (200) planes. The reflection from the latter is forbidden for the ideal Si-crystal and which showing up may indicate lattice distortion of the substrate [32]. The lattice parameter was found according to the Bragg's law (for the first diffraction order):

$$\lambda = d_{HKL} \sin \theta \quad (4.1)$$

where $\lambda = 1.5406 \text{ \AA}$ – wavelength for the *Cu-K α* radiation, d_{HKL} – distance between two planes *HKL*. The lattice parameter was calculated based on the position of peak (111). The crystallite size for each sample was estimated based on the Debye-Scherrer approach:

$$B = \frac{K*\lambda}{\beta*\cos\theta} \quad (4.2)$$

Where $K=0.9$ and β = FWHM of the peak. We use the FWHM for the peak at the minimum 2θ angle which is around 28°, which is (111), to minimize effect of the microstrain. Microstrain in the lattice causes broadening of the peaks which effect increases continuously over θ .

Using this method, Lattice parameter and crystallite sizes for different samples, annealed in different temperatures, in different media can be calculated using equations (1) and (2)

respectively. It shall be noted however that Debye-Scherrer formula is not a precise and reliable method, but the numbers calculated are comparable in same experimental setup. The results of calculations are presented in following tables.

Table 4-6: Summarized results on the lattice parameters of CeOx thin films (IFE and UiS)

		Lattice parameter, Å				
		25°C	400°C	600°C	800°C	1000°C
Annealing in air	Ce 101	5,409	5,432	5,417	5,405	5,409
	Ce 102	5,463	5,448	5,424	5,409	5,414
	Ce 103	5,465	5,451	5,426	5,407	5,405
Annealing in vacuum	Ce 101	5,409	5,429	5,408	5,419	-
	Ce 102	5,463	5,458	5,413	5,406	-
	Ce 103	5,465	5,488	5,504	5,554	-

Table 4-7: Summarized results on the crystalline size of CeOx thin films (IFE and UiS)

		Crystallite Size, nm				
		25°C	400°C	600°C	800°C	1000°C
Annealing in air	Ce 101	9	19	18	30	46
	Ce 102	8	11	12	18	43
	Ce 103	5	6	9	13	42
Annealing in vacuum	Ce 101	9	17	19	23	-
	Ce 102	8	12	15	21	-
	Ce 103	5	6	9	13	42

The change in lattice parameter and crystallite size with the annealing temperature is represented in Figure 4-24, 4-25, 4-26 for samples 101, 102, and 103 respectively.

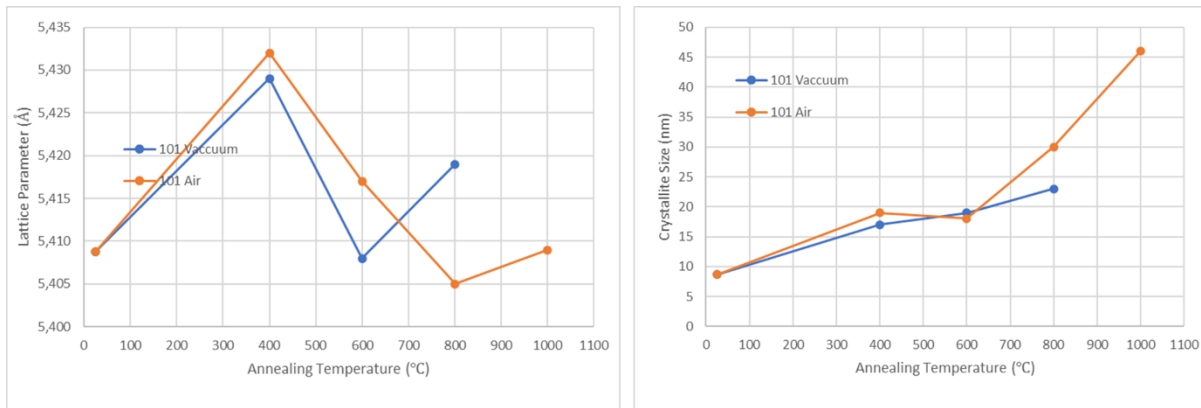


Figure 4-24: Lattice parameter and crystallite size of ceria vs. annealing temperature for 101 batch.

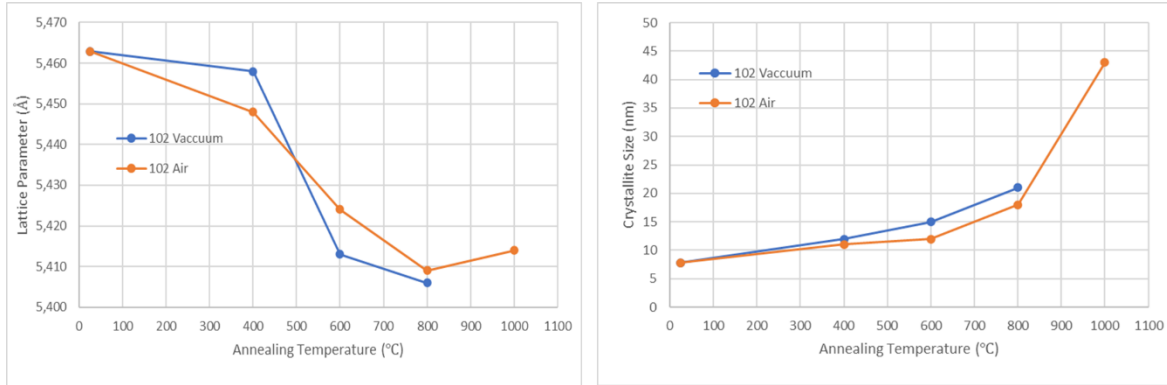


Figure 4-25: Lattice parameter and crystallite size of ceria vs. annealing temperature for 102 batch

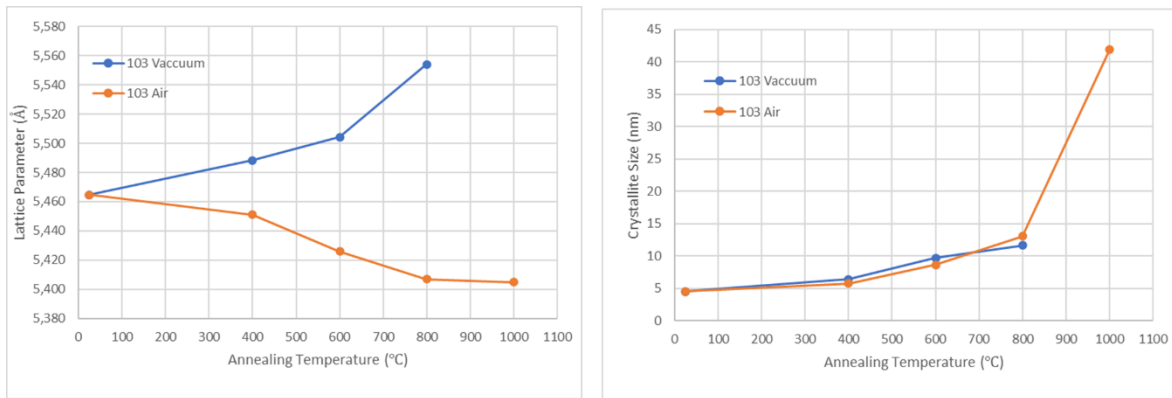


Figure 4-26: Lattice parameter and crystallite size of ceria vs. annealing temperature for 103 batch

For batch 101, annealed at air, there is a minimum in lattice parameter in 800 °C. The minimum for vacuum annealed 101 samples is also at 600 °C. This is interesting because from thermodynamics we know that with increasing temperature, there will be more movement of atoms and their average distance and hence the lattice parameter will increase. This observed decrease means the minimum interstitials in the structure and most perfect crystalline structure of Ceria. It can be said that extra oxygen ions in the structure are released at this temperature. After 800 °C, lattice parameter increases which can be attributed to the effect of temperature and increasing the vibration of atoms, and what is expected normally when heating a solid. The release of oxygen ions is easier when there is no external pressure, hence release is achieved at a lower temperature in vacuum. These deductions are not solid as the tests were conducted on only 5 temperatures. Tests shall be carried out at more temperatures and more samples be tested so that the data becomes reliable.

The crystallite size increases with increasing annealing temperature, which is expected. There is however a sharp increase after 600 °C which may be because of activation of other diffusion mechanisms at higher temperatures. Crystal growth is expected at this temperature.

Samples from batch 102, annealed in air, display same decrease in lattice parameter with increasing temperature up to 800 °C similar to 101 air annealed samples. And the conclusion is same. Vacuum annealed samples however have a different trend. There is no increase after 600°C, whereas the slope or the rate (of oxygen ion release) decreases. As told earlier when comparing reference samples, 102 seems a more robust and stronger layer than 101 and it can be assumed that oxygen release is becoming difficult as diffusion through this compact layer is much more difficult.

The crystallite size of the air annealed samples shows a sharp increase after 800 °C compared to 600 °C for samples 101. This can be attributed to the more compact layer which makes diffusion more difficult and requires higher temperatures to activate more rapid diffusion mechanisms. This increase in the slope is attributed to the governance of grain growth compared to grain nucleation. Interestingly, sizes of vacuum and air annealed samples up to this temperature are roughly similar.

In samples of 103 batch annealed in air, a continuous decrease in lattice parameter with increasing annealing temperature was observed. This has been attributed to the inward diffusion of oxygen through ceria layer and decrease in concentration of oxygen vacancies. As oxygen vacancies decrease, Ce^{3+} ions in the structure undergo the redox reaction and oxidize to Ce^{4+} . This is accompanied with a reduction in the radius of the Cerium ion off course which in turn leads to reduction of the Ce-O bond length, or average distance, decreasing lattice parameter.

Vacuum annealed 103 samples show a different trend. Lattice parameter increases steadily with increasing annealing temperature, with a sharp increase at 600 to 800 °C. This is however in line with the expectations as higher temperature promotes outward diffusion of oxygen into vacuum. This is accompanied with an increase in oxygen vacancy concentration and Ce^{3+}/Ce^{4+} increase. As explained, Ce^{3+} has a higher radius than Ce^{4+} , which leads to higher bond length and bigger lattice parameter [72]. It is suggested that the sharp increase in the 800 °C because of activation of more diffusion routes.

In 103 samples, increase in crystallite size with temperature, follows the same pattern of 102. The rate of increase after 800 °C which is the point where slope or governing mechanism changes is higher for 103, meaning that diffusion is easier in 103 compared to 102. This can be attributed to 102 sample being more compact and diffusion in that samples being more difficult. Crystallite sizes for vacuum annealed samples are almost same as air annealed samples up to this turning point and follow a straight line suggesting a diffusion-controlled mechanism.

By increasing the temperature, the FWHM of Raman spectra decreases as a consequence of increasing the particle sizes which is shown in Figure 3-25 or decreasing the induced defects and strains. The calculated particle sizes using XRD pattern are in the same range as the obtained particle sizes using SEM. However, the obvious difference in samples annealed at 1000°C and 800°C can be related to agglomeration. The results from different characterization techniques are in good agreement with each other.

Chapter 5

Conclusion

In this thesis work, the goal was to investigate Cerium Oxide thin films. Thin films have been prepared using magnetron sputtering on two substrates, Silicon and glass. Samples were prepared in Institut for Energi Teknik (IFE) at Oslo. Samples coated on glass were prepared to study the effect of changing coating parameters of magnetron sputtering and to see if there is a quantum effect in small sizes. In these series of tests, after getting the Raman spectrum for each sample, it was concluded that modifying parameters like film thickness, deposition rate, oxygen to argon ratio, and pressure will result in Raman peak position change or its broadening.

These tests were repeated a few times for each sample to study the repeatability of the tests and prevent errors as much as possible.

However, modified parameter were not comparable after categorization of samples, because more than one parameter was changed between samples. This presented a difficulty in analyzing the results and making conclusions. Although, it can be said that with increasing deposition pressure, FWHM decreased and there was a shift in Raman peak. This finding is in accordance with previously reported results elsewhere.

With reduction in film thickness, a blue shift in Raman peak was expected. This did not happen and in some of the samples, there was a blue shift and in some a red shift and some samples didn't show any shifts at all. No meaningful relation between film thickness and Raman peak shift cannot be reported.

Samples coated over Silicon, were heat treated after deposition and then put in an oven for 17 hours near PDMS so that a surface film of PDMS is deposited on them and potentially increase hydrophobicity. These samples were studied using Raman spectroscopy afterwards to see if PDMS can be identified on the surface. However, there was no success in identification of PDMS on sample surfaces. Two theories were suggested to explain this, first is that PDMS layer is not thick enough to be identifiable by Raman studies. The other suggested reason was that if PDMS has

remained on the surface of the layer in the timeframe from application to the test time. To check these hypotheses, one drop of a silicone oil (similar to PDMS) were put on the surface and the Raman spectra was acquired with the oil drop on the surface and also after removing of the oil.

The peaks with silicone oil were vanished after the oil layer was cleaned with a tissue. So, it was concluded that if there was silicone layer on the surface, there could have been an effect in Raman spectra and the prepared samples had their layer removed due to the time between sample preparation and testing. These studies need to be conducted again to check repeatability. More specifically, oven treatment with PDMS oil can be retried and the freshly prepared samples to be see if there is an oil layer on the surface.

Effect of heat treatment (or annealing) on the properties of thin films was also studied. In the studies, it was observed that increasing annealing temperature of the samples, reduces the FWHM of the peaks. This can be attributed to the increase in crystallinity and crystal size.

All of the samples annealed in air and also in vacuum displayed a red shift in peaks. For air annealed samples this can be explained by the increase in strain at the interface of Ceria and substrate. For vacuum annealed samples, annealing will be accompanied by release of oxygen from structure and conversion of CeO_2 to Ce_2O_3 . Ce^{3+} has a larger radius and band length of Ce-O will be larger which results in a red shift.

Water Contact Angle (WCA) was another test conducted on the samples. This test was suggested to check existence of PDMS on sample surface. After testing (putting water droplets on sample surfaces and measuring contact angle on the photos taken), the results indicated that there are meaningful differences between samples. It was proposed that the reason is because of the surface morphology of the samples. To understand the root for this difference in behavior, a series of SEM studies on sample surfaces were conducted.

SEM studies started with the idea of recognizing differences between surfaces containing PDMS and without that. However, other results also obtained including the effect of increasing annealing temperature in increasing particle (grain) sizes. Increasing annealing temperature resulted in increasing particle sizes. In- samples annealed at 1000°C , agglomeration of particles was evident. Increasing annealing temperature also accompanied with an increase in ordering of the layer.

Records of previous works in IFE, and the WCA measurements conducted at UiS, showed meaningful differences between surfaces coated with PDMS and bare CeO₂ surfaces. Previous works carried out elsewhere suggested that WCA is dependent to crystal orientation and a hypothesis was proposed about effect of orientation of surface ceria layer on WCA and to study if there is a preferential orientation in ceria layer. To study this, PR has been used.

In the first step, simulation of possible, expected patterns were carried out using MATLAB. The simulation was conducted for three lowest index planes of FCC structure: (100), (110), (111). Polarized Raman studies were carried out using a makeshift setup to measure the angle of the sample towards the beam. Details of the setup explained elsewhere in this document. Acquired data from the tests were fitted against simulated patterns and for the samples coated on Si substrate, the measured and simulated data complied. Si substrate was a single crystal with a (001) plane and the data acquired for Si peak was a very good fit with the simulated model. However, for ceria there was no such agreement for ceria with simulated peak and it was concluded that the ceria layer is polycrystalline with a preference in (111).

The last part of the research was XRD studies to complement the data from IFE, which lacked a few samples. Using XRD patterns, existence of ceria layer, was confirmed and lattice parameter was calculated and using Debye-Scherrer formula, size of crystallites estimated. The results generally complied with previous results from SEM and Raman studies.

References

- [1] I. Porqueras, C. Person, C. Corbella, M. Vives, A. Pinyol and E. Bertran, "Characteristics of e-beam deposited electrochromic CeO₂ thin films," *Solid State Ion.* 165 131-137, pp. 131-137, 2003.
- [2] S. Debnath, M. R. Islam and M. S. R. Khan, "Optical properties of CeO₂ thin films," *Bulletin of Materials Science*, p. 315–319, 2007.
- [3] A. Paulenova, S. Creager and J. D. Navratil, "Redox potentials and kinetics of the Ce³⁺/Ce⁴⁺ redox reaction and solubility of cerium sulfates in sulfuric acid solutions," *Journal of Power Sources*, pp. 431-438, 2002.
- [4] B. A. M. R. M. M. C. B. A. & K. A. Elidrissi, "Structural and optical properties of CeO₂ thin films prepared by spray pyrolysis," *Thin Solid Films*, p. 23–27, 2000.
- [5] S. W. W. Z. J. & Q. Y. Wang, "Study of the Raman spectrum of CeO₂ nanometer thin films," *Materials Chemistry and Physics*, p. 246–248, 2001.
- [6] I. S. T. A. H. U. & C. P. Kosacki, "Raman scattering and lattice defects in nanocrystalline CeO₂ thin films," *Solid State Ionics*, p. 99–105, 2002.
- [7] S. D.-M. Z. K. A. L. N. K. V. & P. Z. V. Aškračić, "Oxygen vacancy-induced microstructural changes of annealed CeO_{2-x} nanocrystals," *Journal of Raman Spectroscopy*, p. 76–81, 2011.
- [8] B. C. G. G. M. & K. U. Hirschauer, "Studies of highly oriented CeO₂ films grown on Si(111) by pulsed laser deposition," *Thin Solid Films*, pp. 3-7, 1999.
- [9] M. W. T. T. T. S. Y. M. T. S. Y. M. Mashimo, "Cerium oxide (CeO_{2-x}) nanoparticles with high Ce³⁺ proportion synthesized by pulsed plasma in liquid," *Ceramics International*, pp. 26502-26510, 2020.
- [10] J. E. R. R. D. Z. F. C. S.-W. & H. I. P. Spanier, "Size-dependent properties of CeO_{2-y} nanoparticles as studied by Raman scattering," *Physical Review B*, pp. 245407 1-8, 2001.
- [11] T. R. A. Y. B. S. M. K. A. E. A. S. A. A. K. K. Plakhova, "Towards the surface hydroxyl species in CeO₂ nanoparticles," *Nanoscale*, pp. 18142-18149, 2019.
- [12] S. M. S. & S. A. K. Kanakaraju, "Optical and structural properties of reactive ion beam sputter deposited CeO₂ films," *Thin Solid Films*, p. 191–195, 1997.
- [13] Y. T. T. B. J. B. A. G. R. C. E. F. J. B. B. Guhel, "Rapid thermal annealing of cerium dioxide thin films sputtered onto silicon (111) substrates: Influence of heating rate on microstructure and electrical properties," *Materials Science in Semiconductor Processing*, p. 352–360, 2015.
- [14] Z. Shi, P. Shum, Z. Zhou and L. Li, "Effect of bias voltage on the properties of CeO_{2-x} coatings prepared by magnetron sputtering," *Surface and Coatings Technology*, p. 411–416, 2017.

- [15] R. V. G. M. T. H. Y. & R. G. Murugan, "Effect of rf power on the properties of magnetron sputtered CeO₂ thin films," *Journal of Materials Science: Materials in Electronics*, p. 2800–2809, 2015.
- [16] M. T. Ta, D. Briand, Y. Guhel, J. Bernard, J. C. Pesant and B. Boudart, "Growth and structural characterization of cerium oxide thin films realized on Si(111) substrates by on-axis rf. magnetron sputtering," *Thin Solid Films*, p. 450–452, 2008.
- [17] H. A. J. Z.-T. A. M. V. J.-P. Z. Z. R. M. M. D. B. Z. Miran, "Influence of DC magnetron sputtering reaction gas on structural and optical characteristics of Ce-oxide thin films," *Ceramics International*, pp. 16450-16458, 2018.
- [18] F. P. G. M. Kaspar J, "Use of CeO₂-based oxides in the three-way catalysis," *Catalysis Today*, pp. 285-298, 1999.
- [19] S. T. A. H. Jasinski P, "Nanocrystalline undoped ceria oxygen sensor," *Sensors and Actuators B: Chemical*, pp. 73-77, 2003.
- [20] V. J. G. R. Park SD, "Direct oxidation of hydrocarbons in a solid oxide fuel cells," *Nature*, pp. 265-267, 2000.
- [21] H. R. R. J. Sun CW, "Cathode materials for solid oxide fuel cells: a review," *Journal of Solid State Electrochemistry*, pp. 1125-1144, 2010.
- [22] S. D. W. Z. P. M. S. B. S. A. S. T. Y. Y. D. Y. W. X. H. Y. Feng XD, "Converting ceria polyhedral nanoparticles into single-crystal nanospheres," *Science*, p. 1504–1508, 2006.
- [23] N. Ozer, "Optical properties and electrochromic characterization of sol–gel deposited ceria films," *Solar Energy Materials and Solar Cells*, p. 391–400, 2001.
- [24] K. R. Singh, V. Nayak, T. Sarkar and R. P. Singh, "Cerium oxide nanoparticles: properties, biosynthesis and biomedical application," *Royal Society of Chemistry Advancements*, p. 27194–27214, 2020.
- [25] L. Sun, W. Xiao, X. Hao, Q. Meng and M. Zhou, "A first-principles study on the structural, thermal and electronic properties of cerium oxides by using different functionals," *Electronic Structure*, 2018.
- [26] H. L. Tuller and A. S. Nowick, "Small polaron electron-transport in reduced CeO₂ single-crystals," *Journal of Physics and Chemistry of Solids*, p. 859–867, 1977.
- [27] S. P. S. K. S. V. & S. S. Deshpande, "Size dependency variation in lattice parameter and valency states in nanocrystalline cerium oxide," *Applied Physics Letters*, pp. 133113-133120, 2005.
- [28] M. S. W. G. Sayle DC, "Atomistic models for CeO₂(111), (110), and (100) nanoparticles, supported on yttrium-stabilized zirconia," *Journal of American Chemical Society*, p. 11429–11439, 2002.
- [29] A. J. v. S. M. Jiang Y, "Density-functional calculation of CeO₂ surfaces and prediction of effects of oxygen partial pressure and temperature on stabilities," *Journal of Chemical Physics*, pp. 064701-064705, 2005.

- [30] C. M. B. U. P. S. H. S. M. G. M. M. R. D. S. S. S. D. Sayle TXT, "Strain and architecture-tuned reactivity in ceria nanostructures; enhanced catalytic oxidation of CO to CO₂," *Chemistry of Materials*, p. 1811–1821, 2012.
- [31] P. C. Campbell CT, "Oxygen vacancies and catalysis on ceria surfaces. *Science*. 2005; 309: 713–," *Science*, p. 713–720, 2005.
- [32] X.-D. H. W. Zhou, "Size-induced lattice relaxation in CeO₂ nanoparticles.," *Applied Physics Letters*, p. 3512–3514, 2001.
- [33] F. X. Wang ZL, "Polyhedral shapes of CeO₂ nanoparticles," *Journal of Physical Chemistry B*, p. 13563–13566, 2003.
- [34] C. P. C. A. N. J. P. V. Carretin S, "Nanocrystalline CeO₂ increases the activity of Au for CO oxidation by two orders of magnitude," *Angewandte Chemie International Edition*, p. 2538–2540, 2004.
- [35] D. A. L. J. A. T. R. K. J. Hailstone RK, "A study of lattice expansion in CeO₂ nanoparticles by transmission electron microscopy," *Journal of Physical Chemistry C*, p. 15155–15159, 2009.
- [36] M. a. A. D. Daniel, "Gold Nanoparticles: Assembly, Supramolecular Chemistry, Quantum-Size-Related Properties, and Applications toward Biology, Catalysis, and Nanotechnology," *Chemical Reviews*, pp. 293-346, 2004.
- [37] G. Faraci, S. Gibilisco, A. R. Pennisi and C. Faraci, "Quantum size effects in Raman spectra of Si nanocrystals," *Journal of Applied Physics*, 2011.
- [38] W. Pengren, P. Chaoyi, W. Binrui, Y. Zhiqing, Y. Fubiao and Z. Jiangcheng, "A facile method of fabricating mechanical durable anti-icing coatings based on CeO₂ microparticles," *IOP Conference Series Materials Science and Engineering*, pp. 1-7, 2015.
- [39] L. Huang, W. Zhang, K. Chen, W. Zhu, X. Liu, R. Wang, X. Zhang, N. Hu and Y. Suo, "Facetselective response of trigger molecule to CeO₂ {110} for up-regulating oxidase-like activity," *Chemical Engineering Journal*, p. 746–752, 2017.
- [40] J. Tam, U. Erb and G. Azimi, "Non-wetting nickel-cerium oxide composite coatings with remarkable wear stability," *MRS Advances*, p. 1647–1651, 2018.
- [41] J. Tam, B. Feng, Y. Ikuhara, H. Ohta and U. Erb, "Crystallographic orientation – surface energy – wetting property relationships of rare earth oxides," *Journal of Materials Chemistry A*, pp. 18384-18388, 2018.
- [42] Trovarelli A., "Catalytic properties of ceria and CeO₂-containing materials," *Catalysis Reviews*, p. 439–520, 1996.
- [43] Z. Shi, Z. Zhifeng, P. Shum and L. K.-Y. Li, "Thermal stability, wettability and corrosion resistance of sputtered ceria films on 316 stainless steel," *Applied Surface Science*, pp. 166-171, 2019.

- [44] "Polydimethylsiloxane - Wikipedia," [Online]. Available: <https://en.wikipedia.org/wiki/Polydimethylsiloxane>. [Accessed 22 May 2022].
- [45] "Polydimethylsiloxane - American Chemical Society," [Online]. Available: <https://www.acs.org/content/acs/en/molecule-of-the-week/archive/p/polydimethylsiloxane.html>. [Accessed 22 May 2022].
- [46] A. Mata, A. J. Fleischman and S. Roy, "Characterization of polydimethylsiloxane (PDMS) properties for biomedical micro/nanosystems," *Biomedical Microdevices*, p. 281–293, 2005.
- [47] E. J. Park, Y. K. Cho, D. H. Kim, M. G. Jeong, Y. H. Kim and Y. D. KiM, "Hydrophobic Polydimethylsiloxane (PDMS) Coating of Mesoporous Silica and Its Use as a Preconcentrating Agent of Gas Analytes," *Langmuir*, p. 10256–10262, 2014.
- [48] L. Jayes, A. P. Hard, C. Séné, S. F. Parker and U. A. Jayasooriya, "Vibrational Spectroscopic Analysis of Silicones: A Fourier Transform-Raman and Inelastic Neutron Scattering Investigation," *Analytical Chemistry*, p. 742–746, 2003.
- [49] Y. C. A. S. I. Cho, "Fabricating a Raman spectrometer using an optical pickup unit and pulsed power," *Scientific Reports*, 2020.
- [50] K. Nakamoto, in *Infrared and Raman Spectra of Inorganic and Coordination Compounds*, John Wiley & Sons, 2008, p. 1–147.
- [51] D. I. Bower, "Investigation of molecular orientation distributions by polarized Raman scattering and polarized fluorescence," *Journal of Polymer Science Part A-2: Polymer Physics*, p. 2135–2153, 1972.
- [52] "Technical Note: Polarised Raman Spectroscopy," Edinburgh Instruments, [Online]. Available: <https://www.edinst.com/us/polarised-raman-spectroscopy/>. [Accessed 22 May 2022].
- [53] D. Tuschel, "Practical Group Theory and Raman Spectroscopy, Part II: Application of Polarization," *Spectroscopy*, pp. 15-22, 2014.
- [54] N. D. E. M. J. R. R. N. W. M. S. J. H. J. J. D. C. Goldstein J. I., *Scanning Electron Microscopy and X-Ray Microanalysis*, New York: Springer, 2018.
- [55] "Principles and applications of EPMA and SEM," [Online]. Available: <https://emil.sites.unlv.edu/the-applications-of-epma-and-sem/>. [Accessed 22 May 2022].
- [56] A. U. Hamid, *A Beginner's Guide to Scanning Electron Microscopy*, Springer, 2018.
- [57] H. Y. F. Y. C. H. Liang J., "Formation of superhydrophobic cerium oxide surfaces on aluminum substrate and its corrosion resistance properties," *Surface and Interface Analysis*, pp. 1211-1216, 2013.
- [58] S. S. R. Cullity B. D., *Elements of X-Ray Diffraction*, Pearson New International Edition, International Edition: Pearson, 2014.

- [59] C. Kittel, Introduction to solid state physics, New York: John Wiley & Sons, 1953.
- [60] "Space Group Diagrams and Tables," [Online]. Available: <http://img.chem.ucl.ac.uk/sgp/large/sgp.htm>. [Accessed 22 May 2022].
- [61] "Atomic Form Factors," TU Graz, [Online]. Available: <http://lampx.tugraz.at/~hadley/ss1/crystalldiffraction/atomicformfactors/formfactors.php>. [Accessed 22 May 2022].
- [62] M. E. S. K. Waseda Y., X-Ray Diffraction Crystallography, Springer, 2011.
- [63] S. Loridant, "Raman spectroscopy as a powerful tool to characterize ceria-based catalysts," *Catalysis Today*, pp. 98-111, 2021.
- [64] S. Mochizuki, "Infrared Optical Properties of Cerium Dioxide," *Physica Status Solidi*, pp. 189-199, 1982.
- [65] T. Shimanouchi, M. Tsuboi and T. Miyazawa, "Optically Active Lattice Vibrations as Treated by the GF-Matrix Method," *Journal of Chemical Physics*, pp. 1597-1612, 1961.
- [66] W. Weber, K. Hass and J. McBride, "Raman Study of CeO₂: Second-Order Scattering, Lattice Dynamics, and Particle-Size Effects," *Physical Review B: Condensed Matter and Materials Physics*, pp. 178-185, 1993.
- [67] L. T. Avisar D., "The Raman-scattering of A-type Ce₂O₃," *Vibrational Spectroscopy*, pp. 14-16, 2016.
- [68] D. Tuschel, "Why are the Raman spectra of crystalline and amorphous solids different?," *Raman Spectroscopy*, pp. 26-33, 2017.
- [69] R. Zamiri, H. Ahangar, A. Kaushal, A. Zakaria, G. Zamiri, D. Tobaldi and J. Ferreira, "Dielectrical Properties of CeO₂ Nanoparticles at Different Temperatures," *PLOS ONE*, 2015.
- [70] A. Filtschew, K. Hofmann and C. Hess, "Ceria and Its Defect Structure: New Insights from a Combined Spectroscopic Approach," *Journal of Physical Chemistry C*, p. 6694–6703, 2016.
- [71] P. Zaumseil, "High-resolution characterization of the forbidden Si 200 and Si 222 reflections," *Journal of Applied Crystallography*, pp. 528-532, 2015.
- [72] C. P. C. A. Choudhury B., "Annealing temperature and oxygen-vacancy-dependent variation of lattice strain, band gap and luminescence properties of CeO₂ nanoparticles," *Journal of Experimental Nanoscience*, pp. 103-114, 2015.
- [73] C. Schilling, A. Hofmann, C. Hess and M. V. Gandugliga Pirovano, "Raman Spectra of Polycrystalline CeO₂: A Density Functional Theory Study," *The Journal of Physical Chemistry C*, p. 20834–20849, 2017.

- [74] L. L. Z. X. Zheng X., "Formation and properties of hydrophobic CeO₂ nanoparticles," *Colloid Journal*, p. 558–563, 2014.
- [75] K. R. Singh, V. Nayak, T. Sarkar and R. P. Singh, "Cerium oxide nanoparticles: properties, biosynthesis and biomedical application," *Cerium oxide nanoparticles: properties, biosynthesis and biomedical application*, pp. 27194-27214, 2020.
- [76] D. H. K. S. M. S. D. A. Rios P.F., "Durable ultra-hydrophobic surfaces for self-cleaning applications," *Polymers for Advanced Technologies*, p. 1684–1691, 2008.
- [77] S. Phokhaa, S. Limwichean, M. Horprathum, V. Patthanasettakul, C. Chananonawathorn, P. Eiamchai, N. Chanlek and S. Maensiri, "Effect of annealing temperature on the structural and magnetic properties of CeO₂ thin films," *Thin Solid Films*, pp. 138001-138009, 2020.
- [78] B. Peng, X. Ma, Z. Lan, W. Xu and R. Wen, "Experimental investigation on steam condensation heat transfer enhancement with vertically patterned hydrophobic–hydrophilic hybrid surfaces," *International Journal of Heat and Mass Transfer*, pp. 27-38, 2015.
- [79] V. J. G. R. Park SD, "Direct oxidation of hydrocarbons in a solid oxide fuel cells," *Nature*, p. 265–267, 2000.
- [80] A. G. M.-W. Neumann H, "Relaxation and degradation of SrTiO₃ and BaTiO₃ ceramics," *Ferroelectrics*, pp. 179-186, 1986.
- [81] V. G. B. S. I. F. N. K. Migani A, "Dramatic reduction of the oxygen vacancy formation energy in ceria particles: a possible key to their remarkable reactivity at the nanoscale," *Journal of Material Chemistry*, p. 10535–10546, 2010.
- [82] M. M. Marina OA, "High-temperature conversion of methane on a composite gadolinia-doped ceria–gold electrode," *Applied Catalysis A*, p. 117–126, 1999.
- [83] F. C. I. M. Malavasi L., "Oxide-ion and proton conducting electrolyte materials for clean energy applications structural and mechanistics features," *Chemical Society Reviews*, pp. 4370-4387, 2010.
- [84] D. A. Long, *The Raman Effect: A Unified Treatment of the Theory of Raman Scattering by Molecules*, West Sussex: John Wiley and Sons, 2002.
- [85] A. Kossoy, Y. Feldman, E. Wachtel, K. Gartsman, I. Lubomirsky, J. Fleig and J. Maier, "On the origin of the lattice constant anomaly in nanocrystalline ceria," *Physical Chemistry Chemical Physics*, pp. 1111-1115, 2006.
- [86] A. Jooshesh, "Factors affecting the depth of field for SEM," [Online]. [Accessed 2022].
- [87] V. J. Gorte RJ, "Nanostructured anodes for solid oxide fuel cells," *Current Opinion on Colloid and Interface Science*, p. 236–244, 2009.
- [88] M. A. M. H. N. & H. D. A. H. Fronzi, "Theoretical insights into the hydrophobicity of low index CeO₂ surfaces," *Applied Surface Science*, pp. 68-74, 2019.

- [89] G. G. S. P. A. R. & F. C. Faraci, "Quantum size effects in Raman spectra of Si nanocrystals," *Journal of Applied Physics*, pp. 074311-074318, 2011.
- [90] Dalavi, Dhanaji, Bhosale, Appasaheb, Desai, Radhika and Patil, "Energy efficient electrochromic smart windows based on highly stable CeO₂-V₂O₅ optically passive counter electrode," *Materials Today: Proceedings*, pp. 146-152, 2020.
- [91] H. K. Chyuan, C. Hsiang, Y. Fang, S. Hou, S. W. Chang, C. W. Chang, S. L. Chao, C. P. Chen, Y. Y. He, S. R. Lin, K. M. Hsieh and M. H. Lin, "Fabrication of multianalyte CeO₂ nanograin electrolyte–insulator–semiconductor biosen," , *Fabrication of multianalyte CeO₂ nanograin electrolyte–insulator–semiconductor biosen*, pp. 71-77, 2015.
- [92] Y. C. A. S. I. Cho, "Fabricating a Raman spectrometer using an optical pickup unit and pulsed power," *Scientific Reports*, 2020.
- [93] C. Bousquet, M. Masson and M. Harrand, "Analysis of polarized Raman spectra of liquids at liquid–solid interfaces," *Journal of Raman Spectroscopy*, pp. 273-282, 1995.
- [94] G. R. C. M. G. C. D. R. M. E. S. J. I. G. K. T. Balakrishnan, "X-ray diffraction, Raman and photoluminescence studies of nanocrystalline cerium oxide thin films," *Ceramics International*, p. 8327–8333, 2013.
- [95] "Theory of Raman Spectroscopy," [Online]. Available: [https://chem.libretexts.org/Bookshelves/Analytical_Chemistry/Map%3A_Principles_of_Instrumental_Analysis_\(Skoog_et_al.\)/18%3A_Raman_Spectroscopy/18.01%3A_Theory_of_Raman_Spectroscopy](https://chem.libretexts.org/Bookshelves/Analytical_Chemistry/Map%3A_Principles_of_Instrumental_Analysis_(Skoog_et_al.)/18%3A_Raman_Spectroscopy/18.01%3A_Theory_of_Raman_Spectroscopy) . [Accessed 22 May 2022].
- [96] "Self-cleaning surfaces - Wikipedia," [Online]. Available: https://en.wikipedia.org/wiki/Self-cleaning_surfaces. [Accessed 22 May 2022].
- [97] "D8 ADVANCE - XRD," Bruker, [Online]. Available: <https://www.bruker.com/en/products-and-solutions/diffractometers-and-scattering-systems/x-ray-diffractometers/d8-advance-family/d8-advance.html>. [Accessed 22 May 2022].

List of Figures

figure 2-1: (a) and (b): eight-folds of cerium atoms and four-folds of oxygen atoms in ceo ₂ structure; (c) fcc structure for ceo ₂ (singh, nayak, sarkar, & singh, cerium oxide nanoparticles: properties, biosynthesis and biomedical application, 2020).....	15
figure 2-2: (a) fluorite structure of ceo ₂ . (b) hexagonal structure of ce ₂ o ₃ . Grey color represents ce atoms and red color represents o atoms (sun, xiao, hao, meng, & zhou, 2018).....	15
figure 2-3: comparison of ce ³⁺ and ce ⁴⁺ structure and oxygen vacancies produced in ce ³⁺ structure (deshpande, 2005).....	16
figure 2-4: a) fcc crystal cell of ceo ₂ structure. (b-d) the (100) or (200), (110), (111) planes of the ceo ₂ structure (wang zl, 2003).....	17
figure 2-5: a) calculated raman peak position for a layer of si as a function of its thickness. The bulk si frequency value is 521 cm ⁻¹ . B) calculated raman peak width calculated as a function of the size. The lines show how the confinement enlarges the raman peak for a single (1d) size-limited direction, for a two-dimensional (2d) size-limited square wire, for a three-dimensional (3d) cube (faraci, gibilisco, pennisi, & faraci, 2011).....	18
figure 2-6: schematic representation of water adsorption on a ceo ₂ surface.....	19
figure 2-7: understanding the wettability of rare earth oxide ceramics from crystallographic orientation – surface energy relationships (tam, feng, ikuhara, ohta, & erb, 2018).....	19
figure 2-8: wetting properties of three rare earth oxide’s surface with different orientation. A) water droplets on low index planes of ysz, ceo ₂ and er ₂ o ₃ epitaxial films. (b) the relationship between water contact angle and crystallographic orientation relationships. (c) the relationship between water contact angle with surface energy (normalized). It is shown that the surface energy is inversely proportional to the water contact angle. (tam, feng, ikuhara, ohta, & erb, 2018).....	20
figure 2-9: molecular structure and bonds in pdms (polydimethylsiloxane - american chemical society, n.d.).....	21
figure 2-10: raman spectrum of pdms (park, et al., 2014).....	22
figure 2-11: schematic diagram of magnetron sputtering.....	23
figure 2-12: rayleigh scattering versus stokes raman and anti-stokes raman scattering (cho, fabricating a raman spectrometer using an optical pickup unit and pulsed power, 2020).....	26
figure 2-13: example of molecules belongs to <i>t_d</i> , <i>o_h</i> point groups (nakamoto, 2008).....	28
figure 2-14: states of polarization in (a) elliptical polarization, (b) circular polarization, (c) linear polarization (bower, 1972).....	29
figure 2-15: illustration of the incident/scattering polarization on a polycrystalline sample.....	31
figure 2-16: euler angles position related to laboratory coordinate system (xyz) and crystal coordinate system (xyz).....	32
figure 2-17: types of interactions of incident electron beam in sem. (principles and applications of epma and sem, u.d.).....	33
figure 2-18: region of image in effective focus (hamid, 2018).....	34
figure 2-19: bragg diffraction. Two rays with known wavelength and phase reach a crystal and scattered off from different layers. Θ is the incident beam angle and d is the inner plane distance (cullity b. D., 2014).....	35
figure 3-1: ceo ₂ thin films on silicon substrate (ife).....	39
figure 3-2: renishaw invia raman microscope system.....	40
figure 3-3: schematic image of renishaw raman microscope set up.....	40
figure 3-4: calculated results for polarized raman experiment for (100) plane of cubic structure crystal.....	42
figure 3-5: calculated results for polarized raman experiment for (111) plane of cubic structure crystal.....	42
figure 3-6: calculated results for polarized raman experiment for (110) plane of cubic structure crystal.....	43
figure 3-7: raman spectroscopy set up after inserting polarizer and ½ wave plane.....	43
figure 3-8: a) schematic procedure of polarized raman experiment’s set up. B) sample mounted on angle marked blank plate inside raman chamber.....	44

figure 3-9: xrd for crystal characterization. A) d-8 bruker b) ceo ₂ thin films placed on holders located under x-ray light.....	45
figure 3-10: a) wca experiment's set up. B) sterile water drops on the ceo ₂ -pdms thin films.....	46
figure 3-11: a) two samples in sem holder fixed with conductive carbon tape. B) leica em ace600 coater c) zeiss supra 35vp field emission gun scanning electron microscope at uis, 15 kv acceleration voltage, 30- μ m aperture is used for getting images with sem.	47
figure 4-1: raman spectrum of ce ₂ o ₃ (avisar d., 2016)	49
figure 4-2: raman spectra of crystalline and fused quartz and a glass microscope slide (tuschel, why are the raman spectra of crystalline and amorphous solids different?, 2017).	49
figure 4-3: normalized raman spectra for samples with different parameters for (a): full range of energy (b): expanded view of ceo ₂ peak. Name of graphs includes parameters respectively (sample number, thickness, o ₂ /ar ratio, pressure, deposition rate)	50
figure 4-4: thickness vs. Normalized intensity for all samples. Samples with same thickness shows similar intensities irrespective of their different deposition parameters	50
figure 4-5: comparison of ceo ₂ peak intensity for samples with different thicknesses. Other parameters are same for each group. There are some shifts and intensity changes in ceria peak.	52
figure 4-6: comparison of ceo ₂ peak intensity for samples with different o ₂ /ar ratio. Other parameters are same for each group. There are some shifts and intensity changes in ceria peak.	53
figure 4-7: normalized raman spectra of ceria nanoparticles and the bulk material. A) the full range of energy studied, b) expanded view. It is showing that the peak position, linewidth, and line shape is changing with respect to particle size (spanier, 2001).	54
figure 4-8: comparison of raman spectra of samples annealed in different temperatures (a) left hand side without pdms (b) right hand side with pdms. Reference samples are plotted inside.....	55
figure 4-9: comparison for spectra obtained for different batches coated with pdms, with reference samples and the samples annealed in different temperatures (in lower range below 480 cm ⁻¹). From left to right the raman spectra of batch 102, 101 and 103 with 400, 200 and 50 nm thicknesses.....	56
figure 4-10: raman spectra for 101, 102 and 103 batches (without pdms) annealed in air (left hand side) and vacuum (right hand side). The peak shifts identified on each graph.	57
figure 4-11: fwhm of raman peak vs. Inverse crystalline size which have been calculated by xrd data (have been done in ife) for batches 101 and 102 (200 and 400 nm thickness respectively) annealed in air and vacuum. Fwhm decreases by increasing particle sizes which is the consequence of increasing annealing temperature. Depicted trendlines are least square fits.	59
figure 4-12: calculated curves (empty circles) and experimental results (filled circles) of intensity variation for the si peak (f_{2g}) (521cm ⁻¹) vs. Crystal rotation at parallel (blue) and perpendicular (red) polarizations. They all are in good agreement with the simulated pattern for orientation in (100) plane. Left hand side figures are the samples annealed in air and the right side are the samples annealed in vacuum respectively. The test samples are arranged according to the annealing temperature from top to down. The experimental results fit well with the simulations.	60
figure 4-13: calculated curves (empty circles) and experimental results (filled circles) of intensity variation for the ceo ₂ peak (f_{2g}) intensity (464cm ⁻¹) vs. Crystal rotation for parallel (blue) and perpendicular (red) polarization. Left hand side figures are the samples annealed in air and the right side are the samples annealed in vacuum respectively. The misfit of experimental results with calculations shows polycrystallinity of ceo ₂ layer.	62
figure 4-14: calculated curves (empty circles) and experimental results (filled circles) for reference sample. A) calculation results for (100) plane and raman peak of si (f_{2g}) intensity at 521cm ⁻¹ by the perpendicular and parallel polarization of light in raman set up. B) the experimental results of ceo ₂ peak (f_{2g}) (464 cm ⁻¹) of reference sample vs. Crystal rotational angle. Experimental data (filled circles) fit better with the calculations (empty circles) for silicon on (100) plane but for ceo ₂ the best fit is on (111) plane (the rest of unfitted results has not provided in the figures).....	63
figure 4-15: sem images of reference samples (no annealing) with and without pdms for the batch 101.	64
figure 4-16: particle size histogram measured by image j based on sem image of sample batch 103 prepared at 1000 °c in air.....	65

figure 4-17: sem images of air annealed samples with and without pdms at magnification of 80kx	67
figure 4-18: sem images of vacuum annealed samples with and without pdms at magnification of 80kx	68
figure 4-19: high resolution sem images of samples annealed in air and vacuum at 800 °c with pdms (101 batch, the films with 200nm thickness).....	69
figure 4-20: xrd patterns for reference samples,101, 102 and 103 (no annealing is performed).....	70
figure 4-21: xrd patterns for batches 101 samples annealed in vacuum and air. Results for the vacuum-1000°C sample is missed because of the sample delamination (received from ife).....	71
figure 4-22: xrd patterns for batches 102 annealed in air and vacuum conditions (received from ife).	71
figure 4-23: xrd patterns for batches 103 annealed in air and vacuum. (the patterns obtained at uis)	72
figure 4-24: lattice parameter and crystallite size of ceria vs. Annealing temperature for 101 batch.	74
figure 4-25: lattice parameter and crystallite size of ceria vs. Annealing temperature for 102 batch	75
figure 4-26: lattice parameter and crystallite size of ceria vs. Annealing temperature for 103 batch	75

List of Tables

Table 2-1: comparison of stability, activity, the number and formation energy of oxygen vacancies for low index planes of ceria.....	17
table 2-2: observed ft-raman and ins wavenumbers for 58100 molecular weight pdms (jays, hard, séné, parker, & jayasooriya, 2003).....	22
table 2-3: rotating to nonrotating axes as function of eulerian angles.....	31
table 2-4: the atomic factor coefficients for ce ⁴⁺ and o ¹⁻ ions (atomic form factors, u.d.)	36
table 2-5: structure facture for allowed planes in diffraction.....	37
table 3-1: description of the ceo ₂ on glass substrate samples (ife).....	38
table 3-2: description of the ceo ₂ on si substrate samples (from ife)	39
table 4-1: positions of ce and o atoms in ceria crystal (loridant, 2021).....	48
table 4-2: wca measurements for the ceo ₂ -pdms samples annealed in air	63
table 4-3: wca measurements for the ceo ₂ -pdms samples annealed in vacuum	64
table 4-4: wca measurements for the ceo ₂ -pdms reference samples without annealing.....	64
table 4-5: particle size measured using image j tool based on sem images	66
table 4-6: summarized results on the lattice parameters of ceox thin films (ife and uis)	74
table 4-7: summarized results on the crystalline size of ceox thin films (ife and uis).....	74

Appendices

Appendix A: High resolution SEM Images

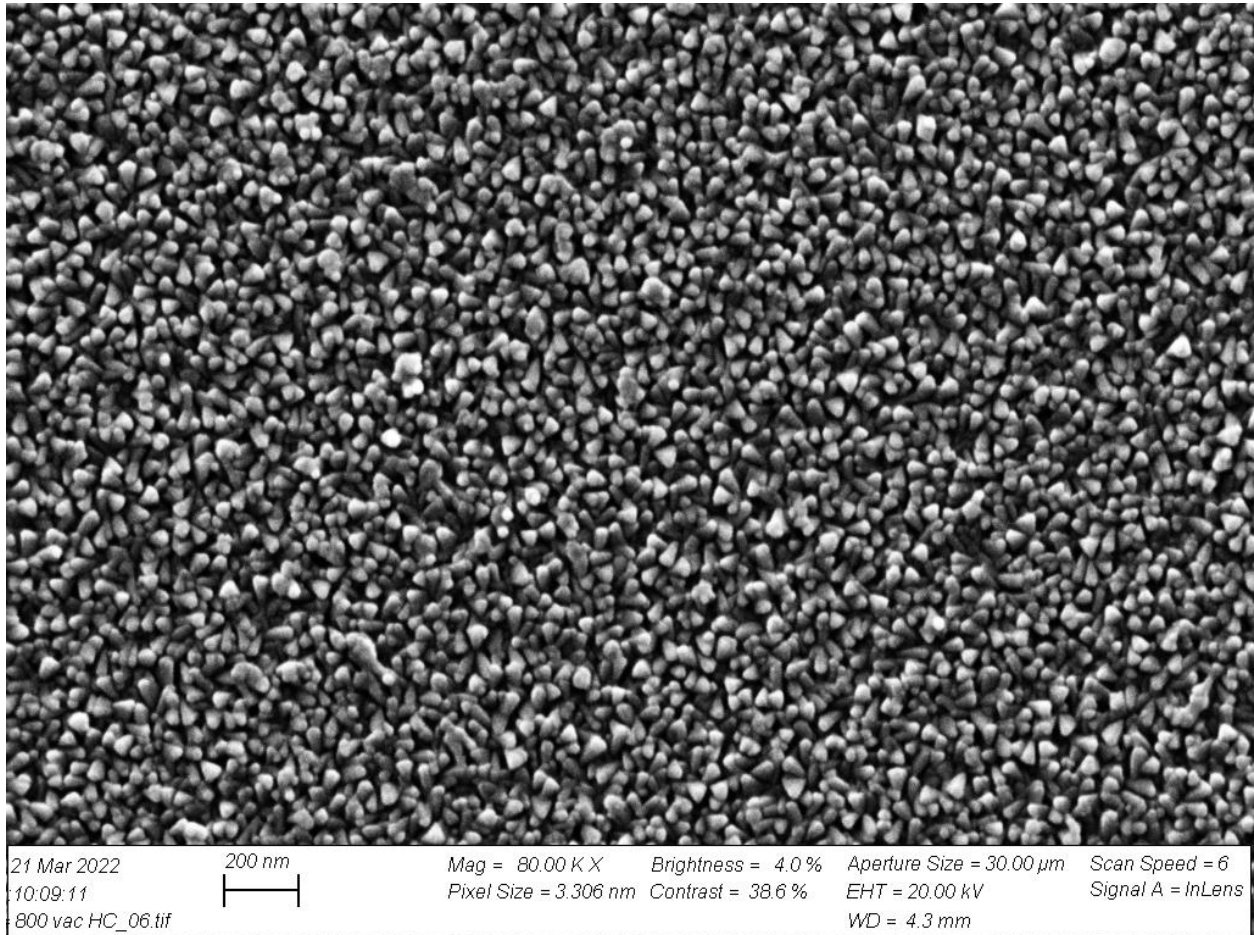


Figure A-1: High resolution SEM image of sample annealed in vacuum at 800 °C with PDMS (101 batch, the films with 200nm thickness). Figure 4-19 is same image with smaller size.

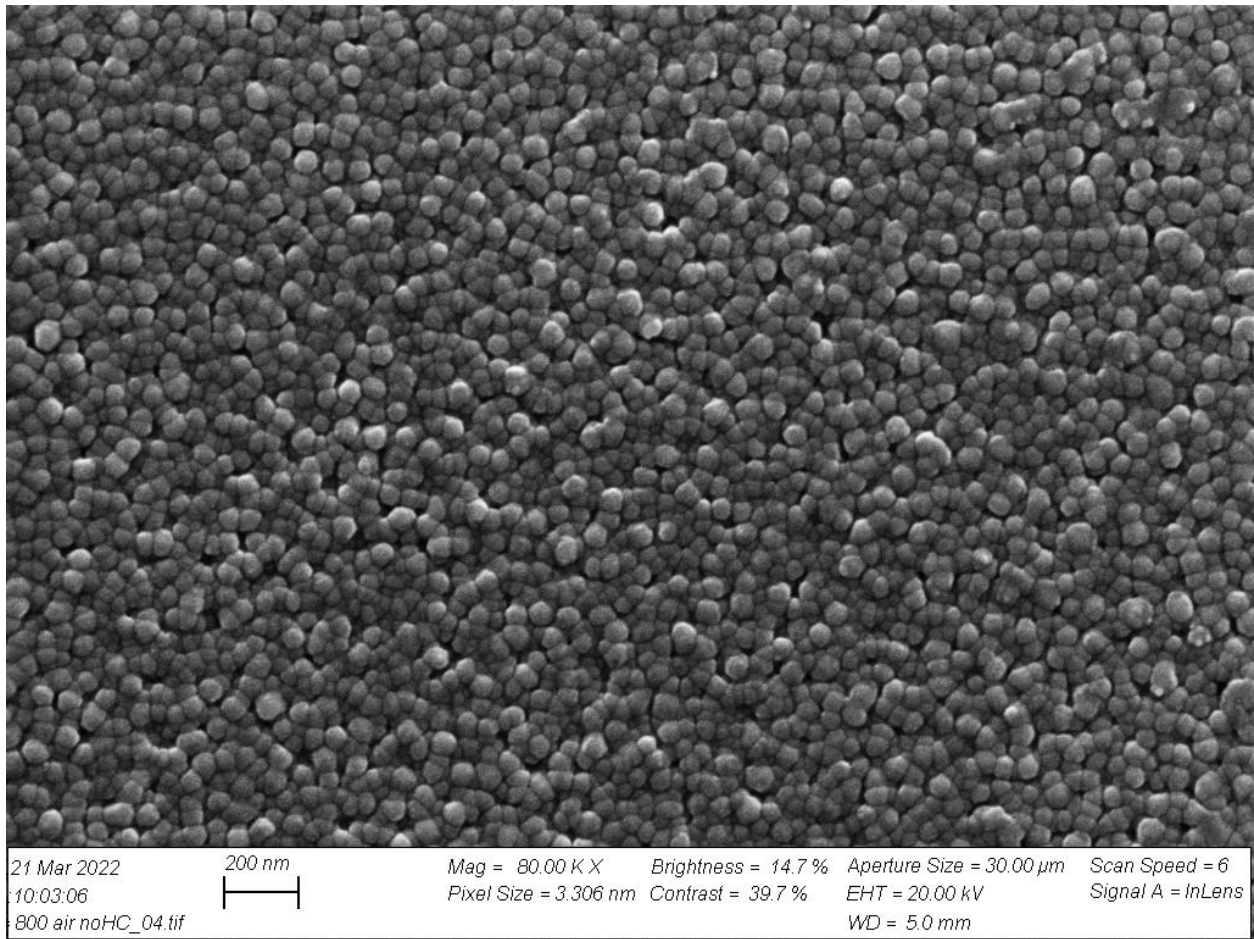


Figure A-2: High resolution SEM image of sample annealed in air at 800 °C without PDMS (101 batch, the films with 200nm thickness). Figure 4-19 is same image with smaller size.

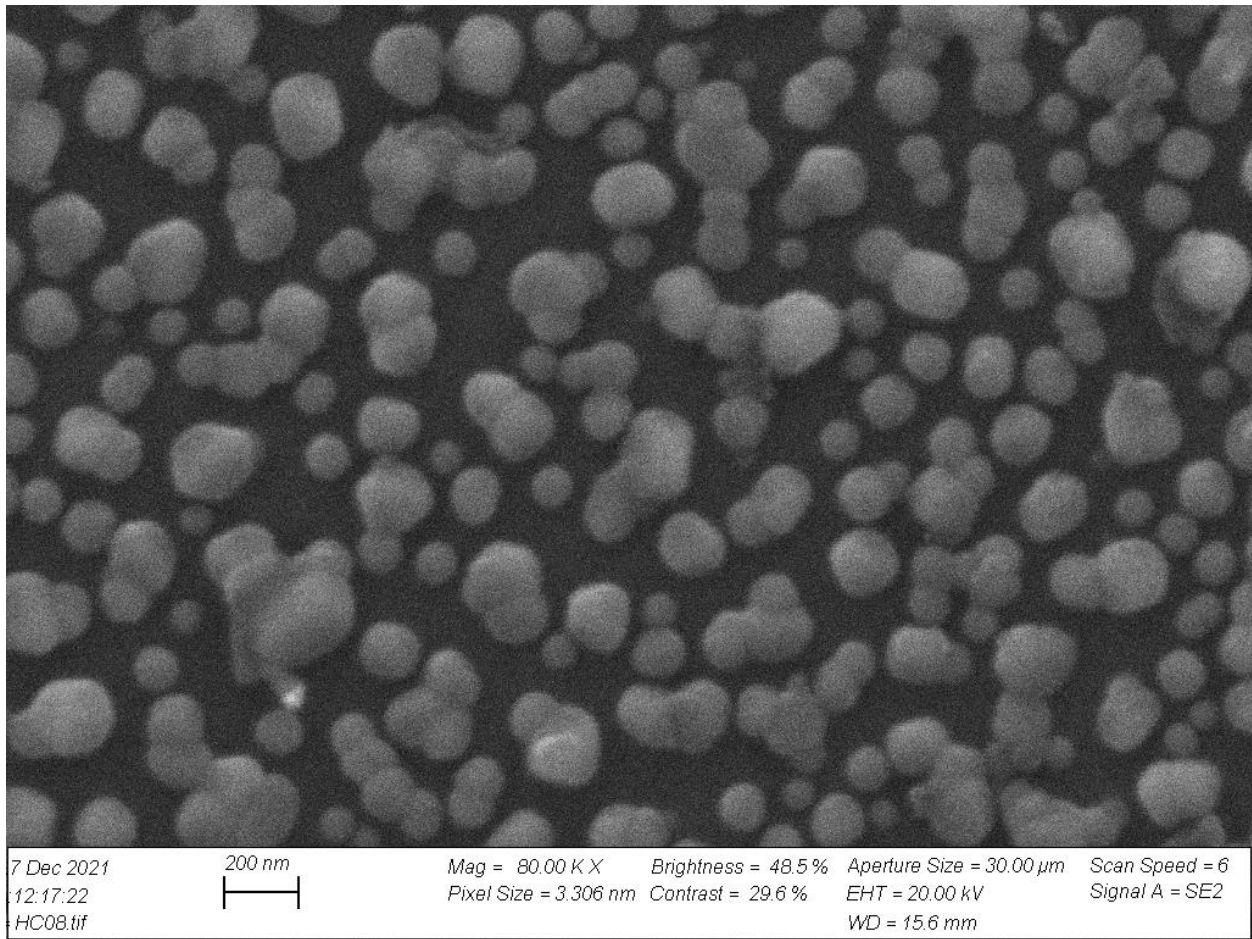


Figure A-3: High resolution SEM image of sample annealed in air at 1000 °C with PDMS (103 batch). Figure 4-17 is same image with smaller size.